Mass Loss
in Population II Red Giants:
an IRAC@Spitzer Survey of
Galactic Globular Clusters

DOTTORANDO:
Sara Fabbri

COORDINATORE:
Prof. L. Moscardini

RELATORE:
Prof. F. R. Ferraro

CO-RELATORE:
Dott. L. Origlia

Contents

Introduction

This Ph.D. Thesis has been carried out in the framework of a large project aimed at the study of Mass loss in first ascent Population II giants with varying stellar parameters and metallicity. This project started a few years ago at the Bologna University and Astronomical Observatory, in collaboration with the Virginia and California Los Angeles (UCLA) Universities.

The project

Though the current generation of theoretical evolutionary models can reasonably reproduce the general framework of stellar evolution, there are still a number of physical phenomena which are poorly understood. Among these the stellar mass loss (hereafter ML) is one of the most vexing. This is particularly the case for cool stars. Indirect evidence shows that ML strongly affects all their late stages of evolution, yet we have little theoretical or observational guidance of how to incorporate it into models. We still rely on empirical laws like that of Reimers (1975a,b) based on observations of Population I bright giants, extrapolated to lower luminosity and masses. The "Reimers Law" or some variant has been the *only* basis for stellar evolutionary models of cool stars at all ages and metallicies.

The project goals are twofold: first, to develop an empirical, scaling law for Population II giants over a range of metallicity as wide as possible; second, to develop a better physical understanding of ML.

In order to reach this goal, the following action have been undertaken.

(*i*) Mid-IR observations of a carefully selected sample of 17 Galactic globular clusters (GGCs) with different metallicity and horizontal branch (HB) morphology have been secured with IRAC on board Spitzer: a global sample counting about 8000 giant has been obtained.

(*ii*) Suitable complementary photometry in the optical and near-IR has been

also secured in order to properly characterize the stellar counterparts to the Spitzer sources and their photospheric parameters.

(*iii*) Stars with color (i.e. dust) excess have been identified, their likely circumstellar emission quantified and modelled, and empirical estimates of mass loss rates and timescales obtained.

(*iv*) The secured database of candidate mass losing giant stars and their ML properties in different GGCs are used to obtain direct information on ML in Population II giants with varying metallicity and its possible impact in shaping the horizontal branch.

Tools for data analysis and interpretation

A number of software tools have been implemented and optimized to analyze the photometric database and to interpret the results.

- To perform the photometric pre-reduction of IR images we used standard routines within the IRAF package.

- The reduction has been carried out by using ROMAFOT (Buonanno et al., 1983), a software package optimized for Point Spread Function fitting in crowded and undersampled stellar field, and DAOPHOTII/ALLSTAR (Stetson , 1994).

- In order to match and astrometrize the catalogs we used the *CataXcorr* and *CataComb* softwares, specifically developed at the Bologna Observatory (P. Montegriffo, private communication).

- The observed Color-Magnitude Diagrams (CMDs) have been complemented and analyzed by using *Smongo* routines.

- In order to obtain the ML rates we use our modified version of the DUSTY code (Ivezić, Nenkova & Elitzur, 1999; Elitzur & Ivezić, 2001), in order to compute the emerging spectrum and dust emission at the IRAC@Spitzer wavelengths between 3.6 and 8μm.

- The comparison between observations and theory has been performed using suitable evolutionary track for RGB star (Pietrinferni et al., 2006).

Thesis organization

The thesis is organized in 6 Chapters, an Introduction, a Conclusion Section and an Appendix.

Chapter 1 gives a general picture of the state of the art in the study of old GGCs and the so-called Second Parameter Problem.

Chapter 2 introduces the ML problem.

Chapter 3 describes the Spitzer mission and onboard instruments.

Chapter 4 describes the Spitzer survey of GGCs and the photometric reduction.

Chapter 5 discusses the computed color-magnitude and color-color diagnostic diagrams used to identify candidate mass loosing stars.

Chapter 6 discusses the inferred mass loss rates, timescales and total mass lost and their trends with cluster metallicity and HB morphology.

Appendix A discusses the RGB population and ML in the old open cluster NGC 6791.

Publication

Some of the results presented in this Thesis have been already published in refereed journals and conference proceedings.

They are listed below, and they are also included in the bibliographic Section and cited throughout the various Chapters.

- **The First Empirical Mass-Loss Law for Population II Giants**.
  Origlia, L., Rood, R.T., **Fabbri, S.**, Ferraro, F.R., Fusi Pecci, F., & Rich, R.M. 2007, ApJl, 667, L85

- **Probing the Galactic Bulge with Deep Adaptive Optics Imaging: The Age of NGC 6440**.
  Origlia, L., Lena, S., Diolaiti, E., Ferraro, F.R., Valenti, E., **Fabbri, S.**, & Beccari, G. 2008, ApJl, 687, L790

- **An IRAC@Spitzer Survey of Galactic Globular Clusters**.
  Fabbri, S., Origlia, L., Rood, R.T., Ferraro, F.R., Fusi Pecci, F., Rich, R.M. 2008, "Memorie della Società Astronomica Italiana", 79, 720.

- **Dust is Forming along the Red Giant Branch of 47 Tuc**.
  Origlia, L., Rood, R.T., **Fabbri, S.**, Ferraro, F.R., Fusi Pecci, F., & Rich, R.M. 2010, ApJlto be submitted

- **A Spitzer survey of Galactic globular Clusters**.
  Fabbri, S., Origlia, L., Ferraro, F.R., Rood, R.T., Fusi Pecci, F., & Rich, R.M. 2010, ApJto be submitted

Chapter 1

Stellar Populations

1.1 Stellar Clusters

Globular Clusters (GCs) are populous and dense aggregates of up to millions stars. They are among the most beautiful objects in the sky, but their importance for astronomy goes far beyond their magnificent appearance. Indeed, GCs might be considered true touchstones for astrophysics and the study of their stellar populations (SPs) addresses fundamental questions ranging from stellar structure, evolution and dynamics to Galaxy formation and the early epoch of the Universe. There are a number of macro-areas in astrophysics which are directly connected to the study of these unique class of objects, namely: (1) astro-archeology - GCs are "fossils" from the remote and violent epoch of Galaxy formation; (2) astro-dynamics - they serve as test particles for studying Galaxy dynamics and to test stellar dynamical models; (3) astro-templates - they are the largest aggregates in which all post Main Sequence (MS) stars can be individually observed, and thus serve as fiducial templates for understanding the integrated light from distant stellar systems.

Because GCs are made of such a large population of stars, all located at the same distance from us and possibly with the same age and chemical composition, they have been considered the best example of simple SPs and thus natural laboratories to test theoretical models of stellar evolution.

However, in the last years, an increasing number of spectroscopic and photometric evidences have dramatically changed such a simple view, showing that GCs harbor stars with different chemical features, show a large variety of Horizontal branches (including rather peculiar morphologies) and in some cases exhibit the even more spectacular MS and Sub Giant Branch (SGB) splitting. Such evidences suggest that multiple stellar populations with different chemical

compositions (in the He and/or metal content) and ages are present in several GCs. One of the first, robust indication of multiple stellar populations in GCs has been obtained by spectroscopic investigations. Stars in GGCs are known to be homogenous in their overall metal content. However, significant star-to-star abundance variations of some light elements (namely Li, C, N, O, Na, Mg, Al) have been recently discovered (both in evolved and unevolved stars), suggesting that GGCs harbor two sub-populations with different chemical abundance ratios. In particular, two main abundance patterns have been detected in all GCs studied so far: an anti-correlation between O and Na abundances, and an anti-correlation between Mg and Al. Such features have been recognized as the signature of material processed through hot H-burning, via the Ne-Na and Mg-Al cycles, that occur at high temperatures (T $\sim 10^8$ K) during the Asymptotic Giant Branch (AGB) phase. The stars with a chemical composition similar to the Galactic field, should be considered as the first stellar generation born in the GC, while the stars with high Na and low O abundances (as well as those with high Al and low Mg) have been interpreted as a second stellar generation born from the ashes of the first population, which polluted the cluster with the ejecta of the AGB stars. The age difference between these two stellar generations is predicted to be of about 100 Myr (D'Ercole et al., 2008), too small to be detected photometrically in the MS Turn-Off regions. The Na-enhanced and O-depleted stars should be accompanied by high He-contents (D'Antona & Caloi, 2004), with a large impact on the color distribution along the HB (since He-rich stars should be less massive) but a negligible impact on the other morphological sequences. For this reason, the He-rich, Na-rich and O-poor stars should to be located (once evolved off the RGB) along the blue side of the HB, while the stars of the first generation (with a normal He content) should be located in the red side of the HB. Within this framework the GC abundance patterns and the second parameter problem might be intimately linked. In these last years, a few GGCs have been identified undoubtedly harboring multiple stellar populations, with the detection of spectacular splitting in their morphological feature in the Color-Magnitude Diagram (CMD). While being quite different among each others, all these clusters are among the most massive GCs in our Galaxy, with masses of about 10^6 solar mass.

(1)— NGC 2808 exhibits a quite complex MS, splitted in 3 sub-structures

(Piotto et al., 2007) and an extended HB, similar to that observed in Omega Centauri. Given the same iron content (as confirmed by spectroscopic investigations), the explanation invoked for its MS structure requires the existence of 3 sub-populations with different He abundances. These sub-populations may be associated to the 3 stellar groups with different O content already detected in previous chemical analysis (it is worth noticing that NGC 2808 exhibits the most extended Na-O anti-correlation observed so far).

(2)— NGC 1851 shows a bimodal HB and 2 sub-populations along the SGB (Milone et al., 2008), likely linked to an age dispersion of at least 1 Gyr or to different metal content (for example a population with a normal chemical composition and another one with a strong CNO Na anti-correlation; in such a case the SGB splitting can be explained without invoking an age dispersion).

(3)— NGC 6388 shows a SGB splitting, similar to the one in NGC 1851, with an extended HB (despite its high metallicity). The 2 twin GCs NGC 6388 and 6441 represent an intriguing and poorly understood case, since they are 2 of the most promising targets to harbor a He-enhanced sub-population, as suggested by (Caloi & D'Antona, 2007) in order to reproduce their HB morphology. A detailed search for possible splitting in their MSs is mandatory to carefully understand these 2 objects.

While it is true that these GCs show multiple evolutionary sequences and some chemical inhomogeneity (e.g., the Na-O anti-correlation, CN inhomogeneity, etc), the iron abundance within all clusters is homogeneous. Specifically, this is the case for NGC 6388 and NGC 6441, where Carretta et al. (2007) and Gratton et al. (2007) did not detect any major iron spread, and possible age dispersion does not exceed 1 Gyr. There are only two GC-like stellar systems in the Galaxy, which show a significative spread in metallicity: Omega Centauri (Sollima et al., 2005a,b, 2007) and Terzan 5 (Ferraro et al., 2009).

(i)— Omega Centauri represents one of the most intriguing and puzzling stellar system in the Galaxy showing three sub-structures in its MS (Bedin et al., 2004), a multiple SGB with at least 4 sub-branches (Sollima et al., 2005a,b; Villanova et al., 2007) and RGBs (Pancino et al., 2000). The chemical abundance pattern is also quite complex. A recent spectroscopic follow-up has show that the blue MS exhibits twice the overall metal abundance than the dominant red MS and the only way to appropriately reproduce the MS splitting

and chemical composition is to assume different He content for the stars along the two sequences: primordial for the dominant old population and enriched (with Y of about 0.38) for the second one. These evidences might also suggest that Omega Centauri is the remnant of a dwarf galaxy and not a genuine GC, hence an accurate description of its sub-populations and chemical signatures is crucial to disentangle the origin of this system.

(ii) Terzan 5 is a globular cluster-like stellar system in the Galctic Bulge. which has been recently found to harbor two stellar populations with different iron content (Ferraro et al., 2009). This discovery was possible by combining: (i) high-resolution images in the K and J bands obtained by using the Multi-Conjugate Adaptive Optics demonstrator MAD at the Very Large Telescope of the European Southern Observatory, that led to the discovery of two well-separated red horizontal branch (HB) clumps; (ii) prompt spectroscopic observations (performed with NIRSPEC at the Keck telescope) of a few stars in the two HB clumps have confirmed that the two populations have a different metal content (namely [Fe/H]=-0.2 and [Fe/H]=+0.3). A first comparison with theoretical stellar isochrones has led to interpret these observational facts in terms of distinct populations generated by two star formation bursts with a time separation of a few (~ 6) Gyrs (12 and 6 Gyrs ago, respectively). Hence, Terzan 5 is the first GC-like system showing a spread in the iron content ever discovered in the Galactic Bulge and it could be the relic of one of the building blocks that contributed to the Bulge formation. Indeed, this discovery opens a new perspective to our understanding of the formation of the Galactic Bulge and in general, of galaxy bulges: it could be the observational confirmation that galactic spheroids originate from the merging of pre-formed internally-evolved stellar systems.

1.2   The HB morphology and the Second Parameter Problem

The correct interpretation of the evolutionary sequences in the color-magnitude diagrams (CMD) of GCs is of paramount importance in order to understand the origin and the formations history of these stellar systems. In particular, the horizontal branch (HB) is a unique astrophysical tool. Its wide color (temperature) distribution, usually called the HB morphology, is the result of large differences in the radius of stars having almost the same absolute

luminosity at the same evolutionary stage.

Particularly interesting are the hottest HB stars and their progeny, which are thought to be the sources of the mysterious UV-excess observed in elliptical galaxies and spiral bulges (Buzzoni, 1989; Greggio & Renzini, 1990). In fact the hottest HB stars (the so-called "extreme HB (EHB) stars", also observed as hot subdwarfs (sdO/sdB) in the Galactic field), have lost almost entirely their hydrogen-rich envelope during the preceding red giant branch (RGB) phase. Hence after the core helium exhaustion, these stars do not return to the asymptotic giant branch (AGB), but rather spend their He-shell burning phase as hot AGB-manqué or Post-early AGB stars, with lifetimes that are strongly influenced by the still poorly understood behavior of the convective core boundary near He exhaustion (Dorman & Rood, 1993). Although present in small numbers, these stars dominate the integrated light of stellar aggregates in the UV and they well could be the sources of the UV-excess in old stellar systems. Hence the full understanding of the processes which drive the observed HB morphologies is of paramount importance in many different astrophysical contests.

Since the star location in effective temperature along the Zero Age Horizontal Branch (ZAHB) depends on all parameters involved in the models (see e.g. Rood, 1973), HB stars behave as amplifiers, displaying the record of both the initial conditions and of any variations and perturbations (even the tiny ones) in the evolution of the star from its birth up to the HB stage. Hence, *reading properly* the HB morphologies can yield some understanding of the Population II stellar evolution in general, and the specific stellar systems (clusters or galaxies) in particular.

Historically, the exceptional sensitivity of HB star location in color to almost any model parameter was perceived during the early 1960's by Sandage & Wallerstein (1960), Faulkner (1966), VandenBergh (1967), Sandage & Wildey (1967). These authors set the basis of the so-called "Second Parameter" problem which nowadays embraces the whole subject related to studying HB morphologies. To a first approximation, the different location, extension, and morphology of the observed HB can be described in terms of the variation of the metal abundance ([Fe/H] in the usual notation), the *first* parameter. This approximation is too rough, as the actual description of the observed HB morphologies apparently requires the use of a *second* parameter ($2^{nd}P$),

whose nature is still unknown. Unfortunately, there are too many *candidate* $2^{nd}P$'s (i.e., age, helium abundance, [CNO/Fe], rotation, etc.) and a too deep ignorance about mass loss, the crucial event during the post-Main Sequence evolution leading to the HB stage (cf. Rood, 1973).

1.2.1   ZAHB models and mass loss

Very schematically, the general model of the HB which emerged in the 1970's was that HB stars are core helium burning stars which had lost $0.2\,M_\odot$ along the RGB with a star to star dispersion of $\sim 10\%$ (first quantified by Rood, 1973). By analysing the models one can conclude that the quantity which actually drives the ZAHB star location is the ratio of the core mass to the total mass, M_c/M_{ZAHB}. In turn, this ratio depends on two sets of parameters: first, the *intrinsic, original* properties of the stars, like age, chemical composition, etc., and second, the phenomena and effects which may change M_{ZAHB} or M_c during the stellar evolution. In particular, mass loss is the dominant factor which lowers the initial mass M_i down to M_{ZAHB}, with $M_i - M_{ZAHB} = \Delta M$, while M_c might vary for instance due to the effects of rotation (Mengel & Gross, 1976; Pinsonneault et al., 1991). In summary, the larger the ratio M_c/M_{ZAHB}, the bluer is the ZAHB location.

The basic characteristics of the ZAHB models worth noting here can thus be summarized as follows:

a) For any metallicity and a fixed helium abundance and core mass, ZAHB models are bluer with decreasing total mass.

b) For a fixed helium abundance and core and total masses, ZAHB models are bluer with decreasing metal content (assuming the constant solar-scaled compositions).

c) For a fixed chemical composition and assuming *no or identical mass loss during the previous RGB phase*, the stars evolving from the RGB toward the ZAHB have smaller initial masses with increasing cluster age. Consequently, ZAHB models are expected to be bluer with increasing age. In particular, this explains why the cluster age is an obvious $2^{nd}P-$candidate. In fact, clusters having the same metallicity should have very similar HB's. If, as observed, they display differences in the HB mean color distributions, it could be ascribed to age effects, being older the clusters having bluer HB's.

d) Increasing the Helium content would naturally reduce (at fixed age) the

initial mass M_i of the star and would move the ZAHB models to the blue. Consequently, ZAHB models are expected to be bluer with increasing helium content.

e) For a fixed age, chemical composition and total and core masses, the ZAHB location is uniquely identified. Hence, to reproduce the observed spread in color (temperature) of HB stars within a given cluster, one must introduce the existence of a corresponding spread among the cluster stars in at least one of the above parameters, as Rood (1973) clearly showed with his simulations.

The scenario presented above is able to offer a general understanding of the observed HB's but fails to yield a detailed description of each individual case, mostly because of even general hints on mass loss and on its dependence on star intrinsic parameters (especially the metallicity).

In this respect the Figure 1.1 (a reproduction of Figure 1 by Fusi Pecci et al., 1993) is illuminating and offer the possibility to make some essential considerations.
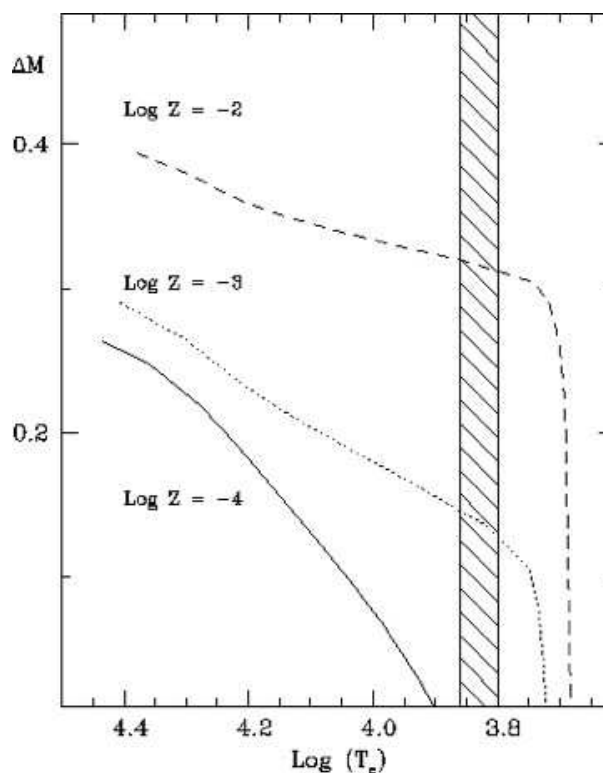

Figure 1.1: Amount of mass ΔM (in solar masses) that a star having initial mass M_i has to lose during the previous evolutionary phases to be then located on the ZAHB at a given temperature (color), with varying metallicity.

1. The plot can be read as yielding the amount of mass ΔM (in solar masses) that a star having initial mass M_i has to lose during the previous evolutionary phases to be then located on the ZAHB at a given temperature (color), with varying metallicity.

2. It is easy to see that for $\Delta M = 0.0$ the ZAHB location is bluer with decreasing metallicity and, more importantly, at different metallicities very different behavior with increasing mass loss is seen.

3. In the high metallicity regime, mass loss in unable to move the ZAHB location in temperature (color) until the total mass lost by the star reaches a threshold of about $0.3 M_\odot$. Then, any further mass loss is very effective in shifting towards higher temperatures the star position along the ZAHB.

4. At intermediate metallicities, one has the maximum sensitivity of ZAHB temperature to mass loss. The stars move from the red extreme to the far blue tail within a range of mass loss less than $0.3 M_\odot$. Hence, the clusters having metallicity in this range are the most promising candidates to detect a variation of the mass loss due to external or dynamical effects.

5. At low metallicities, the sensitivity of ZAHB location to mass loss is quite high and almost linear, but the stars lie even for $\Delta M = 0.0$ in the blue HB, and the color transitions are less evident. This does not imply however that the spread in M_{HB} is small. In fact, as can be seen from Figure 1, if one restricts the consideration to just the region bluer than the instability strip, the metal poor regime displays the maximum slope.

6. Note that the comparison between the three regimes have been carried out assuming *the same age* for the clusters. A difference in age would at least partially simulate a difference in metallicity (to a first order, older clusters have bluer HB's, just as if they were more metal poor). Therefore, though the actual metallicity still controls the HB morphology, age variations can partially move clusters from one regime to another.

From an observational point of view, the progressive addition of new data and the construction of high-quality CMD has allowed the collection of a large sample of observed HB morphologies and a deeper look into the problem. This has produced a rather complex scenario. First of all the use of UV observations has shown that UV-CMD are the best plane where the HB morphology can be investigated (see Ferraro et al., 1998, 1999b). In fact, in the classical $(V, B-V)$ color-magnitude diagram (CMD), stars at the blue-end of the HB lie along an

almost vertical sequence (the so-called "blue tail, BT"), extending down to
visual magnitudes similar to or fainter than the main sequence turnoff (MSTO)
and it is intrinsically difficult to evaluate the real extension of the HB in the
"visual" planes (see the case of NGC 6388 - Dalessandro et al., 2008). The
use of UV and optical planes has allowed to perform direct comparison among
clusters with similar metallicity and age (as the classical triplet M3/M13/M80
see Ferraro et al., 1997, 1998, see Figure 1.2). Moreover, in a growing number
of GGCs the stellar distribution in the HB has been found to be interrupted
by underpopulated regions or "gaps". These gaps are particularly evident and
are best studied when far-UV filters are used. Multi-populations separated by
gaps along the HB might be due to the existence of two mass loss "drivers"
(Ferraro et al., 1998), or to phenomena like the helium dredge-up (Sweigart et
al., 2002), or helium abundance variations (D'Antona et al., 2002, 2005).
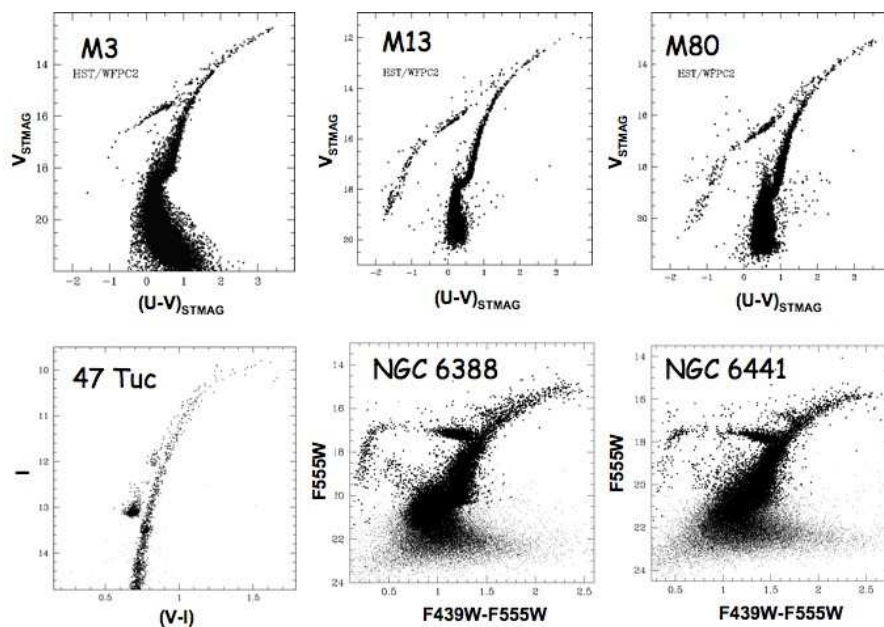
Figure 1.2: Top: the M3-M13-M80 triplet, three cluster with same metallicity but
very different HB morphology. Bottom: 47 Tuc, the prototype of metal rich GC,
and the pair NGC 6388-NGC 6441, that show the clump and an extended blue tails.

Recently Helium has been advocated in order to explain the blue extension
of the HB in NGC 6388 and NGC 6441 (two massive metal rich GCs)
(D'Antona et al., 2002, 2005; Busso et al., 2007; Caloi & D'Antona, 2007;
D'Antona & Caloi, 2008) and the multiple populations along the HB in
NGC 2808 and Omega Cen.

In summary, unfortunately, there are too many 2^{nd}P and it is also well possible that not a single second parameter, but a combination of parameters is responsible for the HB morphology (Fusi Pecci et al., 1993; Buonanno et al., 1997). Cluster age is a plausible and popular 2^{nd}P (Rood, 1973; Catelan et al., 2001). However, direct correlations of HB morphology with ages determined from the main sequence turnoff sometimes seem consistent with age as a 2^{nd}P and sometimes not. The truly problematic 2^{nd}P clusters are those whose HBs might be described as peculiar. These include: clusters with same ages and with bimodal HB distributions (e.g the M3/M80/M13 triplet, see Ferraro et al., 1998), HBs that show long blue tails and gaps in the distribution of stars (see Ferraro et al., 1990; Rich et al., 1997). Blue tails, bimodality, and gaps cannot be simply explained with the smooth variation of some simple 2^{nd}P like age. On the other hand, all these peculiarities can be (in principle) explained either in terms of differential ML mechanisms or different helium abundance. There are also some indications that the structural parameters of the parent cluster (Fusi Pecci et al., 1993; Buonanno et al., 1997) or stellar rotation (Renzini, 1977; Peterson et al., 1995) might play a role in HB morphology. Both could plausibly be linked to ML directly.

In the end, no discussion of HB morphology is independent of ML. For these reasons an empirical determination of the ML law for Population II stars in urgently needed in order to shed light on the role played by the different 2^{nd}P in determining the HB morphology.

Chapter 2

Mass Loss

2.1 Introduction

Despite its importance in our comprehension of stellar evolution, mass loss (ML) is a physical process which is still poorly understood particularly in cool stars. ML strongly affects all the late stages of stellar evolution, but empirical determinations of its occurrence are still sparse as well as its modeling. We have relied on empirical laws like that of Reimers (1975a,b) based on observations of Population I giants. Subsequent work (Mullan, 1978; Goldberg, 1979; Judge & Stencel, 1991; Catelan, 2000) led to slight refinements, but a ML law directly calibrated on Population II low-mass giants has never been determined. Radiation pressure acting on dust might plausibly drive winds in luminous red giants (Willson, 2000; van Loon, 2000). However, in old populations, stars on their first ascent of the red giant branch stars do not reach luminosities sufficient for this mechanism to be efficient. On the other hand, there is a vast amount of indirect, *but quantitative,* evidence for ML in first ascent red giants. This has especially been the case in galactic globular clusters (GGC) where the evidence includes the observed morphology of the horizontal branch (HB) in the cluster color-magnitude diagrams (CMDs), the pulsational properties of the RR Lyrae stars, the absence of asymptotic giant branch (AGB) stars significantly brighter than the red giant branch (RGB) tip, and the masses inferred for white dwarfs in GCCs (Rood, 1973; Fusi Pecci & Renzini, 1975, 1976; Renzini, 1977; Fusi Pecci et al., 1993; D'Cruz et al., 1996; Hansen, 2005; Kalirai et al., 2007).

2.2   Reimers Law

The necessary incidence of ML from stars in advanced stages of evolution was recognized many years ago. Stars with masses above the white dwarf limit of 1.4 $M_\odot$ cannot stabilize themselves after exhaustion of the various sources of nuclear fuel and will finally collapse, releasing an enormous amount of energy in a supernova explosion. Supernova rates, however, seem to be considerably lower than death rates of stars in the mass range above 1.4 $M_\odot$. This suggest that these stars have lost a large fraction of their original masses during some phase of evolution. Additional indirect evidence for ML comes from population II horizontal branch stars: Rood (1973) first reported from a theoretical study of the H-R diagram of GCs, that a total ML of 0.2 $M_\odot$, with a dispersion of a few hundredths of a solar mass, in stages preceding the horizontal branch stage was necessary in order to obtain a reasonable HB morphology.

The occurrence of ML from red giants was first demonstrated by Deutsch (1956, 1960). From the analysis of violet-shifted absorption cores present in the blue and visual spectra of sufficiently luminous and cool red giants Deutsch (1956, 1960) found these stars have cool expanding envelopes of large dimensions and lose mass to the interstellar medium. In the following years these extended envelopes have become visible through infrared observations of circumstellar dust (Gillett et al., 1968; Woolf & Ney, 1969; Origlia et al., 2002), through polarization of the starlight caused by dust particles, and through radio observations of molecular maser lines in the most luminous and red variables and supergiants (Wilson & Barrett, 1972; Wilson, 1973). ML rates as determined by Deutsch (1960) and Weymann (1962) failed to satisfy evolutionary requirements even for low mass stars. A following re-discussion of circumstellar absorption lines using new observation, however, changed mass-loss rates of M giants considerably and made it possible to study the dependence of ML on basic stellar parameters. In 1975, from the blue shift of the chromosferic CaII K emission component, Reimers obtained the empirical mass-loss relation:

$$\dot{M}_R = \eta_R \, 4 \times 10^{-13} \frac{L_*}{g_* R_*} \qquad \left[M_\odot \; yr^{-1} \right], \qquad (2.1)$$

where L_*, g_* and R_* are stellar luminosity, gravity and radius, respectively, given in solar units, and $\dot{M}_R$ is in $M_\odot \; yr^{-1}$.

η_R is a variable or fitting parameter, introduced later on to allow for more

or less efficient ML ($\eta_R = 0.3 \div 3$).

The Reimers empirical mass-loss relation should be considered as an interpolation formula only and not as being strictly valid. Moreover, the ML formula by Reimers suffers from some important deficiencies. First, it is calibrated on a small sample of giant stars, the majority being AGB stars, as shown in Figure 2.1, that are brighter than low mass RGB stars. The second deficiency consist in the necessity of adjusting the fitting parameter η_R, as different η-values are required ad hoc to match observed mass-loss rates from different types of giants and supergiants. In particular in order to account for a somewhat less efficient ML along the RGB, η_R must be 0.3.

2.2.1 ML formulae revisited

The Reimers relation is not the only ML formula available: in particular, alternative formulae have been presented by Mullan (1978), Goldberg (1979), and Judge & Stencel (1991). Catelan (2000) has revised all of these formulae, employing a most extensive data set available in literature: that of JS91 (Judge & Stencel, 1991). The ML rates provided in JS91 were compared against more recent data (Guilain & Mauron, 1996), and excellent agreement was found. However, the JS91 database still counts only 20-30 giants, the majority being AGB stars, as shown in their plot (see Figure 2.1).

The following are the ML formulae revisited by Catelan (2000):

- Reimers' original ML formula:

$$\dot{M} = 5.2 \times 10^{-16} \left(\frac{L_*}{g_* R_*} \right)^{+1.4} \qquad [M_\odot \ yr^{-1}], \qquad (2.2)$$

- Mullan's formula:

$$\dot{M} = 2.4 \times 10^{-15} \left(\frac{g_*}{R_*^{\frac{3}{2}}} \right)^{-0.9} \qquad [M_\odot \ yr^{-1}], \qquad (2.3)$$

- Goldberg's formula:

$$\dot{M} = 1.2 \times 10^{-15} R_*^{+3.2} \qquad [M_\odot \ yr^{-1}], \qquad (2.4)$$

- Judge e Stencel's formula:

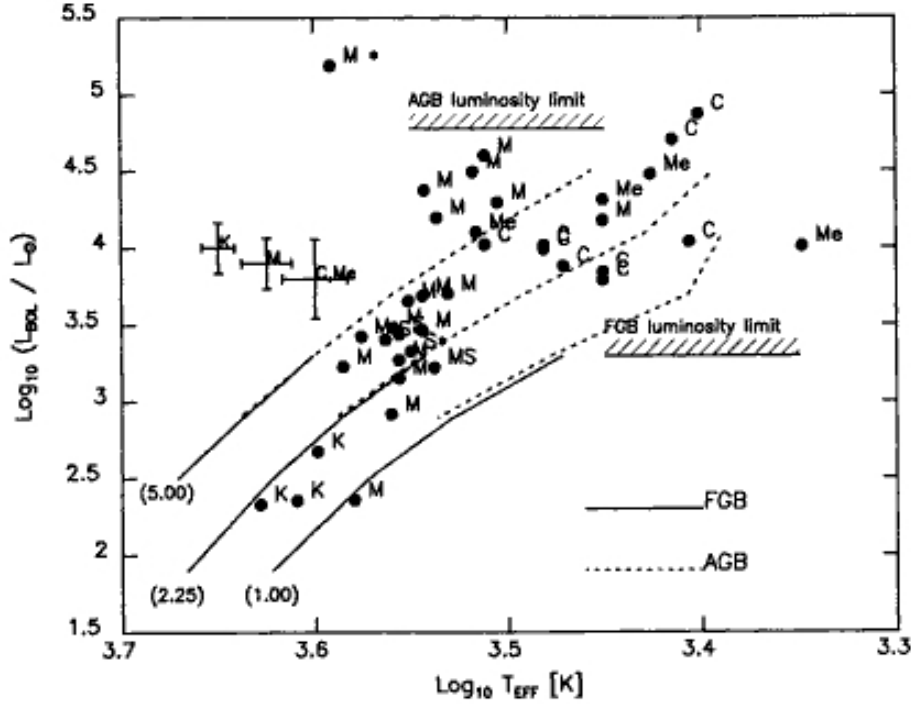$$\dot{M} = 5.0 \times 10^{-15} g_*^{-1.6} \qquad [M_\odot \ yr^{-1}]. \qquad (2.5)$$

Figure 2.1: The JS91 (Judge & Stencel, 1991) database.

Stellar luminosity L_*, gravity g_* and radius R_* are in solar units and $\dot{M}_R$ is in $M_\odot \ yr^{-1}$.

Figure 2.2 shows the ML rates obtained from the revised ML formulae. ML rates are obtained for red giant stars of fixed temperature ($T_* = 4000$ K) and mass ($M_* = 0.8$ $M_\odot$), and varying luminosity, radius and gravity.

Another expression, suggested to Catelan (2000) by VandenBerg, provides a good fit to the data:

$$\dot{M} = 3.2 \times 10^{-12} L_*^{1.1} g_*^{0.9} \qquad [M_\odot \ yr^{-1}] . \qquad (2.6)$$

As in Reimers' case, these equation were derived based on Population I stars. Hence they too are not well established for low-metallicity stars. Moreover, there are only two first-ascent giants in the adopted sample.

Finally Schröder & Cuntz (2005) proposed a modification to the Reimers' formula based on some theoretical arguments. They relation explicitly includes a dependence from all the stellar parameters:

$$\dot{M} = 8.0 \times 10^{-14} \frac{L_* R_*}{M_*} \left(\frac{T_{eff}}{4000} \right)^{3.5} \left(\frac{1 + g_\odot}{4300 g_*} \right) \qquad [M_\odot \ yr^{-1}] . \qquad (2.7)$$
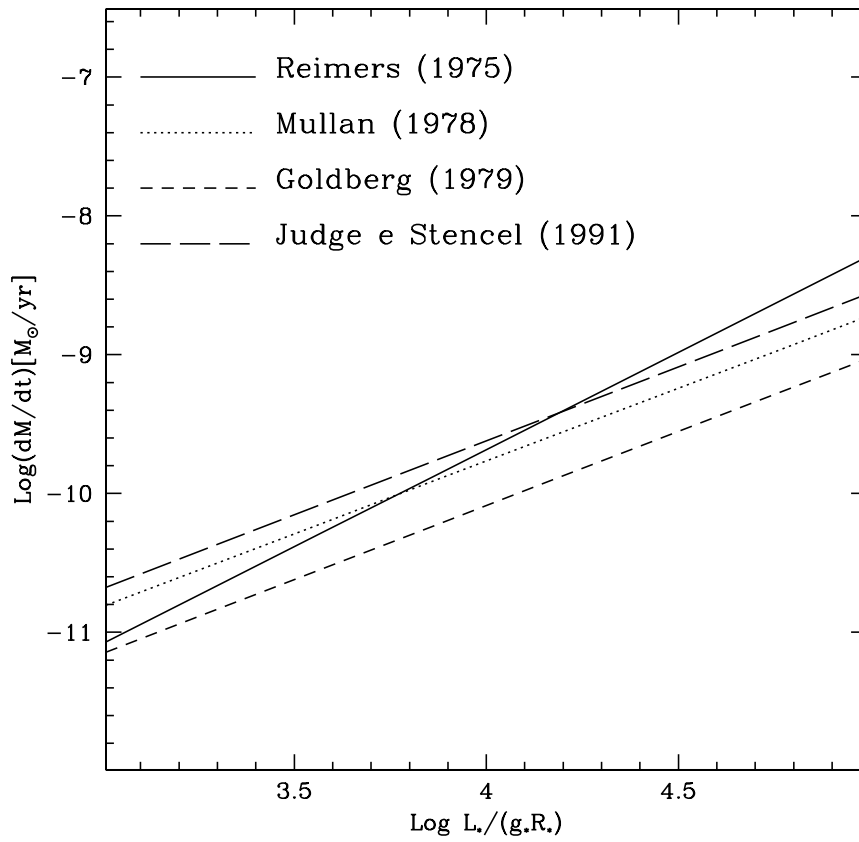
Figure 2.2: Comparison between ML rates obtained from the revisited ML formulae (Catelan, 2000). The formulae have been obtained fixing temperature (T_* = 4000 K) and mass (M_* = 0.8 $M_\odot$) of giant stars, and varying luminosity, radius and gravity.

2.3   ML in Galactic globular clusters

2.3.1   Cosmic dust

The interstellar medium[1] (ISM) is the gas and dust that pervade interstellar space: the matter that exist between the star systems within a galaxy and between the stars in a cluster. The ISM consists of a mixture of ions, atoms, molecules, larger dust grains, cosmic rays, and (galactic) magnetic fields. The matter consists of about 99% gas and 1% dust by mass. Densities range from a few thousand to a few hundred million particles per cubic meter (from about 10^{-3} to 10^3 atom per cubic centimeter). As a result of primordial nucleosynthesis, gas in the ISM is roughly 89% hydrogen, 9% helium and 2% heavier elements.

Cosmic dust is made of dust grain and aggregates of dust grains. These particles are irregularly-shaped with porosity ranging from fluffy to compact. The composition, size, and other properties depends on where the dust is found, and conversely, a compositional analysis of a dust particle can reveal much about the dust particle's origin. General diffuse interstellar medium dust, dust grains in dense clouds, planetary rings dust, and circumstellar dust have different characteristics.
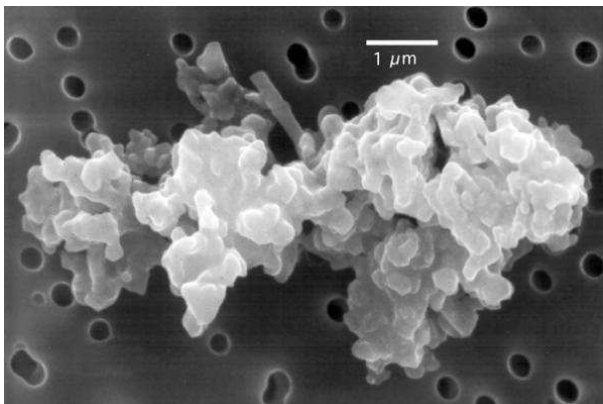
Figure 2.3: A cosmic dust particle.

Cosmic dust was once solely an annoyance to astronomers, as it obscures

---

[1]The ISM is responsible for extinction and reddening: the decreasing light intensity and shift in the dominant observable wavelenghts of light from a star. These effects are caused by absorption and scattering of light emitted by astronomical object by dust and gas between the emitting object and the observer. For Earth-bound observers, extinction arises both from the ISM and the Earth's atmosphere (atmospheric extinction). In both cases, blue light is much more strongly attenuated than red light.

objects they wish to observe. When infrared astronomy began, those previously annoying dust particles were observed to be significant and vital components of astrophysical processes. For example, cosmic dust can drive the ML, play a part in the early stages of star formation, and form planets. Observations and measurements of cosmic dust in different regions provide an important insight into the universe's recycling processes: in the clouds of the diffuse interstellar medium, in molecular clouds, in the circumstellar dust of young stellar objects, and in planetary systems such as our solar system, where astronomers consider dust as in its most recycled state.

Circumstellar envelopes of evolved stars are among the most remarkable chemical laboratories in the universe. These envelopes are created mainly by extensive ML in the later stages of stellar evolution, caused by thermal pulses in the star interior and radiation pressure on dust. Because of the low temperature of the central star, and the long time scales for ML, molecules and dust form in the envelope, and are the gently blown into the ISM. The material lost from such envelopes is thought to account for nearly 80% (by mass) of the ISM.

In circumstellar dust, astronomers have found molecular signatures of CO, silicon carbide, amorphous silicate, polycyclic aromatic hydrocarbons (PAHs), water ice, and polyformaldehyde, among others, while in the diffuse interstellar medium, there is evidence for silicate and carbon grain.

Circumstellar Dust

Circumstellar shells are quite large in size, extending up to 10^4 to 10^5 stellar radii. Near the stellar photosphere, the envelope material (all gaseous) is warm (T $\sim$ 500 K) and dense (n $\sim 10^{10}$ cm^{-3}). As the matter flows away from the star, it expands and cools. Dust begins to form at $\sim$ 5-15 stellar radii, and shortly thereafter the maximum outflow velocity is achieved. Beyond the dust formation zone, the temperature and density continue to decrease such that at the outer edges of the shell, T $\sim$ 25 K and n $\sim 10^5$ cm^{-3}. The chemistry varies substantially throughout the envelope.

The dust composition in circumstellar shells is thought to reflect that of the gas phase. In the majority of O-rich envelopes, amorphous silicates have been identified on the basis of 9.7 and 18 μm solid-state features. Evidence for crystalline silicates such as olivine and pyroxene has also been found. Other

constituents may be refractory oxides of aluminum, silicon, magnesium, and iron. In C-rich stars, the dust is thought to be primarily SiC, which has a 11.3 μm feature arising from the Si-C stretch. It has been observed in >500 AGB stars, but becomes weaker in more evolved objects. In protoplanetary nebulae (PPN) and planetary nebulae (PN), strong infrared features at 3.3, 6,2, 7.7, 8.6, and 11.3 μm are present, which can be attributed to aromatic C-H and C-C stretches and bends, the so-called aromatic infrared bands. There are also bands at 3.4 and 6.9 μm attributed to aliphatic C-H modes. All of these features likely arise from some large solid-state carbon-bearing compound consisting of hundreds of atoms.

2.3.2   Observation of diffuse clouds

Interstellar matter should be present in the central region of GCs as a result of mass-loss processes which take place during the late stages of stellar evolution. Theoretical models predict a ML of ~ 0.2 M$_\odot$ prior to the HB phase and ~ 0.1 M$_\odot$ along the AGB (Fusi Pecci & Renzini, 1976; Renzini, 1977; Fusi Pecci et al., 1993). A typical GC population has about 100-1000 giant stars brighter than the HB, and these stars have a lifetime of about $10^7 - 10^8$ yr. As a consequence of such mass-loss processes, dust e gas should be present in the intracluster medium as diffuse clouds (Angeletti et al., 1982) and/or concentrated in circumstellar envelope (Origlia et al., 2002). However one has to consider that gas is swept out each time the GC passes through the disc. Assuming that this event occurs every 0.1 Gyr, a few tens to hundreds of solar masses of intracluster matter should be located in the central regions of the most massive clusters. With the goal of detecting this diffuse component and measuring the intracluster gas emission, several survey in various spectral ranges have been performed.

Molecular gas. Molecular gas is mostly in the form of H$_2$. Using CO as a tracer, an upper limits of $M_{gas} \sim 0.1$ M$_\odot$ has been yielded in M15 (Smith, Woodsworth & Hesser, 1995), with a possible detection at a similar level in 47 Tuc (Origlia et al., 1997a).

Atomic gas. Faulkner et al. (1991) detected neutral hydrogen (H I) at 21 cm in NGC 2808 and inferred the presence of $M_{gas} \sim 200$ M$_\odot$, but other attempts to detect H I have so far resulted in upper limits of only a few M$_\odot$ (Knapp et al., 1973; Smith et al., 1990; van Loon et al., 2006).

Ionized gas. Hot stars such as blue horizontal branch stars or post-AGB stars produce a radiation field with $T_{rad} > 10000K$, which might ionize the intracluster medium (ICM). Searches for free-free continuum or Hα line emission have set limits of $M_{gas} \sim 1\,\mathrm{M}_\odot$ (Smith et al., 1976; Faulkner & Freeman, 1977; Grindlay & Liller, 1977; Freire et al., 2001).

So, searches for this intracluster gas (H I, H II, CO) yielded upper limits or marginal detection of a few tenths of a solar mass. Various mechanisms were suggested for removing gas from the clusters (Roberts, 1988), perhaps the most plausible being ram-pressure stripping by hot halo gas. There is some evidence supporting this hypothesis in the form of soft diffuse X-rays from a few of the most massive clusters (Hartwick, Cowley & Grindlay, 1982).

At the same time, with the goal of detecting dust emission in the cluster interstellar medium, some surveys of the central regions of GCs have been performed. Although circumstellar dust comprises at most one per cent of the gas mass, it is easily detected observing at infrared and millimeter wavelength, and by polarimetric measures at optical wavelength.

Mid–IR excesses and scattered polarized light have been observed in the central region of massive GCs (Frogel & Elias, 1988; Gillett et al., 1988; Forte & Mendez, 1989; Minniti et al., 1992; Origlia et al., 1995, 1997b). They are mainly associated with long period variables evolving along the AGB. Far e mid-infrared observations, using IRAS and ISO, placed upper limits of $M_{dust} \sim 10^{-3}\,\mathrm{M}_\odot$ (Lynch & Rosanno, 1990; Knapp et al., 1995; Origlia et al., 1996; Hopwood et al., 1999). Observation at mm wavelengths yields similar limits (Penny, Evans & Odenkirchen, 1997).

2.3.3   Observation of circumstellar envelopes

Circumstellar envelopes of gas and dust are unambiguous signatures of the occurrence of ML processes. The mid-IR spectral range is particularly efficient to detect warm dust around giant stars, hence to constrain mass loss rate and time-scales. Mid-IR observations have the advantage of sampling an out-flowing gas fairly far from the star (typically, tens/hundreds stellar radii). Such gas typically left the star a few decades previously, hence the inferred ML rate is also smoothed over such a time-scale. Conceptually, one could sample different distances and smoothing times by observing at different wavelengths. For astrophysical purposes it is the long-term average ML which is important.

However, in the far-IR detectors lack the requisite sensitivity and spatial resolution to measure the more diffuse cold dust in the outer regions of the expanding CS envelopes.

Moreover, GCs are very distant objects, so only the brightest giant stars are observed using ground-based IR observations. In fact, using the Wien's law[2] the peak wavelength of a blackbody of temperature 300 K is found to be nearly at 10 μm: thus, the telescope and its detectors can produce radiation in just the wavelength region the observer might be interested in. This noise is more higher than the source signal, so it's hard to detect distant and faint object even using telescope with diameter of about 8-10 meter. In short, circumstellar dusty envelopes around giant stars in GGCs are detectable only using space telescopes.

The IRAS survey (Origlia et al., 1996)

Many GGCs show positional coincidences with IRAS sources. So, using the IRAS photometric data at 12 and 25 μm, it was possible to analyze IR emission of giant stars in the central region of 18 GCs.

Table 2.1 lists the flux densities of the IRAS point source at 12, 25, 60 and 100 μm associated to GCs. Most of the fluxes at 25, 60 and 100 μm are upper limits or of low quality, while those at 12 μm are of good quality. Note that cirrus contamination at 60 and 100 μm is present in many clusters. To take into account the uncertainty in the IRAS coordinates (on average a few tens of arcsec) and the IRAS beam (30-60 arcsec), the selection criteria have been based on positional coincidences within ± 60 arcsec from the cluster centre.

To extend the available sample, it has been also investigated the possible coincidences between IRAS sources and the central regions of the Magellanic Cloud clusters: adopting a limiting radius of 200 arcsec from the cluster center, 14 clusters have been found in the LMC, and 4 in the SMC (see Table 2.2).

The main conclusion about dust properties and ML, obtained from a detailed analysis of the mid-IR emission in the selected clusters, are the following.

- Colour temperatures $T_{[12]-[25]}$ in the range 170–490 K with a mean value of ~ 270 K.

---

[2] $\lambda_{max} T = 0.290 \, cm \, K$

Cluster	F$_{[12]}$ (Jy)	F$_{[25]}$ (Jy)	F$_{[60]}$ (Jy)	F$_{[100]}$ (Jy)
47 Tuc (NGC 104)	1.710	0.509	0.400	1.000
NGC 362	0.401	0.277	0.400	1.000
NGC2808	0.751	0.250	0.400	1.080
UKS2	0.570	0.250	0.444	6.220
ω Cen (NGC 5139)	0.385	0.250	0.400	1.070
NGC 5927	0.660	0.602	0.400	1.070
Terzan 3	0.541	0.394	0.574	27.6
M62 (NGC 6266)	0.848	0.502	0.453	5.240
NGC 6358	0.236	0.330	0.432	4.540
NGC 6388	1.180	0.295	0.612	28.800
NGC 6440	1.170	0.691	0.126	11.400
NGC 6441	1.000	0.455	0.661	27.200
Terzan 11	1.520	1.100	16.3	165.
NGC 6656	0.678	8.600	21.20	14.60
M54 (NGC 6715)	0.525	0.341	0.400	1.320
NGC 6749	1.270	0.854	4.570	102.
M15 (NGC 7078)	0.414	0.854	0.748	1.200

Table 2.1: IRAS PS emission associated with GGCs. Fluxes are in units of Jansky.

Cluster	$F_{[12]}$ (Jy)	$F_{[25]}$ (Jy)	$F_{[60]}$ (Jy)	$F_{[100]}$ (Jy)
NGC 256	0.250	0.328	6.480	10.18
NGC 269	0.250	0.25	0.716	4.140
NGC 346	0.760	5.710	67.20	127.0
NGC 361	0.402	0.25	0.697	14.30
NGC 1466	0.213	0.294	1.120	2.320
NGC 1767	0.268	0.492	6.870	19.00
NGC 1850	0.250	0.116	3.990	53.32
	0.285	0.336	7.740	54.80
NGC 1854–NGC 1855	7.820	54.80	312.0	419.0
NGC 1872	3.710	40.50	267.0	416.0
NGC 1916	0.268	0.258	7.88	56.10
	0.261	0.414	7.880	63.40
	0.551	0.713	24.20	63.40
NGC 1943	0.262	0.250	1.370	87.30
NGC 1953	0.375	0.378	9.950	181.0
NGC 1978	0.289	0.554	1.770	13.10
	0.258	0.426	1.910	32.50
NGC 1984	4.160	24.20	11.70	65.20
NGC 1984–NGC 19994	1.250	1.470	8.640	83.30
NGC 1994	0.275	0.712	1.790	19.40
NGC 2002	0.296	0.250	1.320	8.260
	0.246	0.250	5.020	29.60
NGC 2004	0.250	0.250	1.480	42.20
	0.264	0.656	5.890	14.00
NGC 2041	0.325	0.294	2.800	23.50
NGC 2058–NGC 2045	0.271	0.250	1.900	10.10
NGC 2070	35.30	300.0	397.0	2490
NGC 2100	0.256	0.250	8.240	95.30

Table 2.2: IRAS PS emission associated with MC clusters.

- Equilibrium radii in the range 8×10^{-5} and 1×10^{-3} pc, with an average value of $\sim 200\,R_*$, where $R_* \sim 100\,\mathrm{R_\odot}$.

- Warm dust mass in the range 10^{-8} to $10^{-6}\,\mathrm{M_\odot}$ in GGCs, while the young LMC clusters, which have more massive and luminous giants, show larger values up to $10^{-5}\,\mathrm{M_\odot}$.

- Assuming a gas-to-dust ratio of 100–1000, upper limits for the total mass-loss rates between 10^{-7} and $10^{-4}\,\mathrm{M_\odot}\,\mathrm{yr}^{-1}$ have been obtained.

The ISOCAM survey (Origlia et al., 2002)

About ten years later, a deep, spatially resolved photometric survey became possible with the spectrophotometric capabilities of ISOCAM on board the Infrared Space Observatory (ISO, Kessler et al. (1996)). ISOCAM (Cesarsky et al., 1996) provided relatively fine spatial resolution, large field coverage, and high sensitivity in the 10 and 20 μm spectral regions.

Five massive Galactic GCs, namely NGC 104 (=47 Tuc), NGC 362, NGC 5139 (=ω Cen), NGC 6388, NGC 7078 (=M15) and NGC 6715 (=M54) in the Sagittarius Dwarf Spheroidal were observed with ISOCAM between February and August 1997, (proposals ISO_GGCS and DUST_GGC, P.I.: F. Fusi Pecci). Each of the clusters has an IRAS point source in its core (Origlia et al., 1996). The 12 μm IRAS flux is 1.7 Jy in 47 Tuc and 1.2 Jy in NGC 6388 and ranges between 0.4–0.5 Jy in the others. 47 Tuc, NGC 6388, and NGC 5139 show extended IRAS emission at 12 μm as well, with typical sizes of $2' - 4'$ and total flux densities between 3 and 11 Jy.

Beam-switching observations were performed using CAM03 and a $6''$ pixel^{-1} scale in two filters, LW7[9.6][3] (8.3–10.9 μm, centred on a silicate dust feature) and LW10[12] (8.6–15.4 μm, the IRAS 12 μm band). The total integration time for each cluster was about 2500 s and the field of view was about 3'×3'. 47 Tuc was also observed a second time in four filters, LW6[7.7] (6.9–8.5 μm), LW7[9.6], LW8[11.3] (10.7-11.9 μm) and LW10[12], for a total integration time of about 6700 s and a field coverage of about $5' \times 3'$.

Near-IR photometry of the clusters observed with ISOCAM was obtained at ESO, La Silla (Chile), using the ESO-MPI 2.2m telescope and the near IR camera IRAC-2 (Moorwood et al., 1992) equipped with a NICMOS-3 256×256

---

[3]For clarity we give the central wavelength (in μm) of the ISOCAM filters in brackets.
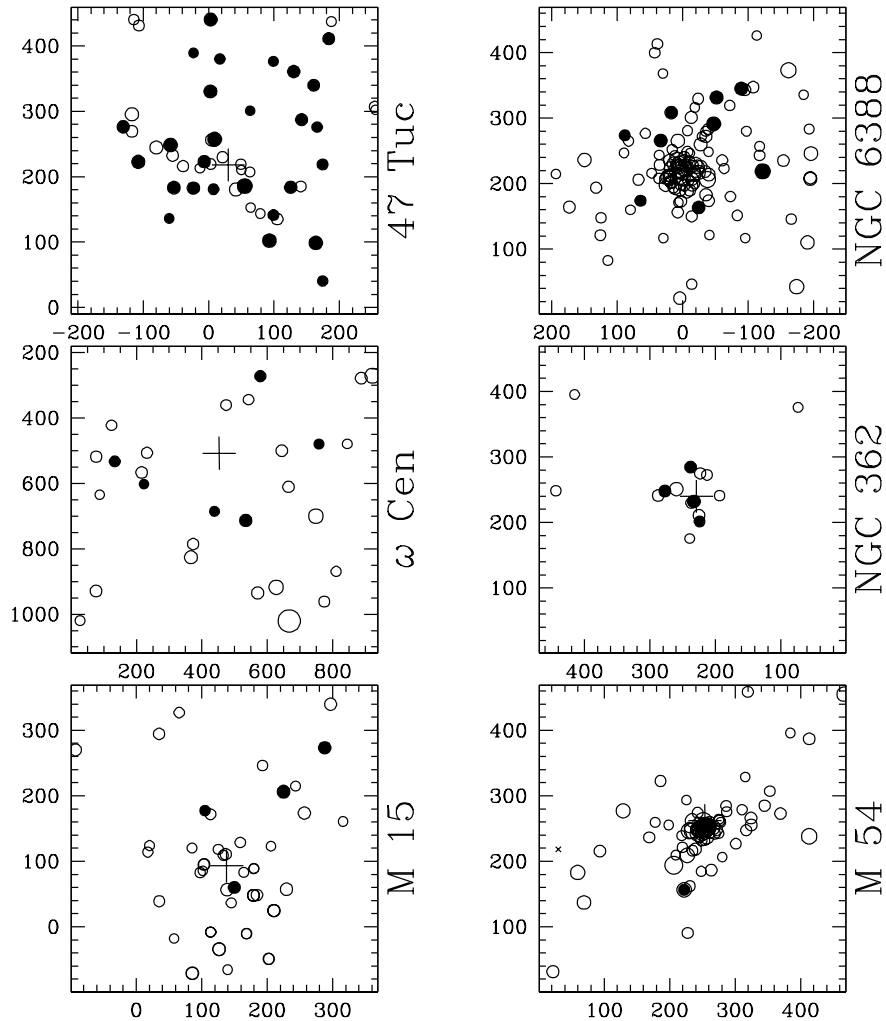
Figure 2.4: K band stellar maps of the six clusters down to a bolometric magnitude $M_{bol} \leq -2.5$. The ISOCAM 12 μm point source counterparts are over-plotted (solid circles). North is up, east is left. The X and Y coordinates are in pixel units (the scale is $0.5''$ pixel^{-1} for all clusters but ω Cen which has $0.3''$ pixel^{-1}). Each map field of view centred around the cluster centre is about $4' \times 4'$. The cross indicates the nominal cluster centre .

array detector, during different runs between 1992 and 1994. ω Cen was also observed (May 1999) with the ESO-NTT telescope using SOFI, the near-IR imager/spectrometer equipped with a 1024×1024 array detector. The near-IR stellar counterpart of each ISOCAM point source was identified by roto-translating the ISOCAM coordinate system into the near-IR system and cross-correlating the two catalogs with an overall accuracy ≤ 2 arcsec. Figure 2.4 shows the K band images of the six clusters, down to a bolometric magnitude $M_{bol} \leq$ -2.5, with the ISOCAM 12 μm contour plots superimposed.

Cluster	Stella	X	Y	K_0	$(J-K)_0$	$(K-12)_0$	M_{bol}	T_{dust} [K]	$\dot{M}$ $[M_\odot yr^{-1}]$
47 Tuc	1	55	186	6.74	0.96	1.20	-3.92	402	2.5×10^{-7}
	2	8	181	7.78	0.99	0.70	-2.84	343	8.5×10^{-8}
	3	-7	223	7.34	1.00	0.76	-3.26	491	1.0×10^{-7}
	4	99	141	7.74	1.00	1.39	-2.86	291	2.1×10^{-7}
	5	-131	276	7.15	1.12	2.14	-3.28	234	1.1×10^{-6}
	V8	3	330	6.83	1.23	1.64	-3.46	312	4.8×10^{-7}
	V26	9	257	6.55	1.24	1.16	-3.73	343	3.4×10^{-7}
NGC 362	1	277	248	8.94	0.96	1.75	-3.12	335	4.4×10^{-7}
	2	232	232	8.73	0.99	1.11	-3.29	339	2.8×10^{-7}
	3	224	156	8.80	1.25	0.99	-2.87	271	3.6×10^{-7}
ω Cen	V42	438	686	8.51	0.89	2.35	-2.58	347	7.1×10^{-7}
NGC 6388	1	17	308	9.62	0.85	0.98	-3.30	291	1.4×10^{-7}
	2	-89	345	9.34	0.98	0.76	-3.39	297	1.4×10^{-7}
	3	-47	291	8.86	1.08	0.75	-3.73	281	2.2×10^{-7}
	4	89	274	9.74	1.08	1.04	-2.85	335	1.2×10^{-7}
	5	34	266	9.11	1.16	1.36	-3.37	209	6.8×10^{-7}
	6	-24	164	9.06	1.25	0.90	-3.31	276	2.3×10^{-7}
M15	1	105	177	10.47	0.63	1.97	-2.67	397	3.3×10^{-7}
	2	150	60	9.89	0.66	1.14	-3.18	572	4.3×10^{-7}
M54	1	222	156	11.17	0.71	2.30	-3.81	272	1.1×10^{-6}

Table 2.3: Infrared photometry and ML rates for the ISOCAM point sources with dust excess.

Suitable color–magnitude and color–color diagrams of the ISOCAM point sources were constructed in order to quantify the relative photospheric and dust excess contribution. Figure 2.5 shows the $M_{\rm bol}$, $(J-K)_0$ and $M_{\rm bol}$, $(K-[12])_0$ color–magnitude diagrams. Figure 2.6 shows the corresponding $(K-[12])_0$, $(K-[9.6])_0$ color–color diagram. The $(J-K)_0$ color mainly traces the photospheric temperature. Possible circumstellar dust excess is best shown

using a combination of near and mid-IR colors. Of the 52 ISOCAM sources detected in the upper 1.5 bolometric magnitudes of the RGB, 20 show direct evidence of mid-IR circumstellar dust excess. The photometry of these sources with dust excess is reported in Table 2.3.

In NGC 6388 and in M15, the most distant clusters in the Galactic sample, also very centrally concentrated, both the total number of ISOCAM sources and the number of those with mid-IR excess must be regarded as lower limits, since stellar counterparts to the 12 μm emission cannot be identified in the very central core where the crowding is too severe given the ISOCAM spatial resolution.

No significant mid-IR excess has been found around any giant star in the observed central region of ω Cen. However, this cluster is known to be anomalous in many respects, with a multi-population RGB (Pancino et al., 2000). More crucially in the current context, while the cluster is large in absolute size, it is very low density, and this sample size is small. It has been possible to estimate that only $< 30\%$ of the brightest giants are located in the central region covered by this mid-IR survey, while in the other clusters a larger fraction of the brightest giants has been sampled. So, a much larger mid-IR spatial mapping is definitely needed.

In order to estimate the dust parameters a simple model using an optically and geometrically thin shell at constant temperature and with a νB_ν grain emissivity (Natta & Panagia, 1976; Origlia et al., 1996, 1997b) has been computed. Standard grain radius and density of 0.1 μm and 3 g cm^{-3}, respectively, are adopted. The dust temperature has been inferred from the $([9.6] - [12])$ color in all clusters, for homogeneity. The inferred values of T_{dust} are between ≈ 200 and ≈ 600 K and the dust equilibrium radii R_{dust} between 300 and 40 stellar radii, respectively. The corresponding dust masses range between a few 10^{-9} and a few 10^{-7} M$_\odot$.

The amount of material available to make dust in RGB stars must be proportional to the cluster metallicity. In fact, a large amount of dust has been only detected in the most metal rich clusters of the sample (47 Tuc and NGC 6388) while the two metal poor stars of M15 have low dust content.

Empirical ML rates can be derived from dust masses by assuming a gas-to-dust ratio and a typical timescale for the outflow. Since more dust should be present in more metal rich objects one also expects that the gas-to-dust
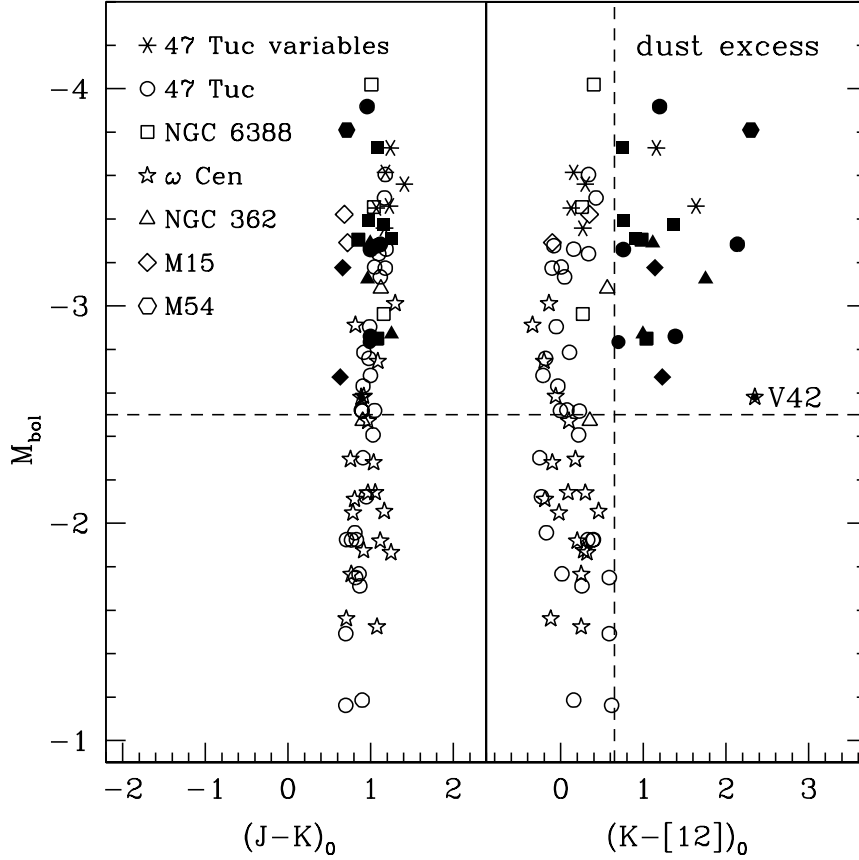
Figure 2.5: $M_{\rm bol}$, $(J - K)_0$ (left panel) and $M_{\rm bol}$, $(K - [12])_0$ (right panel) de-reddened color–magnitude diagrams down to a bolometric magnitude $M_{\rm bol} \leq -1.0$ of the ISOCAM point sources detected in the observed GCs. Sources with $(K - [12])_0 \geq 0.65$ are classified as sources with significant dust excess and are marked with filled symbols. The horizontal, dashed line at $M_{\rm bol} = -2.5$ marks the photometric threshold in the most distant clusters. The vertical, dashed line in the right panel marks the border between where 12 μm emission is dominated by the stellar photosphere or by circumstellar dust. The position of the V42 long period variable of ω Cen is also marked.
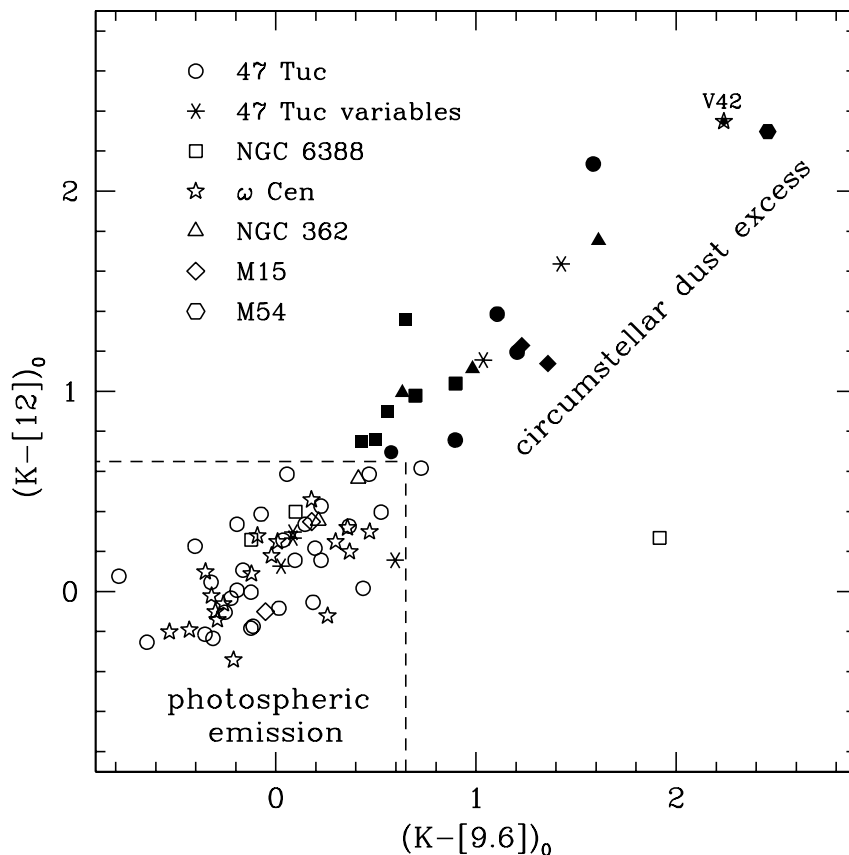
Figure 2.6: De-reddened $(K-[12])_0$, $(K-[9.6])_0$ color–color diagram of the ISOCAM point sources detected in the observed GCs. Symbols as in Figure 2.5. The dashed box indicates the region where the 12 μm emission is still dominated by the stellar photosphere. Although there is a good overall correlation between the $(K-[12])_0$ and $(K-[9.6])_0$ colors, as a conservative approach only those sources with $(K-[12])_0 > 0.65$ are classified as having dusty envelopes. The position of the V42 long period variable in ω Cen is also marked.
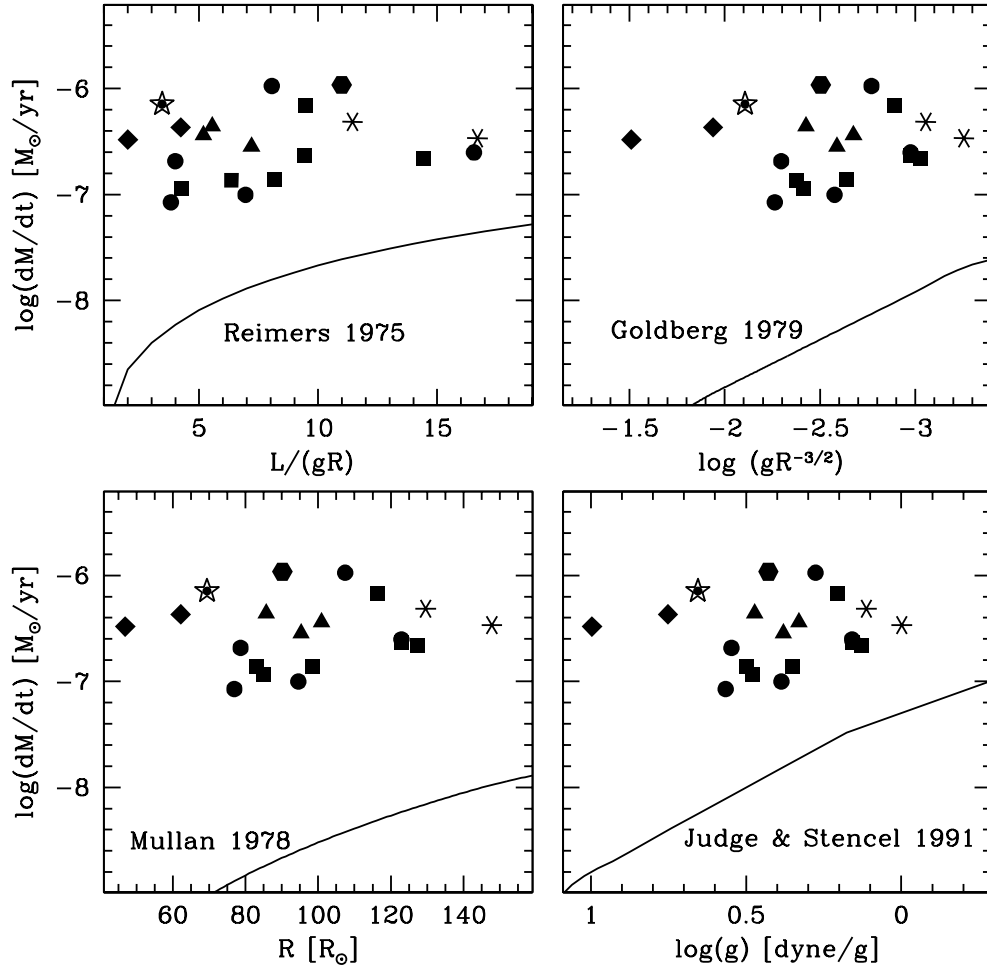
Figure 2.7: ML rates for the giant stars with dust excess, as a function of different stellar parameters. Symbols as in Figure 2.5. The position of the V42 long period variable of ω Cen is also marked. Different empirical laws by Reimers (1975a,b), Mullan (1978), Goldberg (1979), and Judge & Stencel (1991), recently revised by Catelan (2000), calibrated on Population I giants of relatively low luminosity, are shown for comparison.

ratio increases when metallicity decreases (van Loon, 2000). Assuming a gas-to-dust mass ratio of 200 in 47 Tuc, the value for the other clusters is scaled accordingly to their metallicity. For the stars with mid-IR excess in the sample the epochs of dust ejection are typically decades and total ML rates between 10^{-7} and 10^{-6} $M_{\odot}\,yr^{-1}$

These inferred ML rates are finally compared with different empirical laws by Reimers (1975a,b), Mullan (1978), Goldberg (1979), Judge & Stencel (1991). The reference formulae are taken from Catelan (2000), who revised the original ones (see section 2.2.1). The inferred ML rates are about one order of magnitude larger than those predicted by these relations and do not show any clear dependence on stellar parameters (see Figure 2.7).

The major astrophysical implication from this pilot project with ISOCAM, are as following:

- significant ML occurs only at the very end of the RGB evolutionary stage and is episodic;

- typical rates are in the range $10^{-7} < dM/dt < 10^{-6} M_{\odot}\,yr^{-1}$;

- the modulation timescales must be greater than a few decades and less than a million years;

- there is evidence for dusty shells at even the lowest metallicities but ML rates do not show a strong dependence on the cluster metallicity.

However, the ISOCAM survey suffered from a few major limits, namely *i)* the small sample of observed clusters and the consequent overall number of giants allowed to reach only weak conclusions on the ML dependence on metallicity and HB morphology; *ii)* the modest spatial resolution and coverage prevented the study the innermost region of the most concentrated clusters and thus did not allow us to sample a major fraction of the light in the most distant clusters; *iii)* a relatively large absolute photometric uncertainty (≈ 0.5 dex) limited our ability to measure lower ML rates near the RGB tip and our ability to explore ML much below the RGB tip.

2.4   Other ML diagnostics

The detection of outflow motions in the outer regions of stellar atmosphere is the other major ML diagnostic in giant stars.

The investigation of chromospheric lines in giants started in the '80: spectroscopic surveys of a few hundred GC red giants (Cohen, 1976, 1978, 1979, 1980, 1981; Mallia & Pagel, 1978; Peterson, 1981, 1982; Cacciari & Freeman, 1983; Gratton et al., 1984) did reveal Hα emission wings in a good fraction of bright stars. This was initially interpreted as evidence of an extended atmosphere, i.e. of ML.

However, Dupree et al. (1984) demonstrated that this emission is not an unambiguous ML indicator, as it could arise naturally in a static stellar chromosphere, or it could be influenced by hydrodynamic processes due to pulsation (Dupree et al., 1994). Evidence of mass motions in the chromosphere of stars is then sought from blueshifts in the absorption cores or asymmetries in the line profiles of the Na I D and Hα lines or differences in strength between the blue and red emission wings of the Hα profile (Smith & Dupree, 1988).

So, profile asymmetry and coreshifts of chromospheric lines can reveal mass motions, and in particular the presence of a stellar wind and circumstellar material. Red giants in globular clusters were found to exhibit low velocity shifts in the cores of the Hα or Na I D lines (Peterson, 1981; Bates et al., 1990, 1993); similarly, metal-poor field giants, which might be taken as the field counterparts of GC giants, also indicate slow outflow from the asymmetries and line shifts in the Hα, Ca II and Mg II lines (Smith et al., 1992; Dupree & Smith, 1995).

A good diagnostic of winds is the near-infrared He I 10830 Å line which models show (Dupree et al., 1992) is formed higher in the metal-poor atmosphere than Hα and Ca II K. Thus it might be expected to trace out higher velocities, where the outflow becomes a wind, than the optical diagnostics. The first detection of a wind in a metal-deficient star using the He I 10830 Å line was made by Dupree et al. (1992) in a bright field giant, where an outflow of 90 km s^{-1} was discovered, a value comparable to the cromospheric escape velocity. Subsequently, Smith et al. (2004) identified He I absorption from one warm AGB star in the GC M13 in addition to two other metal-poor field giant stars. A stellar T_{eff} greater than 4500 K appeared required to populate the lower level of the He I atom; thus Smith et al. (2004) suggested that the coolest red giant cannot produce this transition. Indeed, He I 10830 Å line was not detected in the five coolest red giants observed in M13. So, while GC stars themselves remain ideal targets, the metal-deficient field giants are

brighter, more accessible to current instrumentation, and can act as surrogates of cluster stars.

Two RGB stars in NGC 6752 were studied by Dupree et al. (1994), by a detailed analysis of the Mg II, Ca II K and Hα line profiles. These stars are at the RGB tip, and the Ca II K and Hα core shifts again revealed slow (≤ 10 km s^{-1}) outflow motions. The asymmetries in the Mg II lines, however, indicated under certain assumptions a stellar wind with a terminal velocity of ~ 150 km s^{-1}, exceeding both the stellar photospheric escape velocity (55 km s^{-1}) and the escape velocity from the cluster core (~ 23 km s^{-1}). The ML rate estimated by Dupree et al. (1994) from the Mg II results ($\sim 10^{-9}$ M$_\odot$yr^{-1}) would lead to a total ML of ~ 0.2 M$_\odot$ over the star lifetime on the RGB ($\sim 2 \times 10^{-8}$ yr), in very good agreement with the expectations of the stellar evolution theory. This result alone is not sufficient to meet the requirements of the stellar evolution that all stars suffer some degree of ML during the phases preceding the HB. However, it shows that the ML phenomenon along the RGB does indeed occur, even if perhaps only occasionally and detected among the brightest stars, and it may be revealed using visual indicators, although less effectively and accurately than using chromospheric lines in the UV such as the Mg II, or in the near-IR such as the He I at 10830 Å (Dupree et al., 1992).

Lyons et al. (1996) discussed the Na I D and Hα stellar profiles for a sample of 63 RGB stars in 5 GC (M 4, M 13, M 22, M 55 and Ω Cen), and found evidence of significant Na I D core shifts in 50% of the stars brighter than log L/L$_\odot \sim 2.9$, whereas significant H core shifts were detected in 50% of the stars brighter than log L/L$_\odot \sim 2.5$. These coreshifts are all ≤ 10 km s^{-1}, i.e. much smaller than the escape velocity from the stellar photosphere ($\sim$ 50-60 km s^{-1}).

Cacciari et al. (2004) have presented the results of the first observations of RGB stars in NGC 2808, obtained with the multi-fiber spectrometer FLAMES, during the Science Verification. FLAMES allows a much more efficient monitoring of visual diagnostics of mass outflow along the RGB over a large magnitude range down from the RGB tip, especially in terms of sample size. In fact a total of 137 stars was observed, of which 20 at high resolution ($R = 47000$) with UVES and the other at lower resolution ($R = 19000-29000$) with GIRAFFE in MEDUSA mode, monitoring $\sim$ 3 mag down from the RGB tip. Evidence of mass motions in the atmospheres was searched from

asymmetry in the profiles and coreshifts of the Hα, Na I D and Ca II K lines, as well as from Hα emission wings. This is by far the largest and most complete collection of such data in GC giants, both for the number of stars observed within one cluster, and for monitoring all the most important optical diagnostics of chromospheric activity/mass motions. Cacciari et al. (2004) have found that, although some diagnostics (e.g. Hα emission) may not provide an unambiguous interpretation, other diagnostics give clear indications of the presence of both chromospheres and mass outflows in the atmospheres of these stars. However, they did not attempt to derive any estimate of ML rate.

Using the same data set, Mauas, Cacciari, Pasquini (2006) compare the observed profiles of the Ca II K and Hα lines with theoretical profiles from suitable model chromospheres. They find that the observed profiles are better described if a negative (outward) velocity field is included in the model chromospheres. They estimate ML rates of a few $10^{-9}\,\mathrm{M_\odot yr^{-1}}$.

Finally, using NIRSPEC on the Keck 2 telescope, Dupree et al. (2009) obtained echelle spectra of He I 10830 Å line for 41 metal-deficient field giant stars including those on red giant branch, asymptotic giant branch and red horizontal branch. They detected fast outflow from the majority of the stars and about 40 % of the outflows have sufficient speed as to allow escape material from the star as well as from a GC. Dupree et al. (2009) found gas outflow in every luminous giant, and estimated ML ranging from $\sim 3 \times 10^{-10}$ to $\sim 6 \times 10^{-8}\,\mathrm{M_\odot yr^{-1}}$.

In summary, the chromospheric method seems very effective in tracing the region of wind formation and acceleration.

However, it is difficult to convert such a line diagnostics into ML rates, not only because of modeling issues, but also because the sampled outflow region is too close to the star, while the bulk of ML is concentrated at larger distances from the star.

Finally, to see asymmetries and coreshift in the spectra of stars at the HB level it's required an high-resolution and high S/N spectra, and they can be obtained only for the nearest GGCs; but also in this case, because the fraction of stars with excess is very small (about 5-10 stars at the HB level) it's necessary to obtain spectra of a large samples in order to detect stars with excess. So, it is expensive to impossible to obtain high-resolution, high S/N spectra of Population II giants along the entire RGB extension.

Chapter 3

The Spitzer Space Telescope

3.1 Infrared astronomy

Observations covering the entire range of wavelengths are either difficult or impossible from the ground due to Earth's atmosphere being opaque to most wavelength regions outside of the visible and radio bands. This is also the case for infrared radiation. Figure 3.1 shows the transparency of the atmosphere as a function of wavelength.
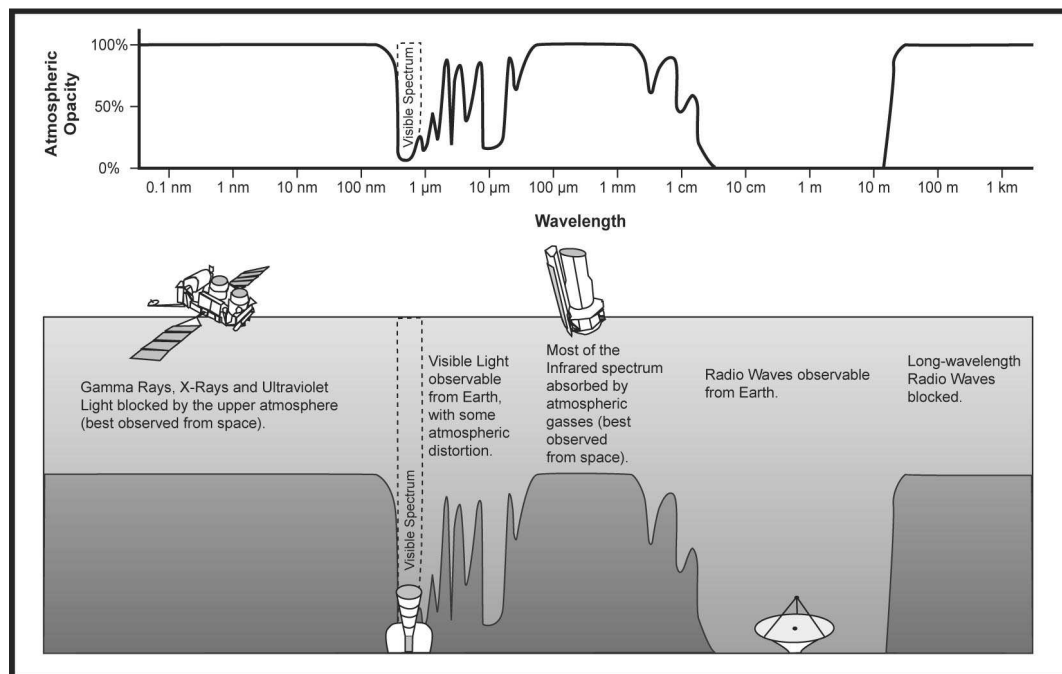

Figure 3.1: The trasparency of Earth's atmosphere as a function of wavelength.

The infrared region can be divided into near-infrared (1.5-5 μm), mid-infrared (5-30 μm), and far-infrared (30 μm to 1 mm). Beyond 1 mm we enter

the realm of radio astronomy.

The atmosphere in the infrared region has a complex and strong absorption spectrum, mostly due to H_2O (all over the spectrum), CO_2, N_2O and O_3. The concentration of these constituents (particularly H_2O) varies from site to site and from time to time at a given site, which results in a spectrum of broad and deep absorptions which, in some cases, totally block the radiation in that specific wavelength band. Fortunately a number of narrow regions (called atmospheric windows) between these molecular bands do exist, where the radiation can reach the ground. Within these windows the IR photometric system (JHKLMNQ) has been defined. Table 3.1 lists the properties of these bands. A large part of the disturbance by the atmosphere can be eliminated

Banda	λ_0 (μm)	$\Delta\lambda$ (μm)
J	1.25	0.38
H	1.65	0.48
K	2.20	0.70
L	3.50	1.20
M	4.80	0.80
N	10.0	8.0
Q	20.0	10.0

Table 3.1: Characteristics of the JHKLMNQ system

by doing infrared observations from aircrafts, balloons or satellites.

In the IR not only absorption is a problem. The sky and the telescope are also emitters of IR radiation: this emission peaks at about 15 μm, close to a very good atmospheric window. This atmospheric emission is not only strong, but also variable (this is even so at balloon altitudes, where absorption becomes very low) and sets the minimum background levels which is received by the detector. The major problem arising from the sky emission is that it is rather nonuniform and affected by large-scale spatial gradients, which translate into temporal variation. In other words, the noise associated with sky emission is not restricted to photon noise only. Since the sky emission is much less than that from the telescope itself, such gradients can be detected only through a *beam-switching* technique[1]. Nonuniform emission combined with scintillation results in excess noise, commonly called *sky noise*. This is the dominant source of noise in the 5-30 μm region.

---

[1]Briefly, the technique consist in moving the telescope from sky+stars to sky.

Local radiation at ambient temperature may also disturb the measurements. At 10 μm, objects at room temperature radiate prominently, and so do telescope mirrors and telescope support structures. Therefore the telescope must be of specific design so that no "warm" surface is seen by the detector. All components which cannot be hidden (filters for example) have to be cooled to very low temperatures. Still, the mirrors of the telescope, and the telescope support structure, contribute to background radiation.

Infrared astronomy started in the 1960s, when balloon-borne telescopes were placed above the Earth's lower atmosphere. By the early 1970s, measurements made by small telescopes on board high-flying Lear jets and on sounding rockets identified a few thousand celestial infrared (IR) sources.

In the meantime, astronomers started to explore narrow atmospheric windows from the ground where transmission is sufficiently good. New infrared instruments were mounted on telescopes at Mauna Kea in Hawaii, at Mount Wilson in Southern California, and at Mount Lemmon in Arizona. NASA converted a cargo plane into the Kuiper Airborne Observatory (KAO) in 1974, and this flying platform provided research flights for infrared astronomers over the next two decades.

None of these observatories, however, could take advantage of the pristine observing conditions of space. By the early 1970s, astronomers began to consider the possibility of placing an infrared telescope above the Earth's atmosphere.

On January 25, 1983 it was launched the first infrared telescope into space: the InfraRed Astronomical Satellite (**IRAS**), an Explorer-class satellite designed to perform the first IR survey of the sky. It was a collaborative effort between the United States, the Netherlands, and the United Kingdom. The American team constructed the telescope, infrared detectors, and cooling system. The Dutch team provided the spacecraft, which included the on-board computers and pointing system. The British built the satellite ground station and control center. IRAS scanned more than 96 percent of the sky four times, providing the first high sensitivity all sky map at 12, 25, 60 and 100 microns wavelengths. IRAS detected about 500000 infrared sources, doubling the number of cataloged astronomical sources. IRAS discoveries included a disk of dust grains around the star Vega, six new comets, and very strong infrared emission from interacting galaxies and from warm dust called infrared

cirrus which could be found in almost every direction of space. IRAS also revealed for the first time the internal region of the Milky Way, as well as its many star forming region. The 10-month IRAS mission was a spectacular success.

Several successful infrared satellite missions were launched after IRAS. During July and August of 1985, an infrared telescope was carried onboard the Space Shuttle's Spacelab 2 to complement observations made by the IRAS mission. This mission produced a high quality map of about 60% of the Galactic plane.

In November 1989, NASA launched the **COBE** satellite to study both infrared and microwave characteristics of the cosmic background radiation (the remains of the extreme heat that was created by the Big Bang). Over a ten month period, COBE mapped the brightness of the entire sky at several infrared wavelengths and discovered that the cosmic background radiation is not entirely smooth, showing extremely small variations in temperature. These variations may have led to the formation of galaxies.

The Infrared Telescope in Space (**IRTS**), launched in March 1995, was Japan's first infrared satellite mission. During its 28 day mission, IRTS surveyed about 7% of the sky with four instruments: a Near and Mid-IR Spectrometer which covered wavelengths of 1.4 to 4 microns and 4.5 to 11 microns respectively, a Far-IR Line Mapper which studied Oxygen and Carbon spectral lines at 63 and 158 microns, and a Far-IR Photometer which studied the sky in four bands centered at 150, 250, 400, and 700 microns. This data should add to our knowledge of cosmology, interstellar matter, late type stars and interplanetary dust.

The European Space Agency launched the Infrared Space Observatory (**ISO**) in November 1995. ISO, which observed at wavelengths between 2.5 and 240 microns, not only covered a much wider wavelength range than IRAS but was also thousands of times more sensitive than IRAS and viewed infrared sources with much better spatial and spectral resolution. ISO was equipped with 4 instruments, two spectrometers (SWS and LWS), a camera (ISOCAM) and an imaging photo-polarimeter (ISOPHOT):

- Short Wave Spectrometer (SWS) - A spectrometer covering the 2.4 to 45 mum wavelength. Observation with this instrument provided valuable information about the chemical composition, density and temperature of

the universe.

- Long Wave Spectrometer (LWS) - A spectrometer covering the 45 to 196.8 mum wavelength. This instrument did essentially the same as the SWS, but looked at much cooler objects than SWS did. Particularly cold dust clouds between stars were studied with this instrument.

- Infrared Camera (ISOCAM) - A high-resolution camera covering 2.5 to 17 mum wavelength with two different detectors.

- Photo-polarimeter (ISOPHOT) - An instrument designed to measure the amount of infrared radiation emitted from an astronomical object. The very broad wavelength range from 2.4 to 240 mum allowed this instrument to see the infrared emissions of even the coldest astronomical objects such as interstellar dust clouds.

ISO took data for about 2.5 years (a period 3 times longer than IRAS). It ceased operations in April 1998 when its supply of liquid helium ran out.

The Midcourse Space Experiment (**MSX**) was launched in April 1996 and lasted until its liquid helium coolant ran out in Feb 1997. During its 10 months of operation, MSX gathered a vast amount of data at 4.2 - 26 microns. MSX studied the infrared emission from the gas and dust which permeates the universe. MSX had 30 times the spatial resolution of IRAS and surveyed areas of the sky which were missed by IRAS.

AKARI was the second space mission for infrared astronomy in Japan. AKARI has a 68.5 cm telescope cooled down to 6K, and observed in the wavelength range from 1.7 to 180 mum. The AKARI mission is an ambitious plan to make an all-sky survey with much better sensitivity, spatial resolution and wider wavelength coverage than IRAS. AKARI is equipped with two instruments: the FIS (Far-Infrared Surveyor), for far-infrared observations (wavelengths range from 50 to 180 mum), and the IRC (InfraRed Camera) for near (1.7-5.5 mum range) and mid-IR (12.4-26.5 mum range) observations. AKARI was launched on February 21, 2006. The satellite ran out of its on-board supply of cryogen on August 26,2007. The boil off of the liquid Helium signaled the completion of observations at far-infrared and mid-infrared, including the all-sky survey. It is currently entering a two week phase of final orbit insertion, in-orbit check out and instrument verification.

3.2   The Spitzer mission

The Spitzer Space Telescope (formerly SIRTF, the Space Infrared Telescope Facility) is the final mission in NASA's Great Observatories Program - a family of four orbiting observatories, each observing the Universe at different wavelengths (visible, gamma rays, X-rays, and infrared). Other missions in this program include the Hubble Space Telescope (HST, launched on 1990), Compton Gamma-Ray Observatory (CGRO, 1991–2000), and the Chandra X-Ray Observatory(CXO, launched on 1999). Spitzer is also a part of NASA's Astronomical Search for Origins Program, designed to provide information which will help us understanding our cosmic roots, and how galaxies, stars and planets develop and form.

The Spitzer Space Telescope consists of a 0.85-meter diameter telescope and three cryogenically-cooled science instruments which will perform imaging and spectroscopy in the 3 - 180 micron wavelength range (1 micron is one-millionth of a meter). Using the latest in large-format detector arrays, Spitzer will be able to make observations that are more sensitive than any previous mission. Spitzer was launched into space by a Delta rocket from Cape Canaveral, Florida on 25 August 2003. While Spitzer's mission lifetime requirement remains 2.5 years, recent developments have brought a 5-year mission within reach. After more than five-and-a-half years of probing the cool cosmos, Spitzer entered an inactive state called standby mode at 3:11 p.m. Pacific Time (6:11 p.m. Eastern Time or 22:11 Universal Time), May 15, as result of running out of its liquid helium coolant. Scientists and engineers then are re-calibrating the instrument at the warmer temperature, and preparing it to begin science operations.

During its mission, Spitzer have obtained images and spectra by detecting the infrared energy, or heat, radiated by objects in space from the near to the far infrared. Most of this infrared radiation is blocked by the Earth's atmosphere and cannot be observed from the ground.

Spitzer is the largest infrared telescope ever launched into space. Its highly sensitive instruments give us a unique view of the Universe and allow us to peer into regions of space which are hidden from optical telescopes. Many areas of space are filled with vast, dense clouds of gas and dust which block our view. Infrared light, however can penetrate these clouds, allowing us to peer into regions of star formation, the centers of galaxies, and into newly forming
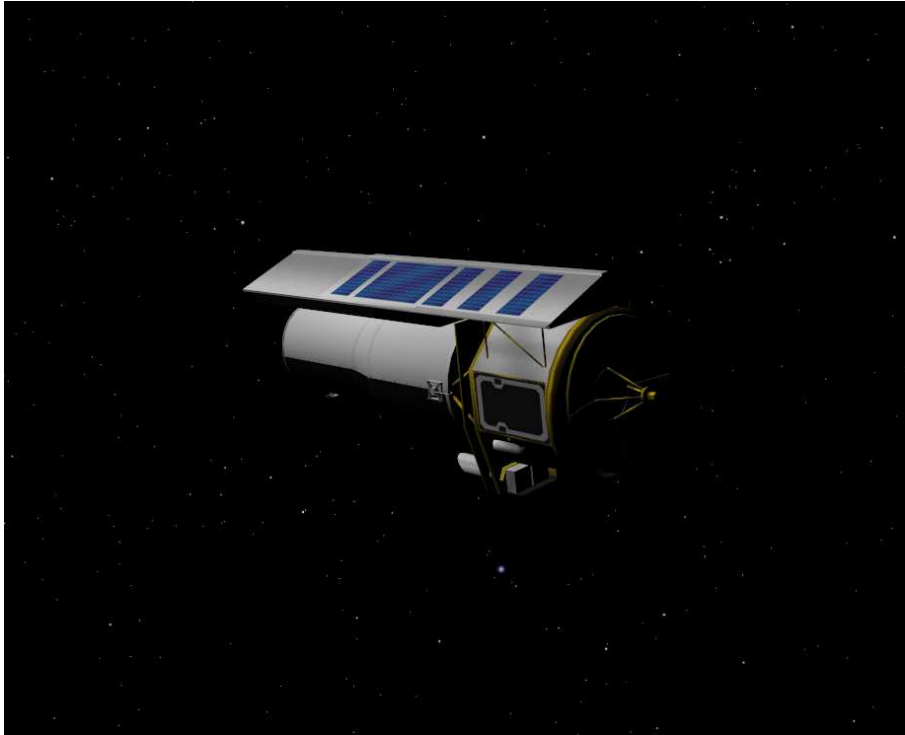
Figure 3.2: Artistic image of Spitzer.

planetary systems. Infrared also brings us information about the cooler objects in space, such as smaller stars which are too dim to be detected by their visible light, extrasolar planets, and giant molecular clouds. Also, many molecules in space, including organic molecules, have their unique signatures in the infrared.

Because infrared is primarily heat radiation, the telescope must be cooled to near absolute zero (-459 degrees Fahrenheit or -273 degrees Celsius) so that it can observe infrared signals from space without interference from the telescope's own heat. Also, the telescope must be protected from the heat of the Sun and the infrared radiation put out by the Earth. To do this, Spitzer carries a solar shield and was launched into an Earth-trailing solar orbit. This unique orbit places Spitzer far enough away from the Earth to allow the telescope to cool rapidly without having to carry large amounts of cryogen (coolant). This innovative approach has significantly reduced the cost of the mission.

3.3 Spitzer Technology

The Spitzer telescope is a lightweight reflector of Ritchey-Chrètien design. It weighs less than 50 kg and is designed to operate at an extremely low

temperature. The telescope has an 85 cm diameter aperture. All of its parts, except for the mirror supports, are made of light-weight beryllium. Beryllium is a very strong material which works well in the construction of infrared space telescopes because it has a low heat capacity at very low temperatures. The telescope characteristic are summarized in Table 3.2.

Aperture (diameter)	85 cm
Cryogenic Lifetime	$\sim$ 5 years
Wavelength Coverage	3.6–160 μm (imaging)
	5.3–40 μm (spectroscopy)
	55–95 μm (spectral energy distribution)
Diffraction Limit	5.5 μm
Image Size	1.5$''$ at 6.5 μm
Field of view (of imaging arrays)	$\sim$ 5'$\times$5' (each band)
Telescope Minimum Temperature	5.6 K

Table 3.2: Summary of Spitzer Characteristics

The telescope is attached to the top of the vapor-cooled cryostat vacuum shell, which keeps the science instruments very cold. The telescope and cryostat shell are launched warm, and cool down once in orbit. Since infrared is primarily heat radiation, detectors are most sensitive to infrared light when they are kept extremely cold. If the instruments are not very cold, the heat from the instruments themselves will interfere with the study of the faint infrared radiation from objects in space. Spitzer's cryostat will keep the science instruments at temperatures as low as 1.4 degrees Kelvin for up to 5 years. Spitzer's cryostat will keep the instruments cold by venting helium vapor from a liquid helium tank. The cryostat consists of the vacuum shell, inner and middle vapor cooled shields, helium tank, and the fluid management system. The tank holds about 360 liters of super-fluid helium.

Spitzer's science payload consist of three cryogenically-cooled instruments, which together offer observational capabilities stretching from the near to the far infrared: **IRAC**, **IRS** and **MIPS**.

The infrared array camera (IRAC) is a four channel camera that provides simultaneous 5.2 x 5.2 arcmin images at 3.6, 4.5, 5.8, and 8 microns. Each of the four detector arrays in the camera are 256 x 256 pixels in size. IRAC uses two sets of detector arrays. The two short-wavelength channels are imaged by composite detectors made from

indium and antimony. The long-wavelength channels use silicon detectors that have been specially treated with arsenic.

The Infrared Spectrograph(IRS) provides both high- and low-resolution spectroscopy at mid-infrared wavelengths. Spectrometers are instruments which spread light out into its constituent wavelengths creating a spectra. Within this spectra, astronomers can study emission and absorption lines: which are the fingerprints of atoms and molecules. The IRS has four separate modules: a low-resolution, short-wavelength mode (SL) covering the 5.3-14 micron interval with spectral resolution R$\sim$60-127; a high-resolution, short-wavelength mode (SH) covering 10-19.5 microns with spectral resolution R$\sim$600; a low-resolution, long-wavelength mode (LL) for observations at 14-40 microns with spectral resolution R$\sim$57-126; and a high-resolution, long-wavelength mode (LH) for 19-37 microns with spectral resolution R$\sim$600. Each module has its own entrance slit to let infrared light in. The detectors are 128 x 128 arrays. The shorter-wavelength silicon detectors are treated with arsenic; the longer-wavelength silicon detectors are treated with antimony. The pixel scale is 1.8″ in the SL mode, 5.1″ in the LL mode, 2.3″ in the SH mode and 4.5″ in the LH mode. From short to long ramp time, the approximate median bright source limit is 50-10 mJy (SL), 130-100 mJy (LL), 540-90 mJy (SH), 620-350 mJy (LH). The IRS has two mode of operation: the spectral staring (spectrum of an individual fixed or moving target or spectra of multiple fixed or moving targets within 1°) and mapping mode (multiple spectra from a 2-D spatial region in user-defined steps parallel and/or perpendicular to one or more slit). In both cases the target is acquired and then observed in a fixed sequence starting with SL2 (Short-Low second-order), SL1, SH, LL2, LL1, LH, skipping any unrequested slits. The IRS SL module contains also two peak-up imaging fields. Their field of view is 55″×80″, with a scale of 1.8″ per pixel. IRS peak-up mode enables the placement of a source on a spectrographic slit or series of slits more accurately than just using blind pointing of the spacecraft alone. The allowed ranges of flux densities for blue and red peak-up point sources are f_{blue} = 0.8-150 mJy and f_{red} = 1.4-340 mJy, respectively. The IRS instrument consists of two physically separated parts, the cold assemblies which are located within the Spitzer multiple

instrument chamber and the warm electronics, which are located in the
Spitzer spacecraft bus. The IRS has no moving parts!

The Multiband Imaging Photometer for Spitzer (MIPS) provides
imaging and limited spectroscopic data at far-infrared wavelengths. It
has three detector arrays. A 128 x 128 array for imaging at 24 microns
is composed of silicon, specially treated with arsenic. A 32 x 32 array for
imaging at 70 microns, and a 2 x 20 array for imaging at 160 microns
both use germanium, treated with gallium. The 32 x 32 array will also
take spectra from 50 - 100 microns. The MIPS field of view varies from
about 5x5 arcmin at the shortest wavelength to about 0.5x5 arcmin at the
longest wavelength. The instrument resolution is $6''$, $18''$ and $40''$ at 24,
70, and 160 μm, respectively. Under optimal conditions, the 5σ detection
limits on point sources in 500 s of integration at 24, 70, and 160 μm
are 0.11, 6, and 15 mJy, respectively. The three arrays, calibrators, scan
mirror, and optics compose the cryogenic part of the MIPS. This assembly
is mounted in the Spitzer cold instrument chamber. In addition, the
MIPS and the IRS share warm electronics that controls their operation.
The only moving part in MIPS is a scan mirror used to efficiently map
large areas of the sky.

3.4   The infrared array camera (IRAC)

In this section we put more attention on the infrared array camera, because in
this thesis we analyzed a sample of IRAC images. In fact, as CS dust condenses
in an outflowing wind, it can be detected by mid-IR excess. IRAC bands
between 3.6 and 8 μm are effective in detecting this dust, particularly when
coupled with ground-based near IR photometry in the J, H, K bands which
is used to classify the stellar counterpart and account for the photospheric
contribution. MIPS observations at 24 μm could provide complementary
information on the cooler dust, but the spatial resolution of this instrument is
too low and exposure times tend to be prohibitive. IRS again is not useful both
because giants star in GC are too faint and because it's be really expensive
to obtain spectra of all the RGB stars from the tip to the HB. Eventually it
could be used in follow up studies, after selected the stars whit IR excess.

IRAC is a four-channel camera that provides simultaneous $5.2' \times 5.2'$

images at 3.6, 4.5, 5.8, and 8 microns. Two adjacent fields of view are imaged in pairs (3.6 and 5.8 microns; 4.5 and 8.0 microns) using dichroic beamsplitters. All four detector arrays in the camera are 256×256 pixels in size, with a pixel size of $1.2' \times 1.2'$. The two short wavelength channels use InSb detector arrays and the two longer wavelength channels use Si:As detectors. The system parameters are summarized in Table 3.3 and Figure 3.3.

The IRAC instrument was designed to address the four major scientific objectives defining the Spitzer mission. These are (1) to study the early universe, (2) to search for and study brown dwarfs and super-planets, (3) to study ultra-luminous galaxies and active galactic nuclei, and (4) to discover and study protoplanetary and planetary debris disks. The utility of IRAC is in no way limited to these objectives, which we only mention to explain the scientific drivers for the instrument design. IRAC is a powerful survey instrument because of its high sensitivity, large field of view, mapping capabilities, and simultaneous four-color imaging.

Channel	Effective λ (μm)	Bandwidth (μm)	Read noise e^- (12 sec)	Saturation DN	Gain (e^-/DN)	Conversion factor (e^-/sec)/(MJy/sr)
1	3.550	0.681	9.4	43939	3.3	25
2	4.493	0.872	9.4	37838	3.7	29
3	5.731	1.250	8.8	44737	3.8	14
4	7.872	2.526	6.7	52632	3.8	29

Table 3.3: IRAC characteristics.

3.4.1   The IRAC BCD pipeline

The IRAC BCD (Basic Calibrated Data) pipeline is designed to take a single raw image from a single IRAC detector and produce a flux-calibrated image which has had all well-understood instrumental signatures removed. The Basic Calibrated Data (BCD) are the calibrated, individual images. These are in array orientation and have a size of 256×256 pixels for the full array images, and 64 planes times 32×32 pixels for the sub-array images. These data are fully calibrated and have detailed file headers.

The IRAC pipeline consists of two principal parts: the data reduction modules and the calibration server. Individual modules are written as stand-alone code and each corrects a single instrumental signature. Each module uses FITS files and text configuration files as input and produces one or more
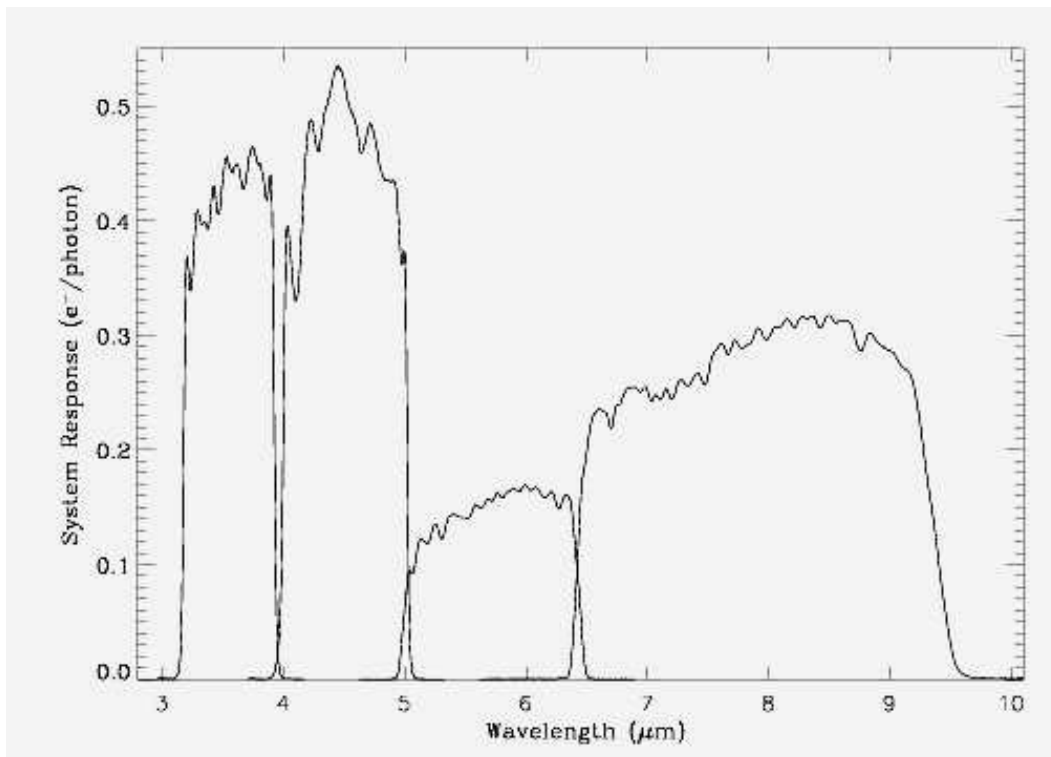
Figure 3.3: IRAC total system response, including transmission of the optics and quantum efficiency of the detectors.

FITS files and log files as output.

The principal instrumental noises corrected by the pipeline are:

Dark current The detector dark currents are generally insignificant compared to the sky background. However, there is a significant offset or bias in a dark frame, and which therefore must be subtracted from the observations. The average dark current is <0.1, 0.28, 1, and 3.8 e^-/s for channels 1, 2, 3, and 4, respectively. Due to the decision not to use the photon-shutter on the IRAC for dark and flat measurements, the dark subtraction procedure is very sophisticated. There will be two steps for the dark subtraction, one using a dark from the ground-based laboratory measurements (called, "lab darks"), and another using a delta dark which is the difference between the lab dark and the sky dark measured at the low zodiacal light region.

Residual image After observing a bright source, a residual image will remain on the array in subsequent frames. In pre-launch laboratory testing, has been found that after taking a 30 sec frame on a very bright lamp, the residual image in the next 30 sec frame had an amplitude (relative to full well) of 0.6%, 1.1%, 2.1%, and 3.7% in channels 1, 2, 3, and 4, respectively. The residual image decayed and became indistinguishable within 270 sec.

Detector linearization Like most detectors, the IRAC arrays are non-linear near full-well capacity. The number of read-out DN is not proportional to the total number of incident photons, rather it becomes increasingly small as the number of photons increases. In IRAC, if fluxes are at levels above half full-well (typically 20-30000 DN in the raw data), they can be non-linear by several percent. During processing the raw data is linearized on a pixel-by-pixel basis using a model derived from ground-based test data and re-verified in flight.

Flat-fielding Like all imaging detectors, each of the IRAC pixels has an individual response function. To account for this pixel-to-pixel responsivity variation, each IRAC image is divided by a map of these variations, called a "flat-field". Observations are taken of pre-selected regions of high-zodiacal background with relatively low stellar content located in the ecliptic plane. They are dithered frames of 100 seconds

in each channel. These observations are processed in the same manner
as science data and then averaged with outlier rejection. This outlier
rejection includes a sophisticated spatial filtering stage to reject the
ever-present stars and galaxies that fill all IRAC frames of this depth.
The result is a smoothed image of the already very uniform zodiacal
background. This "skyflat" is similar to flat-fields taken during ground-
based observations. The flat-fields are then normalized to one.

After instrumental noises correction, individual frames are analyzed to
remove probable cosmic rays. Then follow the sky and zodiacal background
subtraction: a pre-selected region of low zodiacal background in the north
ecliptic cap is observed in order to create a "skydark"; then, for each image,
the zodiacal background will be estimated (a constant for the entire frame)
based on the pointing and time that the data is taken. Finally, the IRAC data
are calibrated in units of MJy sr^{-1}. This is accomplished by multiplying the
data image by a conversion factor provided by the calibration server (see next
3.4.2 and Table 3.5).

All processing of IRAC data beyond the individual, calibrated, $256 \times$
256 images produced by the BCD science pipeline is called "post-BCD". This
includes combining all images from an AOR into a mosaic, detecting sources,
and any cosmetic corrections to the images (individual or mosaic) that are not
based on understood instrumental artifacts or detector physics.

3.4.2   Absolute calibration of the Infrared Array Camera

The Infrared Array Camera (IRAC) on the Spitzer Space Telescope is
absolutely calibrated by comparing photometry of a set of A main-sequence
and K giant stars (primary calibrators) near the north ecliptic pole to
predictions based on ground-based observations and a stellar atmosphere
model. The primary calibrators (Table 3.4) were chosen from a larger list
of candidates on the basis of having good spectral and photometric data and
no known evidence of variability (Megeath et al., 2003).

For each primary calibrator, we predicted the count rate in each IRAC
channel. The procedure was explained in detail by Cohen et al. (2003). In
brief, the spectral type of each star was determined from ground-based visible
spectroscopy (Megeath et al., 2003). The intrinsic spectral energy distribution
for that type was determined from models for the A stars (Kurucz, 1993a,b) or

Calibrator	Type	A_v	K_s	[3.6]	[4.5]	[5.8]	[8.0]
NPM1p64.0581	A0 V	0.387	9.117	9.123	9.104	9.107	9.122
HD 165459	A1 V	0.285	6.584	6.593	6.575	6.579	6.591
NPM1p60.0581	A1 V	0	9.465	9.666	9.653	9.659	9.669
1812095	A3 V	0.378	11.596	11.275	11.254	11.255	11.265
KF08T3	K0.5 III	0	11.090	10.944	10.968	10.985	10.943
KF09T1	K0 III	0	8.114	8.046	8.087	8.086	8.047
KF06T1	K1.5 III	0	10.987	10.762	10.906	10.833	10.793
KF06T2	K1.5 III	0.189	11.273	11.065	11.193	11.133	11.095
NPM1p66.0578	K1 III	0	8.330	8.249	8.347	8.310	8.335
NPM1p67.0536	K2 III	0.161	6.409	6.306	6.428	6.389	6.348
NPM1p68.0422	K2 III	0.462	6.816	6.712	6.822	6.780	6.742

Table 3.4: IRAC primary absolute calibrators.

from empirical spectral templates derived from observations for the K giants (Cohen et al., 1996).

For each star, an absolute normalization and the extinction were derived by fitting the intrinsic SED to optical (UBV, Hipparcos H_p , Tycho-2 B_t and V_t), near-infrared (Two Micron All Sky Survey-2MASS), and mid-infrared (IRAS, MSX) photometry. Table 3.4 shows the 2MASS K_s magnitudes (Skrutskie 1999),the derived extinction for each primary calibrator and the obtained IRAC magnitudes. The fluxes in the IRAC wavebands were calculated by integrating the normalized spectral template for each star over the IRAC spectral response. The number of electrons per unit of time collected from a source with spectrum F_ν using a telescope with area A is

$$N_e = A \int \frac{F_\nu}{h\nu} R_\nu \, d\nu \,,$$

where R_ν is the system spectral response (in units of electrons per photon, at frequency ν, determined from pre-launch measurements). The calibration factor is the ratio of the flux density F_{ν_0} at the nominal wavelength $\lambda_0 = c/\nu_0$, if the source had the nominal $\nu F_\nu = $ constant spectrum, to the observed electron production rate:

$$C = \frac{F_{\nu_0} K G}{N_e f_{ap} \omega_{pixel}} \,,$$

where G is the gain (e$^-$/DN), ω_{pixel} is the pixel solid angle (pixels are square, with 1.22$''$ sides), f_{ap} is the aperture correction factor (taken to be unity), and K is the color correction:

$$K = \frac{\int (F_\nu / F_{\nu_0}) \times (\nu / \nu_0)^{-1} R \, d\nu}{\int (\nu / \nu_0)^{-2} R \, d\nu} \,.$$

In fact, for an imager like IRAC, we calibrate in units of surface brightness, and the flux measurements are made using aperture photometry in a finite aperture that does not necessarily include all of the flux. So we continue to use F_ν as the true source spectrum, and we define the calibration factor such that after performing both aperture and color corrections to the observations, the best measurement of the source flux is obtained. The units of the calibration factor C are $(\text{MJy } sr^{-1})/(\text{DN s}^{-1})$ (remember that $1\text{Jy} = 10^{-26}$ W m^{-2} Hz^{-1} = 10^{-23} erg s^{-1} cm^{-2} Hz^{-1}).

The recommended calibration factors for IRAC were calculated as a weighted average of calibration factors for the four A-type primary calibrators. The results are given in Table 3.5.

Channel	λ	Calibration factor
	(μm)	C
		$(\text{MJy } sr^{-1})/(\text{DN s}^{-1})$
1	3.6	0.1088 ± 0.0022
2	4.5	0.1388 ± 0.0027
3	5.8	0.5952 ± 0.0121
4	8.0	0.2021 ± 0.0041

Table 3.5: Absolute calibration factors for IRAC.

3.4.3   IRAC magnitude system

The IRAC magnitude system is defined such that an observer measures the flux density F_ν of a source from the calibrated images out of the IRAC pipeline, performs image-based corrections (array-location-dependent photometric correction, pixel-phase correction, and aperture correction), and then uses the zero-magnitude flux densities $F_{zero}^{[i]}$ to calculate the magnitude $[i] = 2.5 \log_{10}(F_{zero}^{[i]} / F_\nu)$, where $i = 3.6$, 4.5, 5.8, and 8 are the four IRAC channels. In this system, there is no need to know the spectral shape of the source, as the magnitude is a measure of the in-band flux relative to that of Vega. The zero-magnitude fluxes were determined by integrating the Kurucz model spectrum of α Lyr over the passbands using the equations above; specifically,

$$F_{zero}^{[i]} = \frac{\int F_\nu \, (\nu / \nu_0)^{-1} \, R^{[i]} \, d\nu}{\int (\nu / \nu_0)^{-2} \, R^{[i]} \, d\nu} \, .$$

The resulting zero-magnitude flux densities are 280.9 ± 4.1, 179.7 ± 2.6, 115.0 ± 1.7, and 64.13 ± 0.94 Jy in the [3.6], [4.5], [5.8], and [8] μm channels,

respectively. Due to the choice of A dwarfs as the absolute calibrators, this magnitude convention should yield results on the same scale as used in optical and near-infrared astronomy.

3.5   ML in GCs using Spitzer

As we have seen in the previous Chapter, the amount of dust present in the intracluster medium (ICM) will vary depending on the cluster escape velocity, the time since the last crossing of the Galactic disk in which the ICM could have been stripped away by the ISM, and the number of mass-losing stars. In general the dust in the ICM of GCs is expected to be $\sim 10^{-2}$ to 10^{-3} $M_\odot$ for most GGCs. Previous attempts to detect the ICM in GCs suggest that the ICM density is well below that expected from predictions of the mass loss input from RGB and AGB stars. So, searches for this missing mass are really actually. The high sensitivity of the instruments onboard Spitzer Space telescope has allowed this kind of searches, and in these years a large number of work has been done.

First of all, Boyer et al. (2006) presented an IRAC and MIPS observations of M15, one of the most metal poor GGCs. They reveal a population of dusty red giants (mass-losing AGB and post-AGB stars) near the cluster center, a previously detected planetary nebula, and a possible detection of the ICM from a diffuse emission detected in the Spitzer images at 24 μm. They suggest that $(9 \pm 2) \times 10^{-4}\,M_\odot$ of dust is present in the core of M15, and that this material has accumulated over a period of about 10^{-6} years.

Lebzelter et al. (2006) obtained IRS low-resolution mid-IR (7.6-21.7 μm) spectra of 11 AGB variable stars in the GGC NGC 104. They found significant dust features of various types: a 13 μm feature in spectra of low luminosity AGB stars; more luminous AGB stars show a broad feature a 11.5 μm; finally the spectra of the most luminous stars are dominated by the amorphous silicate bending vibration centered at 9.7 μm.

Boyer et al. (2008) present an IRAC & MIPS imaging survey of the most massive GGC, ω Cen, investigating stellar ML at low metallicity and the ICM. They find that about 140 cluster members show a red excess at 24 μm, indicative of circumstellar dust. They estimate a cumulative ML rate of $2.9 \div 4.2 \times 10^{-7}\,M_\odot \mathrm{yr}^{-1}$. They also find a little evidence for strong ML at lower luminosities along the RGB.

van Loon et al. (2008) used archival IRAC photometry of the old, super-solar metallicity massive open cluster NGC 6791 to look for evidence of enhanced ML, which has been postulated to explain the optical luminosity function and low white dwarf masses.

Boyer et al. (2009) investigate dust production and stellar ML in the GGC NGC 362. Due to its close proximity to the Small Magellanic Cloud, NGC 362 was imaged with the IRAC and MIPS cameras as part of the Surveying the Agents of Galaxy Evolution (SAGE-SMC) Spitzer Legacy program. They detect several cluster members only near the RGB tip that exhibit IR excess indicative of circumstellar dust and conclude that dust in not present in measurable quantities below the tip. They modeled the spectral energy distribution of the stars with the strongest IR excess and find a total cluster dust ML rate of about $3 \times 10^{-9} \, \mathrm{M_\odot yr^{-1}}$.

Finally, Barmby et al. (2009) use MIPS (at 24 and 70 μm) to observe eight GGCs (NGC 104, NGC 362, NGC 1851, NGC 5272 (M3), NGC 5904 (M5), NGC 6205 (M13), NGC 6341 (M92) and NGC 6752) in an attempt to detect the thermal emission from ICM dust. The inferred dust mass and upper limits are less than $4 \times 10^{-4} \, \mathrm{M_\odot}$, well below expectation for cluster dust production from ML in RGB and AGB stars. This implies that either GC dust production is less efficient, or that ICM or dust destruction is more efficient than previously believed.

Chapter 4

Observations and data reduction

4.1 The Spitzer IRAC survey of GGCs

The aim of our project is the detailed study of mass loss in Population II giants down to the HB level in a carefully chosen sample of GGCs, spanning the entire metallicity range from about one hundredth up to almost solar. Our goals are twofold: first, to develop a scaling law calibrated over a wide range of metallicity; second to develop a better physical understanding of mass loss.

The pilot project with ISOCAM showed that the bulk of CS dust around the RGB tip giants typically has temperatures in the range 300–$500\,\mathrm{K}$, if we assume a νB_ν emissivity. The IRAC bands at 5.8 and $8\,\mu\mathrm{m}$ are the most efficient to detect this warm dust. The 3.6 and $4.5\,\mu\mathrm{m}$ bands coupled with ground-based near IR photometry in the J, H, K bands should mainly trace the photospheric contribution.

A sample of 17 massive GGCs, 4–5 per each 0.5 dex bin in metallicity between $[\mathrm{Fe/H}] = -2.3$ and -0.5 and different HB morphologies within each bin, have been observed between September 2005 and July 2006, with IRAC onboard Spitzer with 26 hr of observing time allocated to our program (ID #20298) in Cycle 2. Three color ($3.6\mu\mathrm{m}$ (blue), $6\mu\mathrm{m}$ (green), $8\mu\mathrm{m}$ (red) mosaiced image of the selected clusters are showed in Figures 4.1, 4.2, 4.3.

For all these clusters complementary near-IR and UV photometry are available to properly characterize both the red and the blue sequences. Ground-based near-IR photometry of the central region at high spatial resolution has been obtained using IRAC2@ESO2.2m, SOFI@ESO-NTT and NICS@TNG (Ferraro et al., 2000; Valenti et al., 2004a,b; Sollima et al., 2004) and supplemented with 2MASS data in the external region of each cluster. Accurate WFPC2 and ACS HST UV/optical images of the core regions and
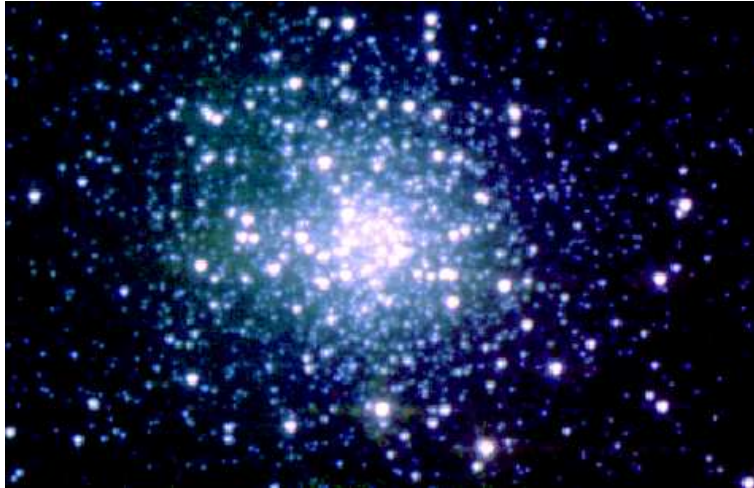
Figure 4.1: Three color (3.6μm (blue), 6μm (green), 8μm (red)) mosaiced image of NGC 104 (47 Tuc).

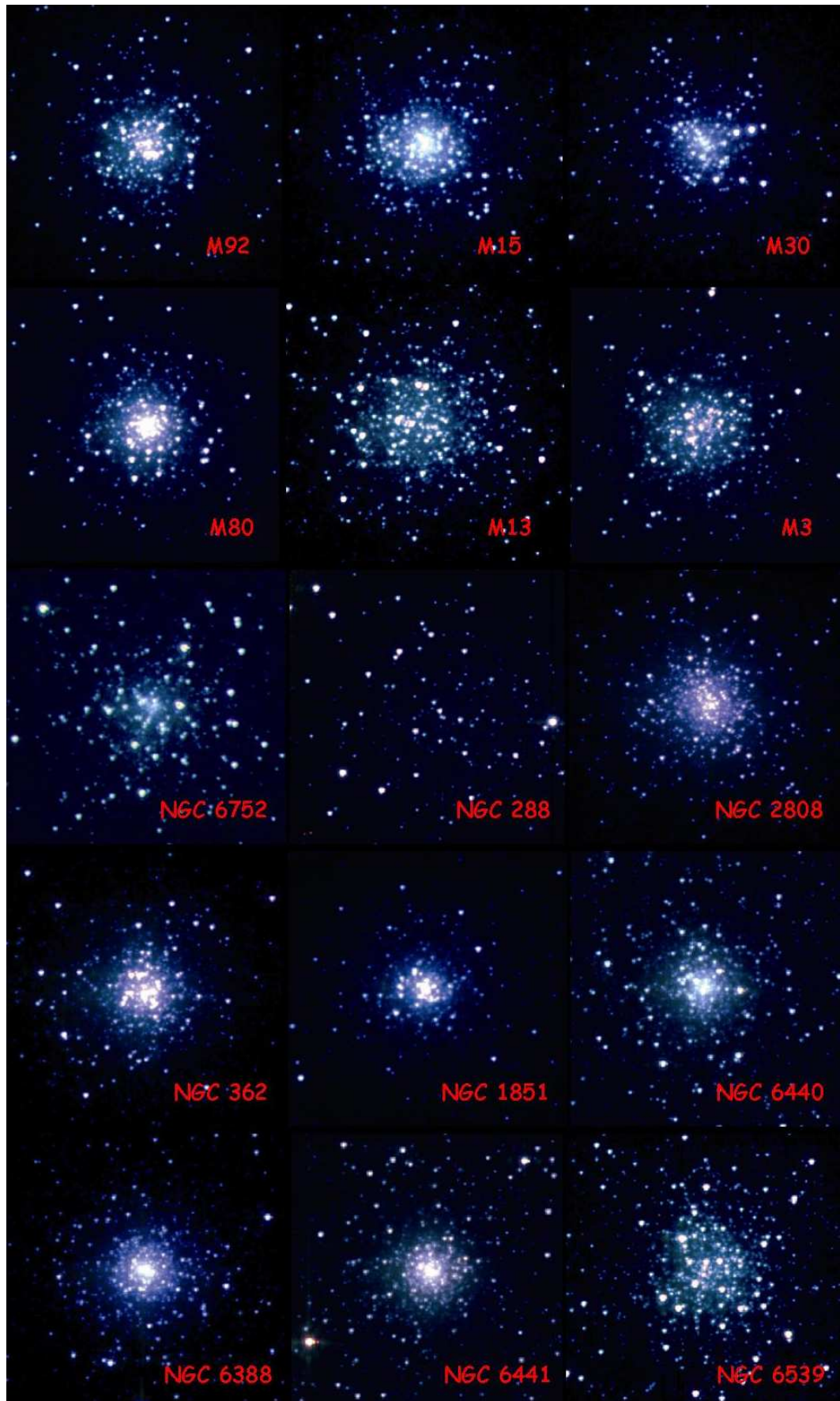Figure 4.2: Three color (3.6μm (blue), 6μm (green), 8μm (red)) mosaiced image of NGC 5139 (ω Cen).

Figure 4.3: Three color (3.6μm (blue), 6μm (green), 8μm (red)) mosaiced image of

Cluster	[Fe/H][a]	$(m-M)_0$[a]	E(B-V)[a]	FOV[b]	t_{exp}[c]
NGC 104 (47 Tuc)	−0.71	13.32	0.04	9'×5'	1.3hr
NGC 288	−1.40	14.73	0.03	5'×5'	1.1hr
NGC 362	−1.28	14.68	0.05	5'×5'	1.1hr
NGC 1851	−1.29	15.46	0.02	5'×5'	2.05hr
NGC 2808	−1.37	14.90	0.23	5'×5'	2.05hr
NGC 5139 (ω Cen)	−1.70	13.60	0.11	14'×5'	1.7hr
NGC 5272 (M3)	−1.57	15.03	0.01	5'×5'	2.05hr
NGC 6093 (M80)	−1.66	14.96	0.18	5'×5'	2.05hr
NGC 6205 (M13)	−1.65	14.43	0.02	5'×5'	1.1hr
NGC 6341 (M92)	−2.24	14.78	0.02	5'×5'	1.1hr
NGC 6388	−0.60	15.30	0.44	5'×5'	2.05hr
NGC 6539	−0.66	14.62	1.08	5'×5'	1.1hr
NGC 6440	−0.34	14.48	1.15	5'×5'	1.1hr
NGC 6441	−0.53	15.26	0.52	5'×5'	2.05hr
NGC 6752	−1.54	13.18	0.04	5'×5'	0.9hr
NGC 7078 (M15)	−2.17	15.15	0.09	5'×5'	2.05hr
NGC 7099 (M30)	−2.13	14.71	0.03	5'×5'	1.1hr

total # of AORs: 17.
total observation time: 26 hrs.

Table 4.1: List of the selected targets and main parameters.

(a) Cluster metallicity, reddening and distance modulus from Ferraro et al. (2000) and Valenti et al. (2007).
(b) Total field of view covered by our IRAC mapping with all the 4 filters.
(c) Total exposure time for our IRAC mapping, according to the AOR duration estimated with SPOT–v11.07.

ground based wide field photometry in the outer regions have been also obtained by our group through a long term project devoted to study the HB morphology of GGCs.

According to SPOT-v11.07, the stellar point sources and IRAC sensitivity PET, a frame time of 12 sec and a *25-30 Cycling Positions* dithering pattern with the *Small* Scale Factor, repeated a few times for total on source integration times between 1000s and 2700s in each filter, depending on the cluster distance, allows us to reach the HB level at $M_{bol} \approx 0.0$ (i.e. $13 \leq K \leq 15$) with $S/N \approx 20$. Such a setup is optimized to maximize the spatial coverage and the "on source" integration time. The 4 brightest clusters in our sample, namely NGC 104, NGC 5139, NGC 6397 and NGC 6752 have been observed using the *High Dynamic Range* Readout Mode, to avoid saturation of the brightest tip giants, all the others using the normal *Full Array* Readout mode. NGC 5139, the sparsest cluster in our sample, have been mapped using a rectangular 1×4 grid in array coordinates, allowing the mapping of the central $14' \times 5'$ in all the four IRAC filters, while NGC 104 have been mapped using a 1×3 grid to cover the central $9' \times 5'$. All the other clusters have been observed with 2 pointings so that for the central $5' \times 5'$ we have exposures in all 4 IRAC bands. The adjacent fields can provide ML rates of stars in the more external regions of the clusters and suitable references for checking background emissivity. In order to observe our sample of 17 clusters with IRAC a total observing time of 26 hr was requested. The list of the selected targets and their main parameters is given in Table 4.1.

4.2 The observed sample

Here we briefly report some properties of the observed clusters.

NGC 6341 (M92). The GC M92 is one of the most metal poor GCs ([Fe/H]=-2.27, Harris (1996)) in the Galaxy and the most metal poor in our sample. It is relatively small but compact, with a mass estimated to be approximately $2.1 \times 10^5 M_\odot$ (Pryor & Meylan, 1993). Its location, far from the Galactic plane, minimizes the significance of field-star contamination.

NGC 7078 (M15). M15, with [Fe/H]=-2.4 (Sneden et al., 1997) is one of the most metal-poor GCs. It is a post-core-collapse cluster with

an extraordinarily dense center (Sosin & King, 1997), containing approximately 4000 $M_\odot$ (Phinney, 1996). It is a well-studied cluster, as it is home to the first planetary nebula (PN) discovered in a GC (K648, also designed as Ps 1; Pease, 1928; Howard et al., 1997; Alves et al., 2000) and to the first GC low-mass X-ray binary source (X2127+119; Auriere et al., 1984; Charles et al., 1986). At least eight millisecond pulsars are also associated with the cluster (Kulkarni & Anderson, 1996). Galactic coordinates for M15 are $l = 69°.01$ and $b = -27°.31$, placing the cluster $\sim$4.5 kpc south of the Galactic plane. Boyer et al. (2006) have presented Spitzer Space Telescope IRAC and MIPS observations of M15. Their analysis suggest the presence of intracluster medium (ICM) dust in the cluster core, with a mass of $(9 \pm 2) \times 10^{-4} M_\odot$ and an equilibrium temperature of $\approx$70 K. They also present Spitzer IRS observations of the planetary nebula K648.

NGC 7099 (M30). M30 is a relatively nearby cluster ($\sim$7 kpc, Peterson (1993)) at high Galactic latitude (b = 46.8), and is at the metal-poor end of the cluster [Fe/H] distribution ([Fe/H]=-2.13, Harris (1996)). M30 is a post-core-collapse cluster, with a high central density and a moderate total mass. The extraordinarily high central density of M30, which may exceed $\sim$$10^6$ $M_\odot$pc^{-3}, makes its core and the surrounding power-law cusp one of the highest density environment in the Galaxy. A high rate of stellar interactions is expected in the core and cusp regions, resulting in blue straggler formation via stellar mergers, binary formation via tidal capture and/or three body interactions, and binary interactions such as exchange encounters (Hut et al., 1992). M30 shows some of the strongest evidence of stellar interactions seen in any globular cluster. It has a very high blue straggler frequency, a very large bluer inward color gradient, and a large deficit of bright giants in the inner region (Guhathakurta et al., 1998; Howell et al., 2000). Thus, the central region of M30 is expected to be a conducive environment for the formation of X-ray binaries.

NGC 6093 (M80). M80 is a centrally concentrated, rather metal poor ([Fe/H]= -1.66) halo globular cluster. It is best known for the nova T Scorpii, which appeared in its center in 1860 and was observed visually for about a month. Ten variable stars have been found in or near the clusters, some of which have been followed since 1939 (Sawyer Hogg,

1973; Wehlau et al., 1990). It is one of the densest globular clusters in the MilkyWay, with a spectacular blue straggler sequence (Ferraro et al., 1999b), and 19 X-ray sources (Heinke et al., 2003).

NGC 6205 (M13). M13 is one of the brightest and best known of the globular clusters. Investigation on variable stars showed that M13 has an unusual distribution in the types of variables that it contains, with only a small fraction being the RR Lyrae type that are the most common in GC. The globular clusters M3 and M13 are a famous second-parameter GC pair that have nearly the same metallicity, but possess different horizontal-branch (HB) morphology. M13 has predominantly blue HB stars that extend below the main-sequence turnoff point. There are some gaps along the BHB star sequence, and the cluster has some RR Lyrae stars but no RHB stars

NGC 5272 (M3). The globular cluster M3 is one of the most studied in the Galaxy. M3 is particularly known for containing the largest number of RR lyrae variables, with more than 182 such stars (Clement et al., 2001). M3 and M13 are one of the most famous second-parameter pairs, along with NGC 288 and NGC 362. The difference in HB morphology between M3 and M13, however, is not as dramatic as that of NGC 288 and NGC 362 because M3, the cluster with the redder HB, has both red HB stars and blue HB stars including RR Lyrae stars that fill the instability region of the HB sequence

NGC 6752. NGC 6752 is one of the nearest clusters. Ferraro et al. (2003a) presented a new determination of the center of gravity and of the star density profile, suggesting that NGC 6752 is experiencing a post-core collapse bounce. NGC 6752 hosts five known millisecond pulsars (D'Amico et al., 2001). Using high-resolution images taken at the European Southern Observatory (ESO) Very Large Telescope (VLT), the optical companion of a binary millisecond pulsar have been identified as a helium white dwarf (Ferraro et al., 2003a,b; Cocozza et al., 2006). The CMD of NGC 6752 shows two interesting features: (i) shows an HB formed only by hot stars without RR Lyrae pulsators; (ii) shows a wide gap in the population of the HB. Interesting enough a second gap was suggested in the SGB togheter with a possible indication for other one

along the RGB (Cannon, 1981; Buonanno et al., 1986).

NGC 5139 (ω Cen). The stellar system ω Centauri is the most luminous and massive object among the GGCs, and it is surely the most peculiar one in terms of structure, kinematics, and stellar content. It is the most flattened GGC, displaying also a decrease of ellipticity in the most internal region (Geyer et al., 1983) and it has a significant rotation (Merritt et al., 1997). The most interesting anomaly is its chemical inhomogeneity (first revealed by Dickens & Woolley, 1967 and spectroscopically confirmed by Freeman & Rodgers, 1975): ω Centauri is the only known GGC which shows clear variations in the metal content of its giants. This evidence has been firmly established in the past by extensive low (Norris et al., 1996; Suntzeff & Kraft, 1996) and high resolution (Norris & Da Costa, 1995; Smith et al., 2000) spectroscopic surveys. More recently, the scenario has become more complicated due to discovery of an additional, metal-rich population with its own distinct RGB that contains approximately 5% of the red giants in ω Cen (Lee et al., 1999; Pancino et al., 2000, 2002). The metal-rich giants appear to have different spatial distribution and dynamical behavior with respect to the metal poor ones. Recent high-precision photometric analyses (Sollima et al., 2004, 2005a,b, 2006) have reveleated a discrete structure of its RGB, indicating a complex star formation history: in addition to the dominant metal-poor ([Fe/H] $\sim$ -1.6) and the extreme metal-rich population ([Fe/H] $\sim$ -0.6), three metal-intermediate component (spanning a range of metallicity -1.3 $<$ [Fe/H] $<$ -1.0) have been identified. Finally, new peculiarities along the main sequence of the cluster have been also discovered. Indeed, an additional blue MS running parallel to the dominant one has been resolved. According to stellar models with canonical chemical abundances, the location of the observed blue MS would suggest a very low metallicity ([Fe/H] $<$ -2) (Anderson, 2002; Bedin et al., 2004; Sollima et al., 2007). So, the spread in metallicity of the stars in ω Cen is an order of magnitude larger than those observed in GGCs. For this reason, ω Cen could not be a "genuine" globular cluster but more likely the remnant of a dwarf galaxy which merged in the past with the Milky Way.

NGC 288. The globular cluster NGC 288 has become the focus of much

debate in the last several years. Many photometric studies of the cluster have appeared in the literature. Metallicity estimates for the cluster by various authors uniformly fill the range $-1.7 \leq [\text{Fe/H}] \leq -1.0$. NGC 288 is important for the study of GC composition and CMD morphology, because its intermediate metallicity yet purely blue horizontal branch implies it should be classified as an "anomalous" cluster similar to M13. NGC 288 and NGC 362 are a second-parameter pair: they have similar metallicity and red giant branch but very different HB morphologies: while the HB of NGC 288 lies entirely to the blue of the RR Lyrae gap, that of NGC 362 lies predominantly to the red. Further, these clusters have similar distance moduli and reddening.

NGC 2808. The massive globular cluster NGC 2808 has been the subject of many photometric and spectroscopic studies (see Cacciari et al., 2004). It has a very complex HB. First, it is greatly extended: among GGCs, only ω Cen and M54 have HBs that go so far to the blue. Second, the distribution of stars along the HB is multimodal, with at least three significant gaps (Sosin et al., 1997), one of these gaps being at the color of the RR Lyrae instability strip. In fact, even though the HB is well populated both to the blue and to the red of the instability strip, very few RR Lyrae stars have been identified in NGC 2808. The other two gaps are on the blue extension of the HB. As such, NGC 2808 is one of the more obnoxious examples of the second-parameter problem, in which HB star distributions cannot be explained in terms of metallicity alone. D'Antona et al. (2005) had suggested that the MS of this cluster has an anomalous blueward extension that involves $\sim 20\%$ of the stars, and Piotto et al. (2007) have demonstrated that the blueward extension is indeed real and that, surprisingly, it is due to the presence of at least three distinct main sequences. The three MS branches may be associated with the complexities of the cluster's horizontal branch and of its abundance distribution.

NGC 362. NGC 362 is situated towards the northern projection of the Small Magellanic Cloud. The main feature of its CMD is the richness of red horizontal branch stars, in contrast to the lack of blue stars, as in metal rich globular clusters, while metal intermediate GC are characterized by the fact that both sides of the variable star gap are populated in a similar

way. NGC 362 is the red member of a famous second-parameter pair of clusters (along with NGC 288).

NGC 1851. The Galactic globular cluster NGC 1851 is rich, centrally condensed, and belongs to the small group of clusters that display bimodal HB morphology, showing both a red clump and an extended blue tail. The cluster is at high galactic latitude so that field star contamination and reddening are low. It contain an X-ray burst source. Finally, there are some RR Lyrae variable known, and 13 blue straggler stars have been identified (Walker, 1992; Saviane et al., 1998).

NGC 104 (47 Tuc). 47 Tuc is one of the most close and massive globular cluster in the halo system. It is the second brightest globular cluster in the sky (after Omega Centauri), and is noted for having a very bright and dense core. It has more than 20 known millisecond pulsars, and a very high population of blue stragglers near the core. Some long period variable have been observed and only one RR Lyrae star. It is the prototype of metal-rich ([Fe/H]=0.71; Harris 1996) red HB cluster. Detailed studies of the near-infrared properties of the red giant and HB of this cluster have been presented by Montegriffo et al. (1995), Ferraro et al. (2000) and Valenti et al. (2004a,b).

NGC 6440. The globular cluster NGC 6440 is located at equatorial coordinates $(\alpha, \delta)_{J2000.0} = (17^h48^m52.7^s, -20°21'37'')$. It is moderately concentrated but apparently has no post collapse core. Photometric studies suggested that NGC 6440 was among the most metal–rich globular cluster in the Galaxy, with metallicity [Fe/H]=-0.49, distance modulus $(m–M)_0$=14.58 and reddening E(B–V)=1.15 (Valenti et al., 2004a,b).

NGC 6388. NGC 6388 is a moderately reddened (E(B–V)=0.44), metal–rich ([Fe/H]=-0.61) GGC (Valenti et al., 2007) located in the outer Bulge region, at equatorial coordinates $(\alpha, \delta)_{J2000.0} = (17^h36^m17.0^s, -44°44'06'')$. Valenti et al. (2007) estimate a distance modulus of $(m–M)_0$=15.38. Since the discovery by Rich et al. (1997) of an extend blue HB (as well as in NGC 6441) in its HST-based CMD, NGC 6388 has been subject of several optical photometric studies (Piotto et al., 2002; Pritzl et al., 2002; Catelan et al., 2006). NGC 6388 displays

a quite peculiar HB morphology. In fact, besides a well populated red HB clump (a feature normally predicted by the stellar evolution theory in the case of old, metal–rich populations) it shows an extend blue tail and a population of RR Lyrae variables (Pritzl et al., 2002).

NGC 6441. NGC 6441 is a massive, metal–rich ([Fe/H]=–0.68; Valenti et al. (2004a,b)) globular cluster, located at equatorial coordinates $(\alpha, \delta)_{J2000.0} = (17^h50^m12.9^s, -37°03'05'')$. As well as its twin NGC 6388, NGC 6441 shows very unusual HB extending from stubby red, as expected for his high metallicity, to extremely blue, and with the red HB sloping upward as one moves blueward in the V, B–V color-magnitude diagram (Rich et al., 1997; Pritzl et al., 2001, 2002, 2003). Rather unexpectedly, large numbers of RR Lyrae stars with unusually long periods have been discovered in this cluster (Pritzl et al., 2001, 2002, 2003; Clementini et al., 2005). NGC 6388 and NGC 6441 are thus the most metal–rich examples of second-parameter affecting the HB morphology.

NGC 6539. NGC 6539 is a poorly studied cluster located in the outer Bulge. According to the compilation of Harris (1996), NGC 6539 is located at equatorial coordinates $(\alpha, \delta)_{J2000.0} = (18^h04^m49.8^s, -0.7°35'09'')$. A large dark cloud complex in the foreground is responsible for its high reddening (E(B–V)=1.08; Sandell, Stevens & Heiles, 1987). Based on an apparent distance modulus of 17.63 mag, Harris (1996) calculates that the cluster lies at a heliocentric distance of 8.4 Kpc, about 3.1 Kpc from the Galactic center. The metallicity is estimated to be [Fe/H]=-0.66 (Zinn, 1985), although more recent estimated include -0.79 and -0.76 (Stephens & Frogel, 2004; Origlia et al., 2005). The best estimates of the cluster's structural parameters include a core radius $R_{core} = 0.54'$, a half-mass radius of $R_{hm} = 1.67'$, and a tidal radius of $R_{tidal} = 21.5'$ (Harris, 1996). Baker et al. (2007) have discovered 12 long-period variables in the cluster.

4.3 Photometry of stars in GCs

To measure brightnesses of point sources in CCD images, there are basically two methods: aperture photometry and PSF fitting. In aperture photometry, one defines one aperture (usually circular) enclosing the source, and another (usually a ring outside the first) that contains only sky. One obtains the mean

counts per pixel from the sky aperture, subtracts that mean from each pixel in the source aperture, and sums the remaining counts to find the total in the stellar image. This method is the best, but unfortunately it is reserved to uncrowded fields.

For crowded fields (GCs, in particular), it is necessary to switch to the procedure of profile fitting: a model of the stellar images is fitted to the data via a least-squares algorithm[1]. Many stars can be handled at the same time. The integration of the individual two-dimensional profiles yields the contribution of each stars. The profile fitting, or point-spread function (PSF) fitting, constitute a complex procedure, essentially involving image processing application. A wide variety of image processing packages exist.

The software package used to processing IRAC images is ROMAFOT (Buonanno et al., 1983). Hereafter we list the main features of this photometric image processing algorithm:

- **Establish the PSF.** The PSF can be modeled by a number of mathematical functions, the most common include Gaussian and Moffat. We have used the Moffat:

$$f(x) = \frac{I_0}{(1 + (\frac{x}{\sigma})^2)^\beta}$$

  where σ and β are fitting parameters. A table of residuals can be summed to the analytic function, to better reproduce light distribution.

- **Sky level evaluation.** The value of the sky background cannot be considered as a constant, and, particularly in the case of Globular Cluster photometry, it is extremely critical: different frequency variations, due to the bulge of the cluster and to the presence of crowded regions are present. In this case, a local (in the immediate vicinity of a star) sky background must be evaluated.

- **Object identification.** To detect the images it is used a fast sequential algorithm which examines all the elements of the pictures and associates a stellar object to each pixel detected above a threshold value. The

---

[1]The method of least squares is used to approximately solve over-determined systems, i.e. systems of equations in which there are more equations than unknowns. Least squares can be interpreted as a method of fitting data. The best fit, between modeled and observed data, in the least-squares sense is that instance of the model for which the sum of squared residuals has its least value, a residual being the difference between an observed value and the value given by the model.

threshold value is generally adopted at $3 - -5\sigma$ the noise of local background.

- **PSF-fitting.** The algorithm centers and scales the PSF on the actual profile.

- **Final catalogue.** Stars magnitude are derived as:

$$m_i = -2.5 \ \log \ (\ V_i \ )$$

where V_i is the integral of the PSF function of each component. In the case of a Moffat function the used relation is:

$$m_i = -2.5 \ \log \ \left(\frac{I_{0i} \ \sigma^2 \ \pi}{\beta - 1} \right)$$

Stellar magnitude and position of each component are finally recorded in a catalogue.

4.4 Photometric and Astrometric Calibration

Any photometric system is defined in terms of a system of magnitudes of selected "standard" stars. Each photometric instrument has its own natural (or instrumental) system. In order to compare photometric observation with fluxes predicted by a theoretical model or with data containing in literature, one must "calibrate" instrumental magnitudes to a "standard" photometric system. In Section 3.4.3 we have reported the zero-magnitude fluxes for each IRAC channel. We have calibrated the instrumental magnitudes using this relation:

$$m^{[i]} = m^{[i]}_{romafot} - 2.5 \ \log \ (\ C^{[i]} \ ) + 2.5 \ \log \ (\ F^{[i]}_{zero} \ ) - 2.5 \ \log \ (\ \omega^2_{pix} \ ),$$

where $m^{[i]}_{romafot}$ is the output of the software, $i = 3.6, 4.5, 5.8$, and 8 are the four IRAC channels, C is the absolute calibration factor (see Section 3.4.2), $F^{[i]}_{zero}$ is the zero-magnitude flux (see Section 3.4.3) and ω_{pix} is the solid angle. These are the obtained calibration factor:

$$m^{[3.6]} \ = \ m^{[3.6]}_{romafot} \ + \ 19.658$$

$$m^{[4.5]} \ = \ m^{[4.5]}_{romafot} \ + \ 18.911$$

$$m^{[5.8]} \ = \ m^{[5.8]}_{romafot} \ + \ 16.846$$

$$m^{[8.0]} \; = \; m^{[8.0]}_{romafot} \; + \; 17.405$$

All the catalogs have been "astrometrized" by determining the precise positions of each star in an absolute reference system, in terms of right ascension α and declination δ. To do this we used *CataXcorr*, a software developed at the Bologna Observatory (P. Montegriffo, private communication). This software aligns a catalog to a reference catalog: using triangulations, the software find the common stars, then using a polynomial function (usually a degree one polynomial function) convert the local position to the absolute reference system. So, the *Spitzer* catalogs have been combined and placed onto the 2MASS astrometric system by cross-correlating the *Spitzer* and the ground-based near-IR surveys.

4.5   Near-IR Photometry

Complementary high resolution ground based near-IR photometry of the central region of the observed cluster has been obtained using IRAC2@ESO2.2m, SOFI@ESO-NTT and NICS@TNG, and supplemented with 2MASS data in the external region. The photometric reduction of the near-IR images was carried out using ROMAFOT (Buonanno et al., 1983) and DAOPHOTII/ALLSTAR (Stetson , 1994).

The fact that the IRAC@Spitzer catalogues are combined with near IR stellar photometric catalogues, suitably cleaned by spurious detections and unlikely cluster members, has also the advantage of excluding any contamination by background sources.

The IR magnitudes have been corrected for extinction, according to the E(B–V) values reported in Table 4.1 and the Rieke & Lebofsky (1985) and Indebetouw et al. (2005) interstellar extinction law.

Suitable transformations between near IR colors and bolometric corrections and effective temperatures have been computed by using the Kurucz's model spectra convoluted with the 2MASS broad band filters, following the procedure described in Origlia et al. (2007). Very similar transformations have been obtained by Montegriffo et al. (1998). These relations have been used to derive the bolometric magnitude and temperature of each star detected in our IRAC@Spitzer survey, from its dereddened $(J-K)_0$ color and M_K absolute magnitude, as computed using the distance moduli by Ferraro et al. (2000) and Valenti et al. (2007) and listed in Table 4.1.

Chapter 5

Color-magnitude and color-color diagrams

For each observed cluster, the J, H, K, 3.6, 4.5, 5.8, 8.0 photometric catalog of the giant (RGB and AGB) stars have been used to construct suitable color-magnitude (CMDs) and color-color (CCDs) diagrams and select candidates with circumstellar dust excess.

In order to compare results from different stellar clusters, it is very convenient to work in the absolute planes. We thus use the absolute K band magnitude and the $(J-K)_0$ and $(K-IRAC)_0$ IR colors of the measured stars in each cluster to construct diagnostic CMDs.

Figure 5.1 shows the M_K, $(J-K)_0$ and M_K, (K-IRAC) CMDs of 47 Tuc. The results for this cluster have been already published in Origlia et al. (2007).

Figures 5.2, 5.3 and 5.4 show the M_K, $(K-8)_0$ CMDs of the other 15 observed clusters. We order the clusters from the most metal poor to the most metal rich. For each clusters we have also reported the HB level (dashed line). ω Cen has not been analyzed in this thesis because the strategy to select stars with color excess on its multiple RGBs is quite complex and requires additional effort to accomplish it.

The $(K - IRAC)_0$ colors of stars with pure photospheric emission are $\approx 0.0 \pm 0.1$ along the entire RGB range sampled by our survey. This is in good agreement with the prediction of theoretical model atmospheres with $T_{\mathrm{eff}} = 3500$–5000 K from the Kurucz database.

In order to select candidates with color (hence dust) excess, mean ridge lines in each CMD have been computed from the average colors of the stars with purely photospheric emission and the overall photometric errors (σ) in different magnitude bins have been determined. Then, since the 8 μm IRAC band is
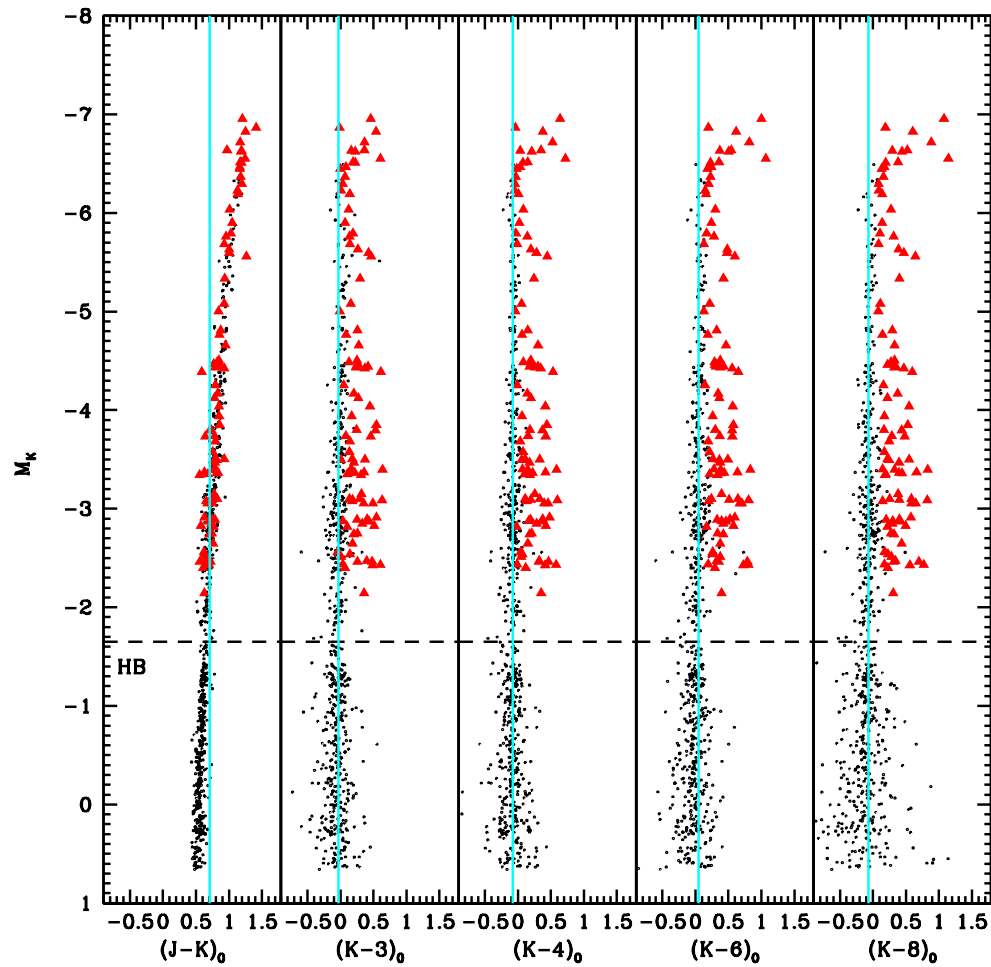
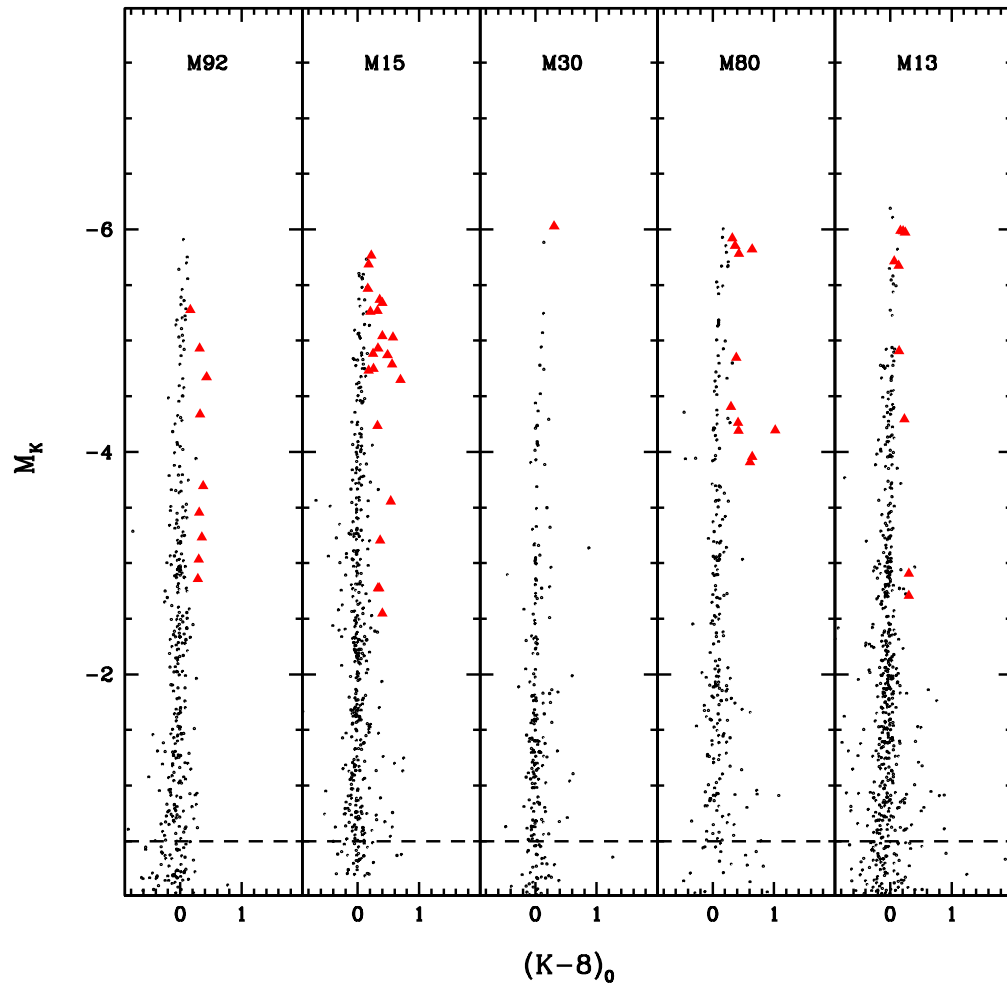Figure 5.1: M_K, $(J-K)_0$ and M_K, $(K-IRAC)_0$ CMDs of 47 Tuc. Stars with color excess are marked in red.

Figure 5.2: Mk, $(K-8)_0$ CMDs of some clusters in our sample. Stars with color excess are marked in red. The HB level is also reported (dashed line).
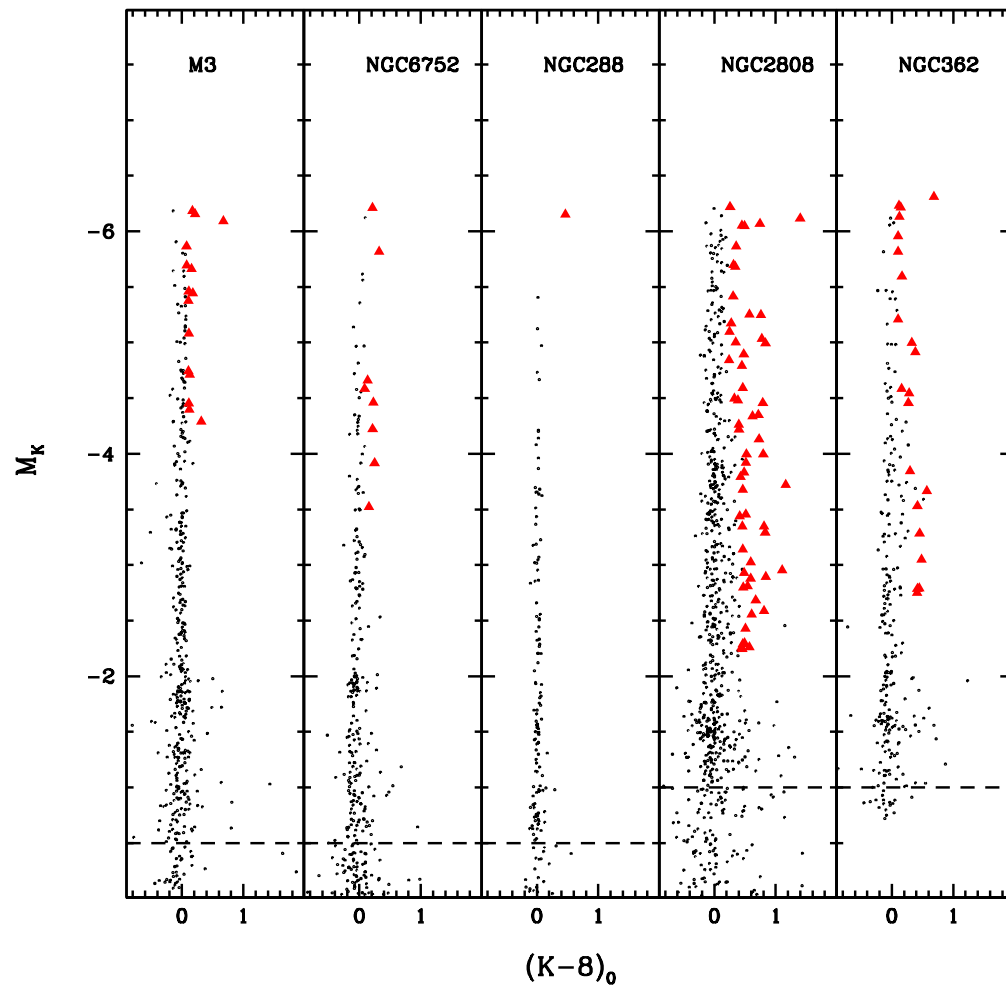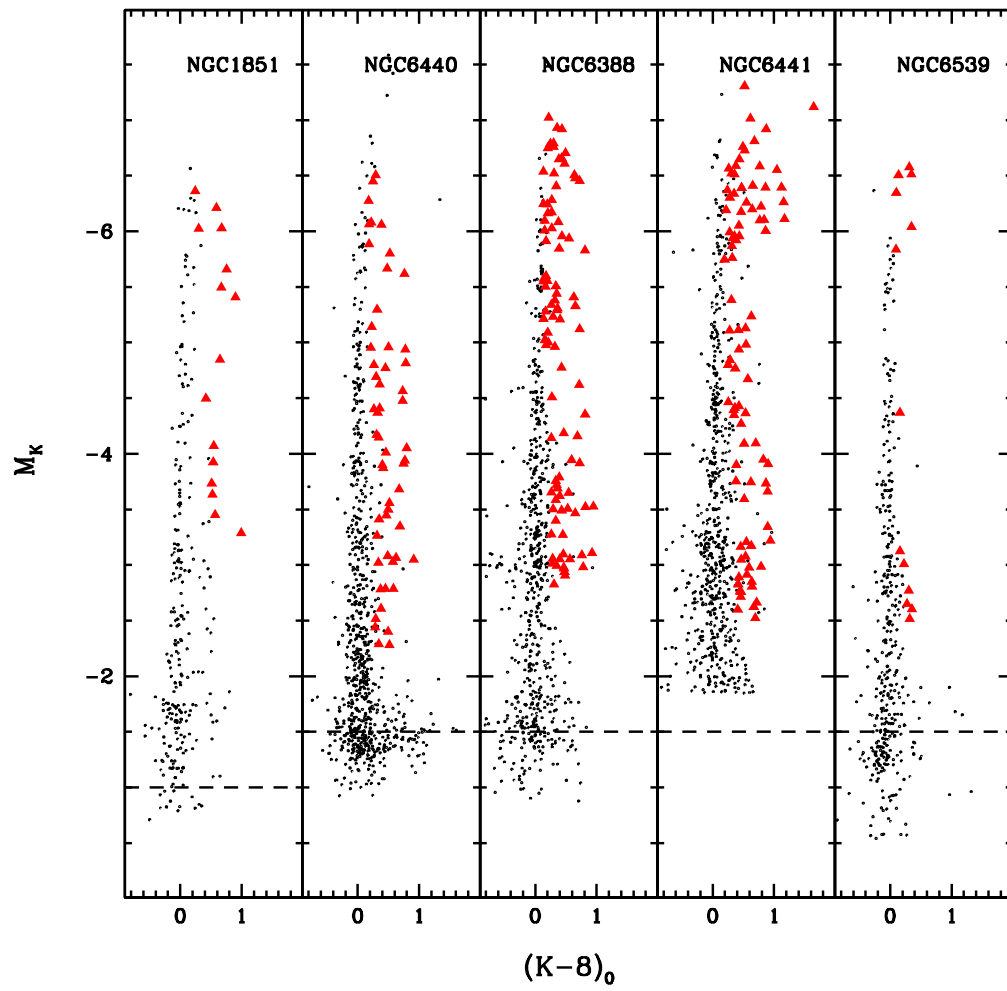
Figure 5.3: As Figure 5.2.

Figure 5.4: As Figure 5.2.

the most sensitive to warm dust and the least contaminated by photospheric emission, stars are flagged as dusty if they show a $(K - 8)_0$ color excess with respect to mean ridge line $\geq n\sigma$. However, we mention that these stars are also normally the reddest in the other IRAC bands (see e.g. Figure 5.1). Stars with a 3σ excess in the $(K - 8)$ color are marked as filled triangles in the plotted CMDs.

Table 5.1 summarizes the results on star counts from our photometric IRAC@Spitzer survey. We detected and measured about 8000 giants above the HB level, and almost 600 show color excess.

In the closest clusters like 47 Tuc where it has been possible to measure stars down to the base of the RGB, we have checked whether some stars below the HB level show 3σ color excess, and we did not find any evidence for that.

By inspecting the observed CMDs (see Figures 5.1, 5.2, 5.3, 5.4) one can clearly see that only a fraction of giant stars show color excess. In order to properly estimate such a fractional number along the RGB, one need to correct star counts by the following contributions/effects:

- incompleteness

- field contamination

- AGBs and LPVs

5.0.1   Completeness and field contamination

The degree of completeness of the near-IR photometric catalogues is always $\approx 100\%$ over the full magnitude range covered by our Spitzer survey, as inferred by artificial star experiments as well as by a comparison with high resolution HST photometry. The completeness of the IRAC@Spitzer photometric catalogues is normally >90% down to M_K=-2 and >70% at fainter magnitudes, with the exception of the very central $10''$–$20''$ of the most concentrated clusters (i.e. 47 Tuc, NGC 6440, NGC 6441, NGC 6388, M80) where it drops down to $\leq 60\%$. In the computation of the star counts, completeness is taken into account, being the innermost crowded region of the most concentrated clusters excluded.

In order to estimate the degree of possible field contamination, we use 2MASS and select an annular region at 20'<r<22' around each cluster and count the stars per magnitude bin. Field contamination is negligible in most

Cluster	mid-IR[a]	near-IR[b]	AGB	LPV[n]	dusty stars
NGC 104 (47 Tuc)	747	1011	95^c	29^o	93
NGC 288	156	200	-	-	3
NGC 362	282	438	33^d	2	26
NGC 1851	277	388	28^e	1	15
NGC 2808	771	1566	61^f	-	34
NGC 5272 (M3)	472	872	24^g	1	20
NGC 6093 (M80)	270	662	34^h	-	14
NGC 6205 (M13)	679	1002	20^g	1	28
NGC 6341 (M92)	404	705	28^i	-	9
NGC 6388	764	2047	53^l	8	108
NGC 6539	395	613	-	-	32
NGC 6440	873	1392	47^d	-	76
NGC 6441	720	1127	23^m	11	93
NGC 6752	572	907	-	-	10
NGC 7078 (M15)	471	669	22^i	-	15
NGC 7099 (M30)	260	387	-	-	5

Table 5.1: Star counts from the photometric IRAC@Spitzer survey.

(a) Mid-IR survey: number giant stars above the HB with IRAC@Spitzer photometry.

(b) Near-IR survey: number of giant stars above the HB in the field of view covered by our Spitzer survey.

(c) From Beccari et al. (2006).

(d) From Piotto et al. (2002), supplemented with WFI photometry in the external region.

(e) From Lanzoni, private communication, supplemented with WFI photometry in the external region.

(f) From Dalessandro et al. (2010, in preparation).

(g) From Ferraro et al. (1997).

(h) From Ferraro et al. (1999b), supplemented with WFI photometry in the external region.

(i) From Beccari, private communication.

(l) From Dalessandro et al. (2008).

(m) From Valenti, private communication.

(n) From Clement et al. (2001).

(o) From Lebzelter et al. (2006).

clusters but in NGC 6440, NGC 6441 and NGC 6388 where along the sampled RGB it turns out to be ≈20%, ≈30% and ≈5%, respectively.

5.0.2   AGB and LPV stars

To explore ML in first ascent red giants (RGB), it is important to decontaminate our catalogs from second ascent red giants (AGB). In fact AGB stars are located about in the same region of RGB stars in the K, J-K plane. In order to identify the AGB stars, we use complementary high resolution HST photometry, where available, and ground-based WFI photometry in the optical bands. The photometric reduction of the images was carried out using DAOPHOTII/ALLSTAR (Stetson , 1994). The AGB stars have been selected using suitable CMDs in the V, (U-V), V, (B-V) and V, (V-I) planes.

We also use the Clement et al. (2001) compilation to identify and decontaminate our catalogs from long period variable stars[1] as well.

5.0.3   Blend and Artifacts

Since the IRAC@Spitzer pixel is relatively large, it is possible that more than one star actually falls in it. Hence crowding is an obvious worry near cluster centers. A rather special kind of crowding can mimic a dusty star. If more than one star blends together in the 8μm PSF, and the blending object does not fall in the K or 3.6μm PSF a bogus IR excess can result. However, to produce an appreciable excess the blending star(s) must be comparable in brightness (say within a factor of 10) to the first star. In all the surveyed clusters, blending turned out to be a rare event, as expected.

In Boyer et al. (2010) and earlier papers (Boyer et al., 2008, 2009) on different clusters, the authors have suggested the possibility of blending and argued that the bulk of the dusty stars in Origlia et al. (2007) are blends. We stress that their statement is not based on a direct inspection of the stars in our sample, but simply on the appearance of their CMDs in a different photometric plane, in different sampled regions or even in different clusters. To estimate the possible magnitude of the blending problem, Boyer et al. (2010) employ a de-convolution technique in which the 3.6μm images are analyzed using the 8μm PSF. While this technique might give some estimate of the magnitude of blending problems, it is definitely less effective than a direct inspection

---

[1] A class of pulsating variable stars known as **long period variables** (LPVs) are AGB stars. LPVs have pulsation periods of 100 to 700 days and include the subclass of **Mira variable stars**.

of high spatial resolution optical/near IR images as done in Origlia et al. (2007). Boyer et al. (2010), relying on Spitzer data alone, may be also bothered by instrumental artifacts. We have no such problem since our high spatial resolution optical and near IR data have no (or at least different) artifacts.

A suitable cross correlation with high spatial resolution near infrared stellar catalogs allows for 1) a proper identification of the stellar counterpart, 2) the correct determination of the star photospheric parameters, and 3) a direct way to check for and remove possible blends, artifacts, background galaxies etc. It is also worth noting that we used ROMAFOT (Buonanno et al., 1983), a software package optimized to perform PSF fitting photometry of crowded fields even in a regime of under-sampling, as IRAC@Spitzer at the shortest wavelengths. ROMAFOT allows one to directly inspect the fit of faint and/or problematic sources to double check possible residual blending, artifacts, background galaxies etc. and to remove them. Objects identified as blends have been rejected as dusty giants.

As an additional, clear-cut test, Figure 5.5 shows 78 out of 93 candidate dusty giants in 47 Tuc as imaged by ACS@HST in the I band. For the majority (72 out of 78) of stars, only the target and a few (if any) much fainter stars (hence ineffective to produce a detectable excess) are present within the IRAC@Spitzer PSF area. The remaining 6 candidate stars with color excess, are actually a blend of 2-3 stars with similar luminosity both in the near IR and Spitzer PSFs. In this case we cannot precisely identify the star(s) responsible for the color excess but at least one has it.

Another indication that blending is not a problem is the absence of any correlation between the occurrence of blending and luminosity in the sampled RGB portion. If the dusty stars are real they should be distributed like the cluster light. False dusty stars arising from crowding should be preferentially found in regions of high density. Hence, as an additional test, by using a King model of 47 Tuc, one can find that about 64% and 36% of the total bolometric light sampled in the central 2 arcmin (in radius) is contained in the central 1 arcmin and in the annulus between 1 and 2 arcmin, respectively. The corresponding fractional number of dusty giants in the same regions are 67±11% and 33±7%. The observed numbers are completely consistent with model expectations and this should be the case only if crowding is not a problem. Hence, Boyer et al. (2010) conclusion that Origlia et al. (2007)
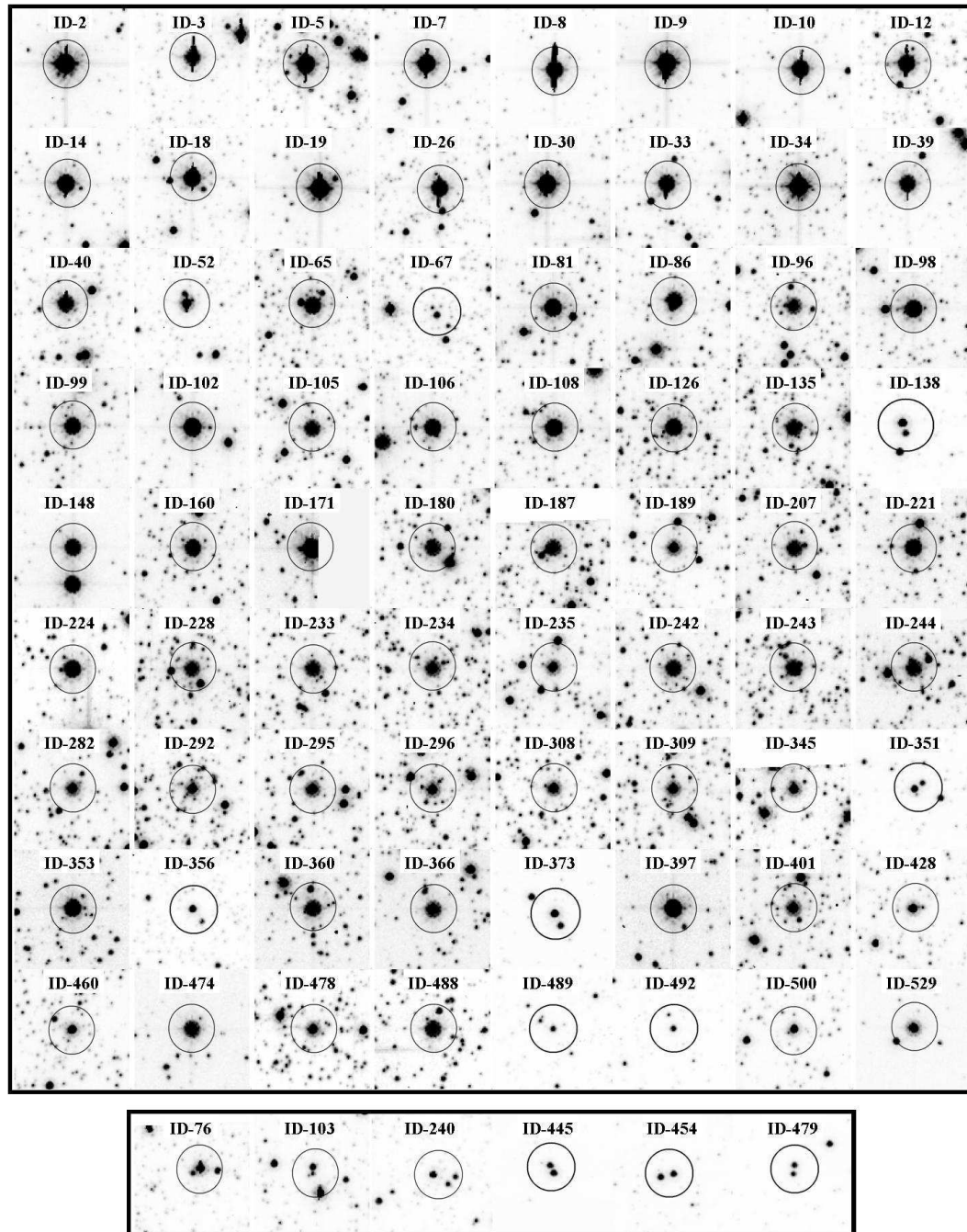
Figure 5.5: 78 candidate dusty giants in 47Tuc as imaged by ACS@HST in the I band. Circles mark the PSF area of Spitzer.

candidate dusty RGB stars below the tip are false detections is not justified.

5.1 Diagnostic Planes

In this section we provide direct evidence that the M_{bol}, $(K-8)$ plane used in Origlia et al. (2007) is the most effective in detecting dusty giants.

Figure 5.6 shows few representative color-color diagrams, combining near IR and Spitzer photometry. Black dots represent stars with no clear excess, colored points those stars showing a 3σ excess in the (K-8) color. Figure 5.7 shows the $(K-8)$, $(3.6-8)$ color-color diagram of 47 Tuc. The filled circles in the bottom panel marks those stars showing a 3σ excess in the $(K-8)$ color, while filled circles in the bottom panel marks those with also a 3σ excess in the $(3.6-8)$ color. The figures all show that the $(K-8)$ color is far more effective than the $(3.6-8)$ color in disentangling relatively warm ($T_{\mathrm{eff}} > 4000$ K) photospheres from optically thin, warm ($T_{\mathrm{dust}} > 500$ K) dusty envelopes. Most of the candidate dusty stars identified by Origlia et al. (2007) have $(3.6-8)$ colors in the 0.1–0.3 mag range, barely (if at all) exceeding the 3σ photometric uncertainty which ranges from 0.15 at $M_{\mathrm{bol}} < -2$ to 0.25 at $M_{\mathrm{bol}} \approx 0$. The $(K-8)$ color always exceeds 0.2 mag and spans a larger range. The reason for such a poor effectiveness of the $(3-8)$ color in disentangling stars with dust excess from those with pure photosperic emission, is that in relatively warm and low luminosity giants, like low mass RGB stars, the fractional contribution of the warm dust emission to the 3.6μm is *not* negligible and *not* much smaller than the dust contribution at 8μm. Indeed, for example, in the measured giants of 47 Tuc we estimate that the average dust contributions are 20% at 3.6μm and 30% at 8μm. The fractional contribution of dust emission at 3.6μm is negligible only in much cooler and more luminous giants stars and/or in case of envelopes with a large amount of dust. This is much clearer in Figure 5.8 that shows the estimated dust mass for the stars of 47 Tuc as a function of bolometric magnitude: empty circles marks those stars showing a 3σ excess in the $(K-8)$ color, filled circles show those with also a 3σ excess in the $(3.6-8)$ color. Hence, when using the $(3.6-8)$ color to select candidate dusty RGB stars in globular clusters, as done by Boyer et al. (2010), one is clearly biased towards the coolest (hence the most luminous) ones and with relatively large amount of circumstellar dust.
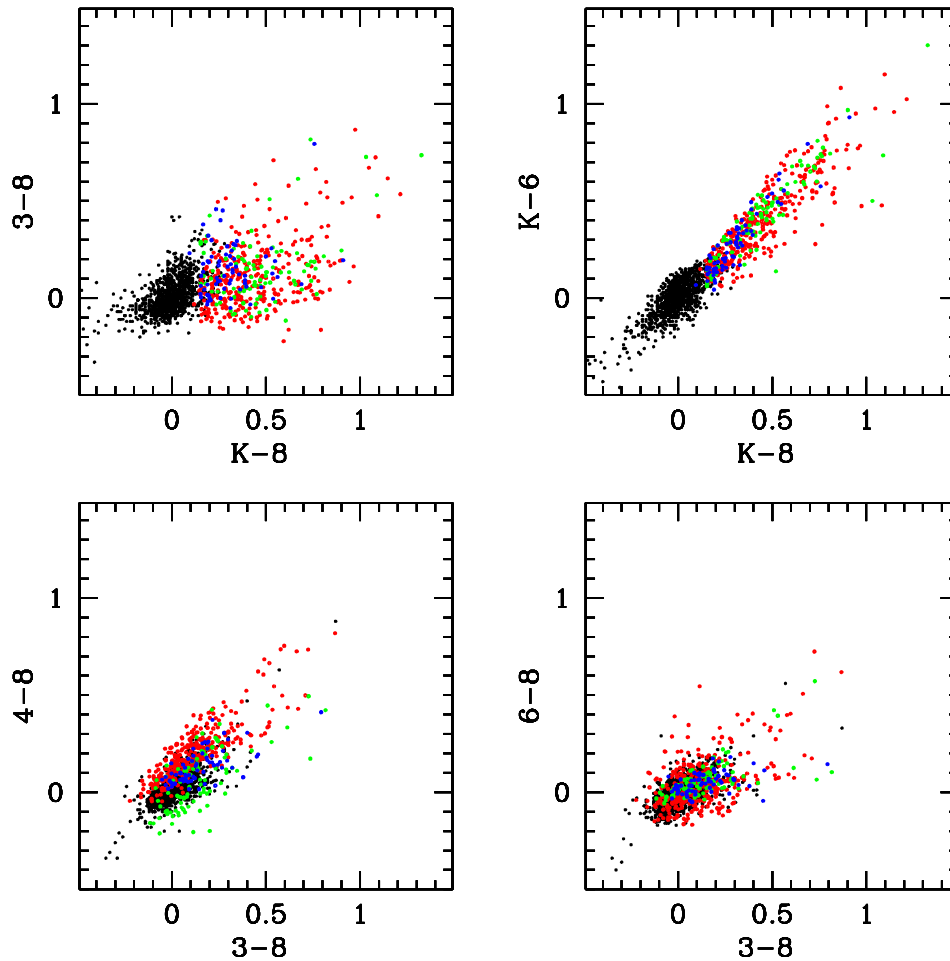
Figure 5.6: Few representative color-color diagrams, combining near IR and Spitzer photometry. Black dots represent stars with no clear excess. colored points those with excess, as inferred from the CMD shown before. As you can see in the bottom panels, whatever combination of pure Spitzer colors is chosen, it is almost impossible to distinguish between the two samples. The reason is that the bluer Spitzer filters like the 3.6 and 4.8 are contaminated by dust emission, hence they cannot be used to trace the pure photospheric contribution. A more sensitive separation between dusty and non dusty stars can be obtained using a combination of K and Spitzer photometry as shown in the top panels.
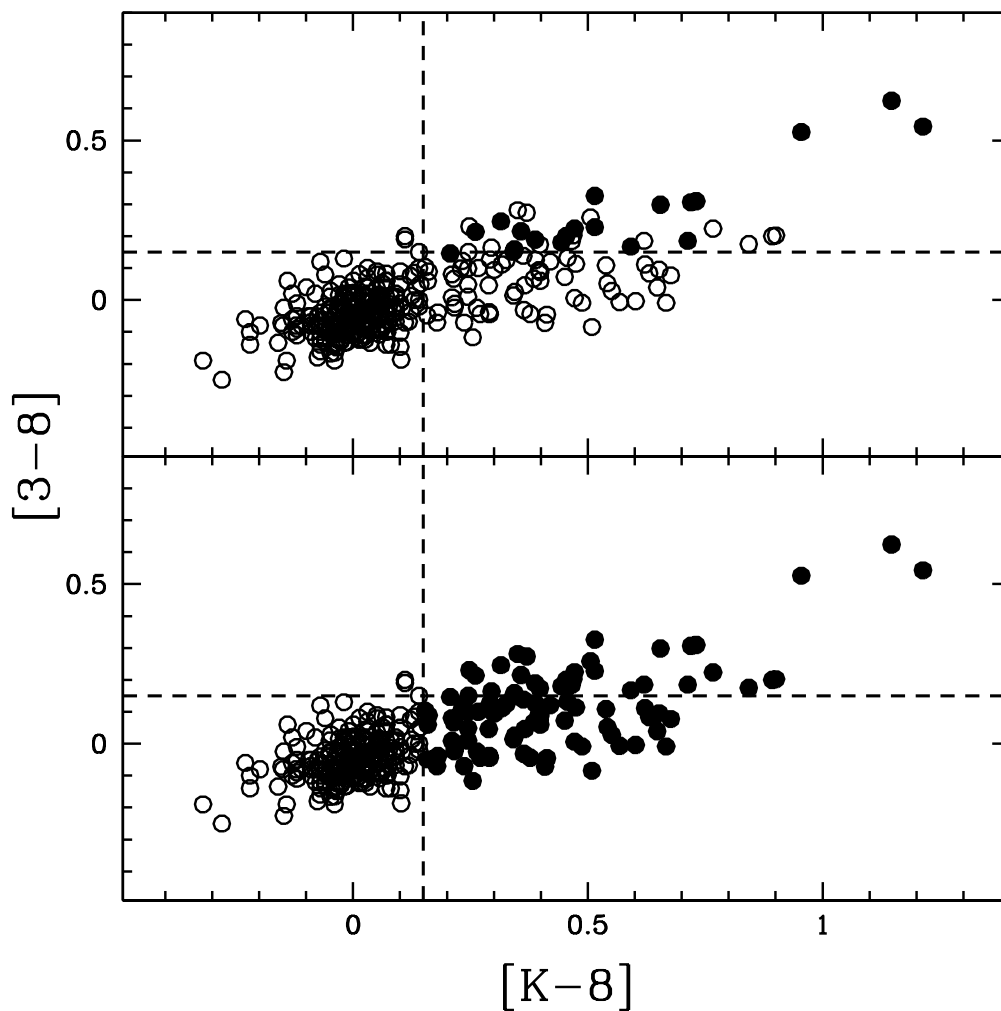
Figure 5.7: 3-8 versus K-8 color color diagram of 47 Tuc. In the bottom panel, filled circles are the dusty stars selected from the K-8 color excess, while in the top panel filled circles are the dusty stars with also 3-8 color excess. The 3-8 is less sensitive in disentangling cool photospheres from warm dusty envelopes: only those envelopes with a relatively large content of dust can be distinguished.
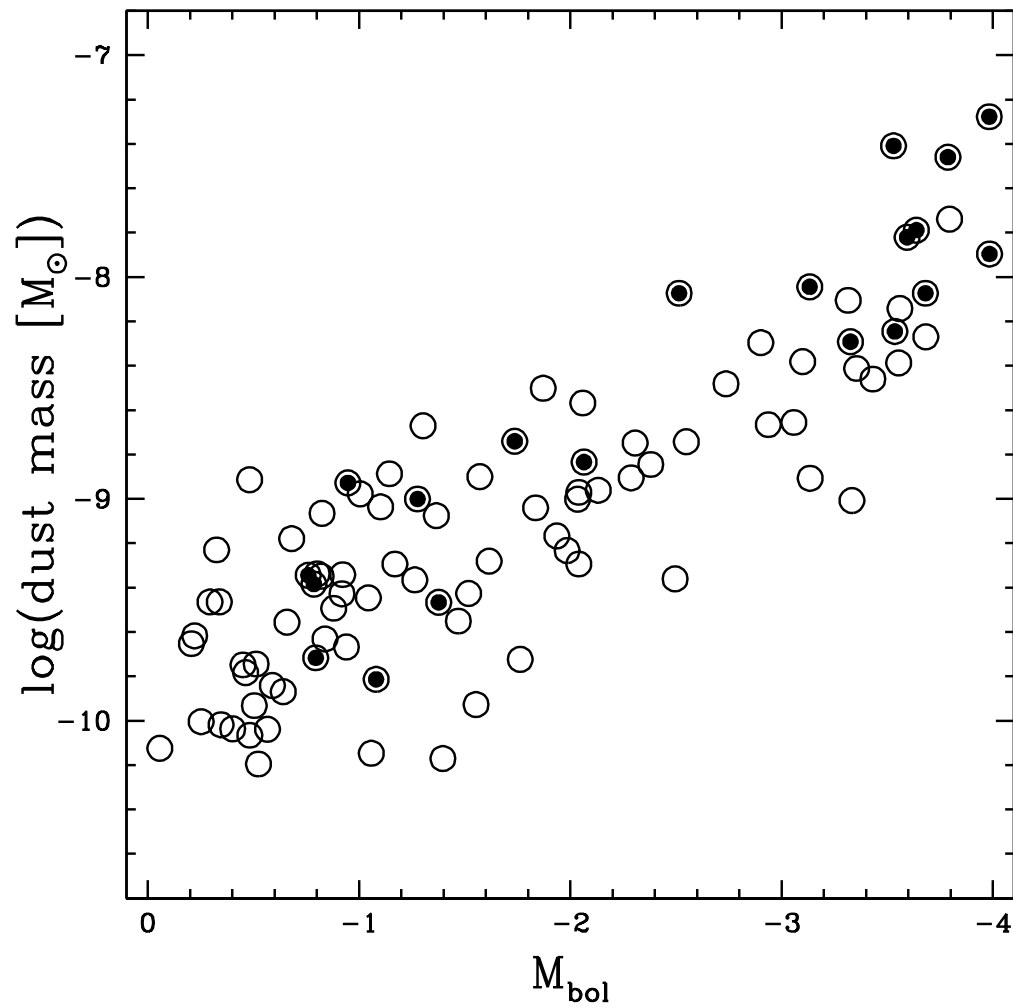
Figure 5.8: Estimated dust mass for the stars of 47 Tuc with color excess: stars with K-8 color excess are marked with empty circles, and stars with 3-8 color excess with filled circles.

5.2 Mass-losing stars: previous identification

5.2.1 SPITZER comparison

In Section 3.5 we have mentioned some previous studies of ML in GC using Spitzer. Here, we compare our results with those studies.

NGC 7078 (=M15)

Boyer et al. (2006) found 23 dusty IR sources. 20 sources are also present in our final catalog, while one (identified as IR4 by Boyer et al. (2006)) is out from our field of view, and 2 (identified as IR3a and IR3b by Boyer et al. (2006)) are too faint (both have k>15). We also detect the Planetary Nebula K648. We confirm as dusty star only one of their dusty sources. However they suggest that these dusty red giants are AGB and post-AGB stars and we have also classified the majority of them as AGBs.

NGC 362

Boyer et al. (2009) find 10 candidate mass-losing stars: they classify s02, s05, s06, s07, s08 as strong mass loss candidates because are very bright and have strong excess, s01, s02, s04, s09, s10 as moderate mass loss candidates (s01 is not a cluster member), s03 and s09 post-AGB stars. We also classified s01 (#4), s05 (#11), s06 (#1), s07 (#2) as dusty stars. s02 and s10 are out of our field of view. s05 and s08 are seen as one component by Spitzer, while from near IR images it is possible to distinguish two (also detected by McDonald & van Loon (2007)) and three components, respectively.

NGC 104 (=47 Tuc)

A star-to-star comparison with Boyer et al. (2010) and Ita et al. (2007) using AKARI is not possible, since the few stars near the tip with dust excess have not been properly catalogued. However, AKARI has neither the spatial resolution nor sensitivity to properly investigate the stellar population in central regions of globular clusters. We ourselves using ISOCAM found circumstellar dust excess only near the RGB tip (Origlia et al., 2002), again because of the lower spatial resolution and sensitivity of ISOCAM compared to IRAC.

5.2.2 ISO comparison

As we have seen in Section 2.3.3 NGC 104 (=47 Tuc), NGC 362, NGC 5139 (=ω Cen), NGC 6388, and NGC 7078 (=M15) have been also observed with ISOCAM (Origlia et al., 2002).

NGC 104 (=47 Tuc)

The seven 47 Tuc stars which showed dust excess in our ISOCAM survey have been also detected by Spitzer and confirmed as dusty stars.

NGC 362

Three sources in NGC 362 were identified as having IR excess in our ISOCAM survey. The spectra of these sources have been also obtained by McDonald & van Loon (2007) with VLT/UVES. They designated these source as x01, x02 and x03. x01 turns out to be a blend of Spitzer sources #5, #6 and #11, the latter with excess. X02 is located in the very central region and is definitely a complex blend of 5 sources. X03 is Spitzer source #3 with excess.

NGC 6388

Six sources in NGC 6388 were identified as having IR excess in our ISOCAM survey. All these source have been also detected by Spitzer and confirmed as dusty stars. ISO source 2 is a blend of Spitzer source #39 and #65, the latter with excess. ISO source 4 is a blend of Spitzer source #55 and #92, the latter with excess.

NGC 7078 (=M15)

Two sources in M15 were identified as having IR excess in ISOCAM survey. Both these source have been detected by Spitzer and confirmed as dusty stars. Only one of the ISO sources was marked as dusty sources by Boyer et al. (2006).

Chapter 6

Dust excess and mass loss

For the candidate dusty stars in each GC mass loss rates and average timescales can be obtained by properly modeling the circumstellar dust emission. Once rates and timescales with varying the stellar luminosity are estimated, total mass lost can be computed by integrating over the evolutionary time along the RGB.

6.1   The DUSTY model

In order to obtain the ML rates we use our modified version of the DUSTY code (Ivezić, Nenkova & Elitzur, 1999; Elitzur & Ivezić, 2001), to compute the emerging spectrum and dust emission at the IRAC wavelengths.

The code DUSTY was developed at the University of Kentucky by Zeljko Ivezic, Maia Nenkova and Moshe Elitzur for a commonly encountered astrophysical problem: radiation from sources (e.g. stars, galactic nuclei, etc.) as viewed after processing by a dusty region. The original radiation is scattered, absorbed and re-emitted by the dust, and the emerging processed spectrum often provides the only available information about the embedded object. DUSTY can handle both planar and centrally-heated spherical density distributions. The solution is obtained through an integral equation for the spectral energy density, introduced in Ivezić, Nenkova & Elitzur (1997). The number of independent input model parameters is minimized by fully implementing the scaling properties of the radiative transfer problem, and the spatial temperature profile is found from radiative equilibrium at every point in the dusty region.

We adopt Kurucz model atmospheres for the heating source and for the dust a mixture of warm silicates with an average grain radius $a = 0.1\,\mu$m.

Slightly different choices for the dust properties have negligible impact in the resulting IRAC colors and mass loss rates. While radiation pressure acting on dust might plausibly drive winds in luminous, metal rich red giants (Willson, 2000), the GGC stars are generally neither luminous nor metal rich enough for this mechanism to be efficient. Hence we run the DUSTY code under the general assumption of an expanding envelope at constant velocity v_{exp} with a density profile $\eta \propto r^{-2}$, a dust temperature for the inner boundary r_{in} of 1000 K and a shell outer boundary $r_{\mathrm{out}} = 1000 \times r_{\mathrm{in}}$. We then computed a large grid of DUSTY models with stellar temperatures in the 3500–5000 K range and optical depths at 8 μm (τ_8) between 10^{-5} and 10^{-1}. For each star with dust excess, we enter the grid with its empirical stellar temperature and $(K - IRAC)_0$ colors, and we exit with prediction for the optical depth, emerging flux and envelope radius.

6.2   Mass loss rates

The mass loss rates are computed by using the formula:

$$dM/dt = 4\,\pi\, r_{\mathrm{out}}^2 \times \rho_{\mathrm{dust}} \times v_{\mathrm{exp}} \times \delta$$

where $\rho_{\mathrm{dust}} \propto \rho_{\mathrm{g}}\, \tau_8\, F_8(\mathrm{obs})/F_8(\mathrm{mod})\, D^2/r_{\mathrm{out}}^2$ is the dust density, $\rho_{\mathrm{g}} = 3\,\mathrm{g\,cm^{-3}}$ is the grain density, F_8 are the observed and model fluxes at 8 μm, D the distance, r_{out} the envelope outer radius and δ the gas to dust ratio. A lower limit to δ is given by $1/Z$ where Z^1 is the global metallicity. v_{exp} is a free parameter, which should scale like $\delta^{-0.5}$ if dust and gas are coupled. Indeed, by increasing the number of gas particles (i.e. for higher value of δ), the momentum per particle (either gas or dust) is smaller, hence of v_{exp} decreases (Habing, Tignon & Tielens, 1994; van Loon, 2000). For 47 Tuc we adopt $\delta \approx 1/Z \approx 200$ and $v_{\mathrm{exp}} = 10$ km s^{-1}. The latter is the typical expansion velocity measured in luminous, nearby giants (see e.g. Netzer & Elitzur, 1993) which can range between a few and ≈ 20 kms^{-1}. Even in the most metal poor stars $v_{\mathrm{exp}} \approx 1$ km s^{-1} exceeds the sound speed.

Fig. 6.1 shows the inferred mass loss rates as a function of the bolometric magnitude for the dusty stars of the most populous clusters in our sample. Dusty stars of 47 Tuc and NGC 6441 are marked in red, those of NGC 6388 and NGC 6440 in magenta, those of NGC 362, NGC 1851 and NGC 2808

---

[1]$\log_{10} Z = [M/H] - 1.7$

are marked in green, those of M80 in cyan and finally those of M15 and M92 in blue. The mass loss rate increases with increasing stellar luminosity and decreasing metallicity.
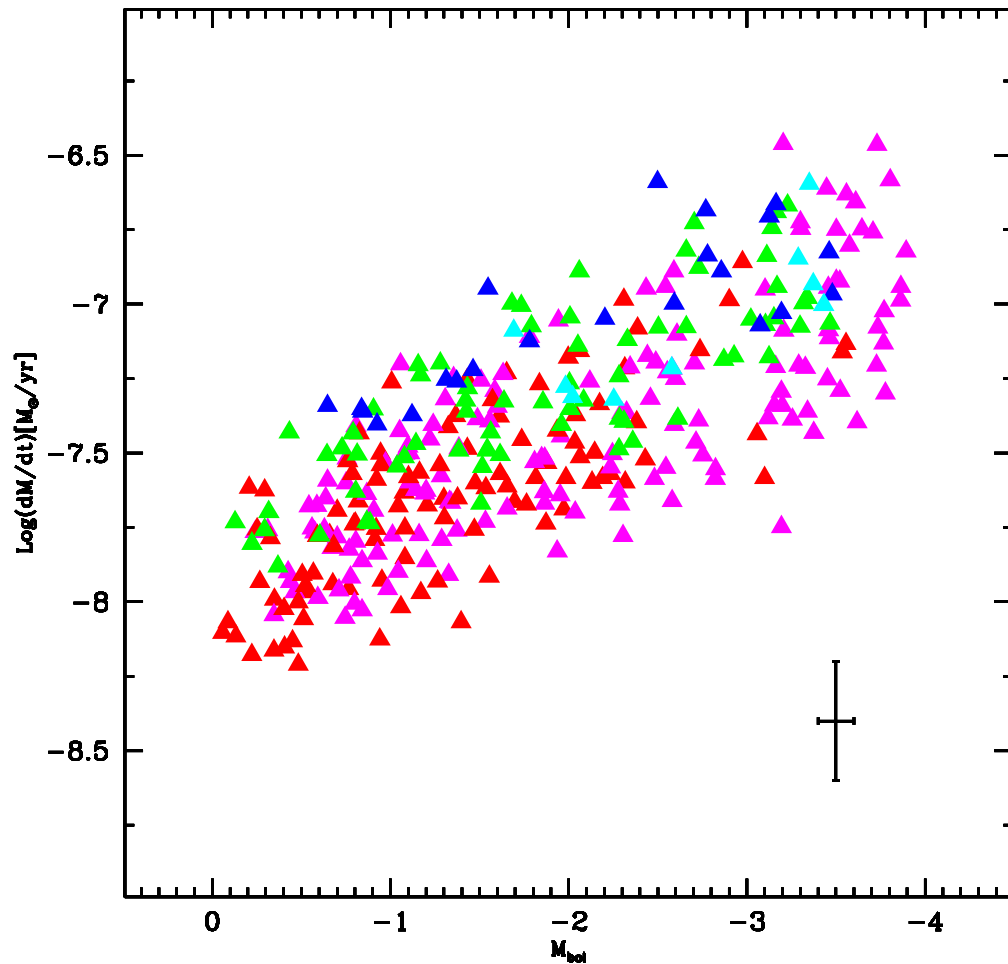

Figure 6.1: Inferred mass loss rates as a function of the bolometric magnitude, for the Spitzer sources with dust excess of the most populous clusters in our sample. Dusty stars of 47 Tuc and NGC 6441 are marked in red, those of NGC 6388 and NGC 6440 in magenta, those of NGC 362, NGC 1851 and NGC 2808 are marked in green, those of M80 in cyan and finally those of M15 and M92 in blue.

Fig. 6.2 shows the inferred mass loss rates as a function of the normalized luminosity, according to the Reimers' formalism. Our empirical estimates are systematically higher than the prediction by extrapolating the Reimers law.
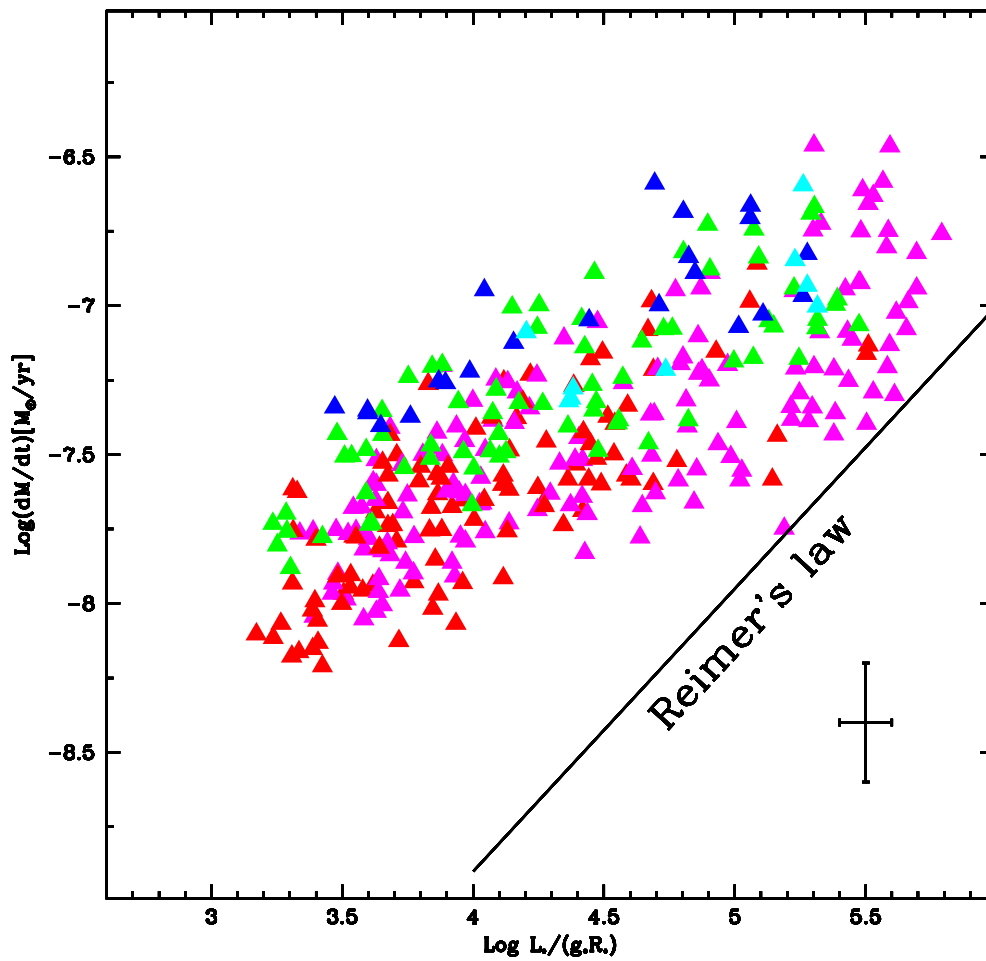
Figure 6.2: Inferred mass loss rates as a function of the normalized luminosity, for the Spitzer sources with dust excess of the most populous clusters in our sample. Dusty stars of 47 Tuc and NGC 6441 are marked in red, those of NGC 6388 and NGC 6440 in magenta, those of NGC 362, NGC 1851 and NGC 2808 are marked in green, those of M80 in cyan and finally those of M15 and M92 in blue. ML derived from extrapolation of the Reimers law (black line) is also plotted for comparison.

The empirical law for the reference cluster 47 Tuc, gives:

$$\mathrm{dM/dt} = C \times 4 \times 10^{-10} \times (L_*/g_* R_*)_{\odot}^{0.4} \qquad [\mathrm{M}_{\odot}\ yr^{-1}]$$

where

$$C = (\delta/200)^{0.5} \times (v_{\mathrm{exp}}/10) \times (\rho_{\mathrm{g}}/3)$$

and $L_{\odot}$, $g_{\odot}$, and $R_{\odot}$ are the stellar luminosity, gravity and radius in solar units. Under the assumption that the same $\delta = \delta_{47\ Tuc} \times (Z_{47\ Tuc}/Z)^{-0.5}$ scaling law applies to all clusters, we can provide a general formulation for mass loss rates in globular cluster giants:

$$\mathrm{dM/dt} = C \times 4 \times 10^{-10} \times (L_*/g_* R_*)_{\odot}^{0.4} \times 10^{-([Fe/H]+0.7)/3} \qquad [\mathrm{M}_{\odot}\ yr^{-1}]$$

Only true RGB stars are used to derive the fitting formula. Errors are as follows: $\approx 10\%$ for L/gR and the fit exponent and $\approx 25\%$ for the fit zero point.

As comparison, we also report the Reimers formula, extrapolated to low luminosity giant stars:

$$\mathrm{dM/dt} = \eta_R \times 4 \times 10^{-13} \times (L_*/g_* R_*)_{\odot} \qquad [\mathrm{M}_{\odot}\ yr^{-1}]$$

6.3   Total Mass Lost

The inspection of the CMDs (Figure 5.1, 5.2, 5.3, 5.4) in the previous Chapter share that only a fraction of stars along the RGB are currently losing mass. This fraction, **f**, can be computed as the ratio between the number of dusty stars and the total number of RGB stars, after correction for incompleteness, field contamination, AGB stars and blending. On average **f** range between 10 and 20 % for $M_{bol} < -1$ and a few percent (at most) in the $-1 < M_{bol} < 0$ bolometric magnitude range. This suggest that the mass loss process is somewhat episodic. In practice, mass loss is "on" for some fraction of the evolutionary time, only. By using suitable evolutionary tracks for RGB stars of M=0.9 $\mathrm{M}_{\odot}$ and Z ranging between 0.004 for metal rich clusters and 0.0003 for metal poor clusters (Pietrinferni et al., 2006), we can derive the evolutionary timescale in each luminosity interval. Multiplying such a timescale by **f**, we find the ML timescale, during which the process of mass loss is active.

Figure 6.3 shows average ML rates and timescales as a function of metallicity, calculated in the first magnitude bin, down to $M_K = -3$ or
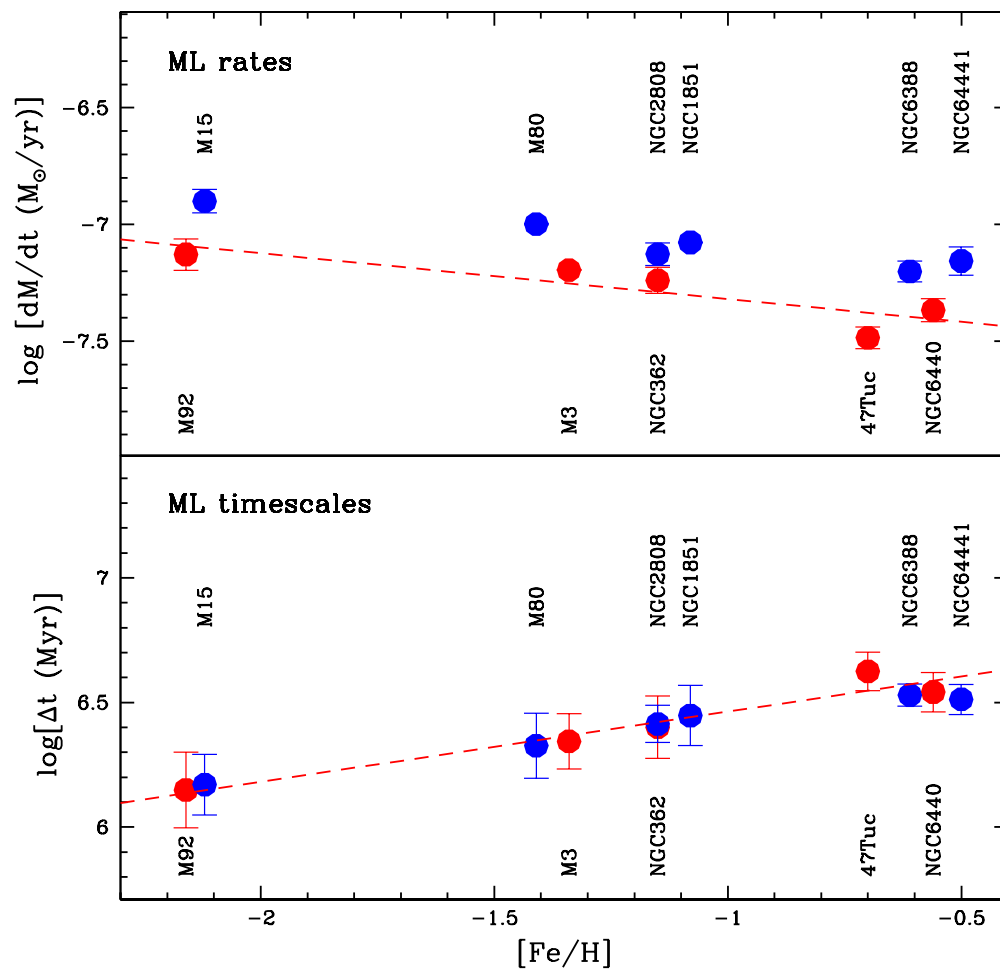
Figure 6.3: This plot shows average ML rates (top panel) and timescales (bottom panel) as a function of metallicity, calculated in the first magnitude bin. Clusters with normal HB are marked in red while clusters with extended blue HB are marked in blue. The dashed lines are obtained from the best fit of the red points.

$M_{bol} = -1$. We divide the RGB in magnitude bins, each bin is set to keep constant the evolutionary temporal duration. The plotted errors on the average ML rates are purely statistic. The error on **f** is Poissonian and depends on the number of dusty stars corrected for incompleteness and total number of RGB stars. Obviously, less populous is the cluster, smaller is the number of the observed stars, and bigger is the relative error. Clusters with normal HB are marked in red, while clusters with extended blue HB are marked in blue. In this analysis we excluded those clusters not populous enough, for which errors due to low number statistics is too severe. In particular: M30 and NGC 6752 have a high central concentration but are intrinsically less luminous; M13 has a relatively low central concentration, so it is poorly populated in the bright portion of the RGB; NGC 288 has a low central concentration, and is intrinsically less luminous; finally NGC 6539 has a relatively low central concentration, so it is poorly populated in the bright portion of the RGB.

As it is possible to see from Figure 6.3, rates decrease with increasing metallicity. The least square fit for the clusters with normal HB (red points) is $\log_{10} dM/dt \approx -0.2 \times [Fe/H] - 7.51$, while timescales becomes longer with increasing metallicity ($\log_{10}(\Delta t_i \times \mathbf{f}_i) \approx 0.28 \times [Fe/H] + 6.74$). For a given metallicity, clusters with extended, blue HB have average higher mass loss rates, while no appreciable difference in the timescales among the two cluster populations is evident.

By using the simple equation:

$$\Delta M_{RGB} = \Sigma_i \left(dM/dt_i \times \Delta t_i \times \mathbf{f}_i \right)$$

to integrate the mass loss formula multiplied by the ML timescale ($\Delta t_i \times \mathbf{f}_i$) we find the total mass lost on the RGB. It is interesting to note that if we do not take into account the frequency **f**, we obtain a total mass lost too high, even exceeding the stellar mass!

Figure 6.4 shows average total mass lost as a function of metallicity. Red points are clusters with normal HB, while blue point are those with extended blue HB. The average total mass lost increases with increasing metallicity.

The red line is the least square fit of the red points: $\Delta M_{RGB} \approx 0.04 \times [Fe/H] + 0.21 \; M_\odot$. The χ^2 test gives a 99% probability that such a linear fit is a good representation of the observed distribution. The probability of a constant ($\Delta M_{RGB} \approx 0.16 \; M_\odot$) total mass lost is 55%, only. However we can not exclude this possibility.
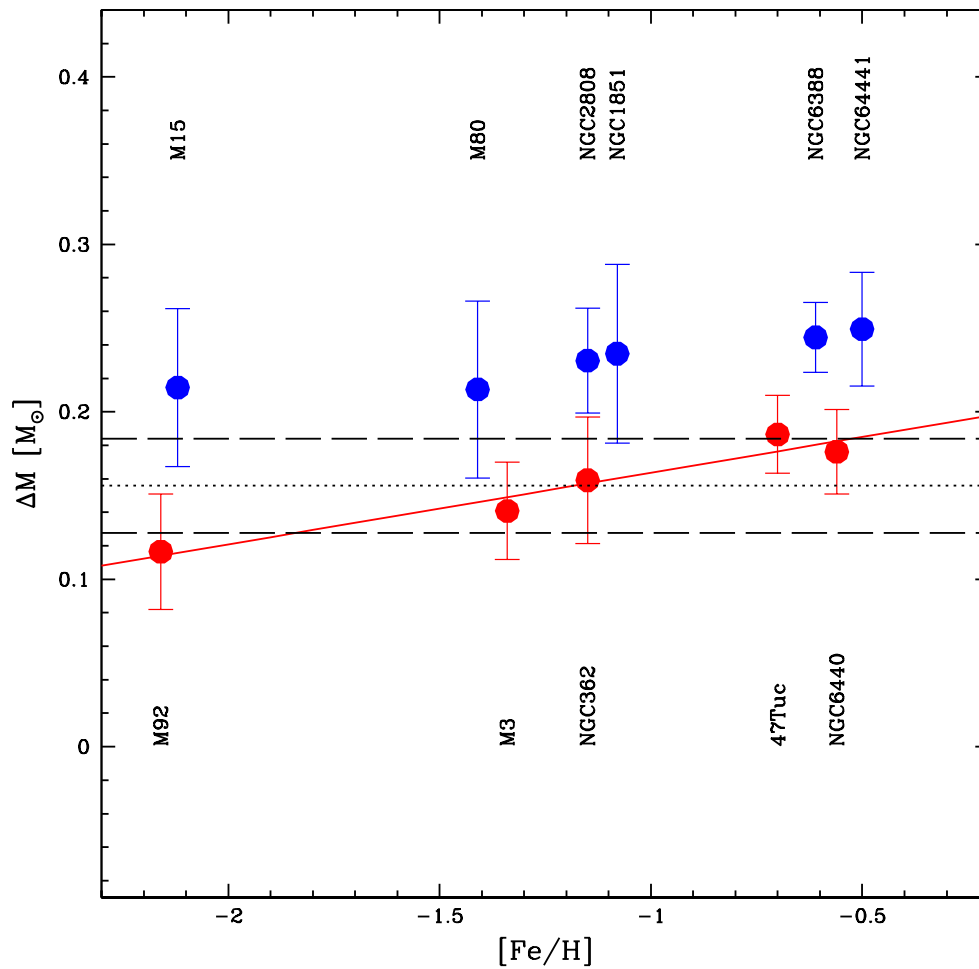
Figure 6.4: Average total mass lost as a function of metallicity. Clusters with normal HB are marked in red while cluster with extended blue HB are marked in blue. The red line is obtained from the least square fit of the red points. The dotted line is the mean of the red points, while the dashed lines are the mean $\pm 1\sigma$.

We find that the average mass lost in GC with normal HB is between 0.1 and 0.2 solar masses, that it increases by a factor of two (at most) from the most metal poor clusters (about 1/100 solar) to the most metal rich ones (about 1/3 solar). In GC with extended blue HB the average mass lost is systematically higher, and varies between 0.20 and 0.26 solar masses, i.e. by about 30% only, in the same metallicity range. The meaning of such an average mass lost in these extended, blue HB clusters is as follow. The majority (about 70-80%) of the stars should lose mass in a normal way, like those in normal HB clusters, while 20-30 % of the stars have enhanced (up to a factor of two) ML. These fractional numbers are consistent with the star counts computed on observed HB populations.

As an example, Figure 6.5 shows the UV CMD of NGC 6388 obtained by Dalessandro et al. (2008). The UV filters are used to properly trace the warm sequences. The HB population is marked with blue symbols and is divided into few group: a red clump, about 80% of the entire population, a blue HB, about 15%, and a blue tail with the remaining stars. It is evident that this population ratios are consistent with the previous numbers.
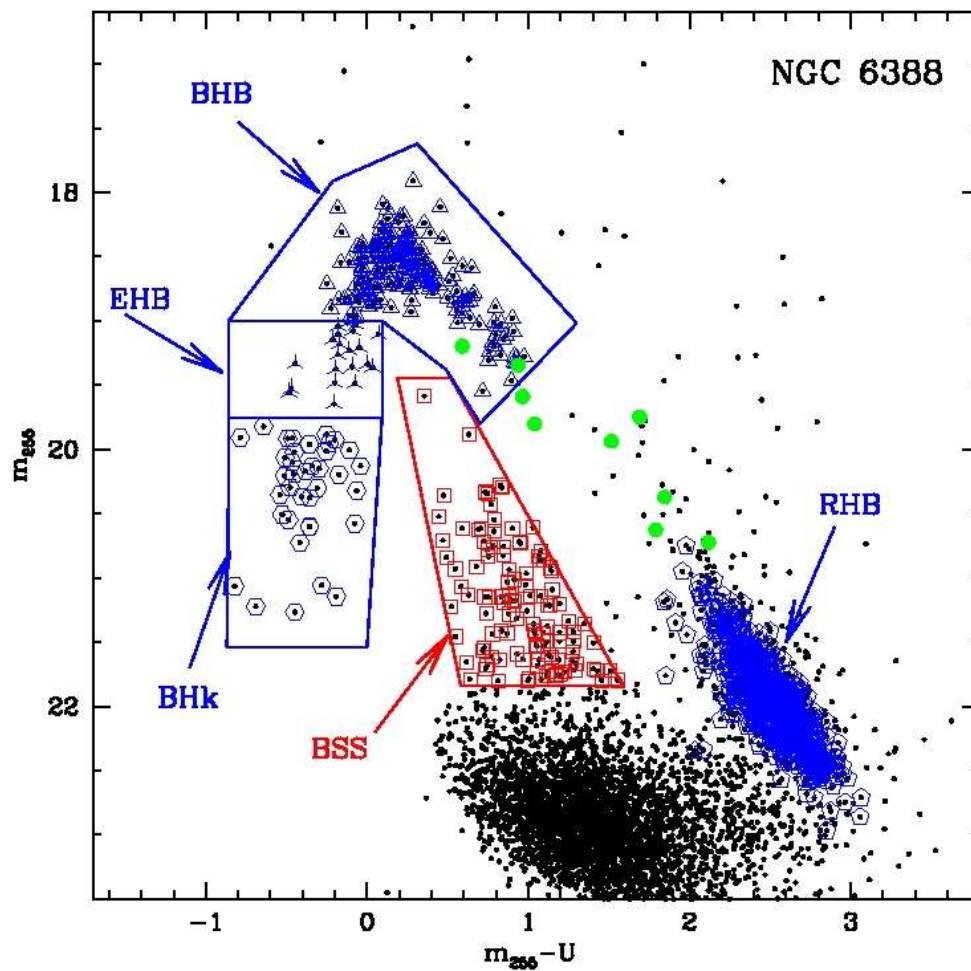
Figure 6.5: UV CMD of NGC 6388. The HB population is marked with blue symbols and is divided into few group: a red clump, about 80% of the population, a blue HB, about 15%, and a blue tail with the remaining stars. The blue stragglers stars (BSS) are marked in red and the RR Lyrae in green.

Conclusions and Future Perspectives

This PhD Thesis presents the results of a mid-IR IRAC@Spitzer survey of a carefully selected sample of 17 GGCs with different metallicity and HB morphology. The goals of the Thesis are twofold: first, to develop an empirical, scaling law for Population II giants over as wide a range of metallicity as possible; second, to develop a better physical understanding of mass loss.

Suitable color-magnitude and color-color diagrams have been computed, to reliable identify candidate mass loosing giants, as traced by the presence of circumstellar dusty envelopes. For each GCC, photospheric and circumstellar dust parameters of the candidate dusty giants are provided.

In particular:

(i) a catalog with the J, H, K, 3.6, 4.5, 5.8, 8.0 photometry and RA and Dec astrometric positions;

(ii) a catalog with photospheric parameters (temperature, absolute K and bolometric magnitudes), colors, warm dust parameters (color-temperature, mass, 8μm flux) and mass loss rates.

The inferred mass loss rates range between 10^{-8} to 10^{-6} $M_\odot$ yr^{-1}.

We find that mass loss rates increases with increasing stellar luminosity and decreasing metallicity. The finding of higher rates at lower metallicities seems to exclude opacity as the main mass loss driving mechanism.

For a given luminosity, ML rates are systematically higher than the prediction by extrapolating the Reimers law.

To properly quantify the dependence of mass loss rates on metallicity, for each cluster we calculated average ML rates in the first magnitude bin down to $M_{bol} \leq -1$.

Average rates for cluster with extended blue HB are systematically higher than for clusters with normal HB.

For the latter GCs, the least square fit of the mass loss rates / metallicity relation gives: $\log_{10} dM/dt \approx -0.2 \times [Fe/H] - 7.51$.

CMDs constructed from ground based near-IR and IRAC bands show that at a given luminosity some stars have dusty envelopes and others do not: so, only a fraction of stars along the RGB are currently loosing mass. This fraction, **f**, can be computed as the ratio between the number of dusty stars and the total number of RGB stars, after correction for incompleteness, field contamination, AGB stars and blending. On average **f** range between 10 and 20% for $M_{bol} < -1$ and a few percent (at most) in the $-1 < M_{bol} < 0$ bolometric magnitude range. Such a behavior suggests that the ML is episodic and is "on" for some fraction of the evolutionary time, **f$_{on}$**. The timescale during the process is "on" is thus significantly shorter (a few million years, only) than the evolutionary time (a few tens million years) If, rather than being episodic, ML was occurring continuously in some stars only, stars losing mass at the observed rates will never reach the He flash. This would lead to a HB much redder than observed and a deficiency in the number of HB stars.

To quantify the dependence of **f** on metallicity, for each cluster we calculated average timescales in the first magnitude bin down to $M_{bol} \leq -1$, and the least square fit gives: $\log_{10}(\Delta t_i \times \mathbf{f}_i) \approx 0.28 \times [Fe/H] + 6.74$.

Although ML seems to be an episodic process, ML modulation mechanism are still quite unknown (cf. e.g. Judge & Stencel, 1991) and matter of debate. There is observational evidence of small-amplitude and short period variability among giants close to the RGB-tip (cf. e.g. Welty 1985; Edmonds & Gilliland 1996), consistent with some oscillation activity (low-overtone radial or non-radial pulsations). Cacciari & Freeman (1983) and Gratton, Pilachowski & Sneden (1984), observed Hα emission lines in hundreds of giants in a large sample of globular clusters. They initially argued that the Hα emission was direct evidence for mass loss. However, interpreting Hα emission can be complicated (Dupree 1986). For example, Dupree et al. (1994) suggest from its time variability that Hα emission is due to atmospheric shocks which might drive the mass loss. In either interpretation the presence of Hα emission in RGB spectra would generally indicate ongoing mass loss.

In the star in which mass loss is best understood, the Sun, the mass loss mechanism is ultimately tied to the magnetic field generated by the convective zone (e.g., Dupree 1986). Since cluster RGB stars have convective zones they

could well have magnetic fields. There are no direct measurements of such fields, and interpreting signatures of chromospheric activity which might arise from magnetic fields is quite complex (e.g., Ayres et al. 1997). There is some recent evidence for RGB starspots which would imply magnetic activity (Stefanik et al. 2002). Soker (2000) and García-Segura et al. (2001) argue that magnetic activity might play a role in AGB mass loss on the basis of planetary nebula morphology.

Some non-canonical deep mixing in the upper RGB has been also invoked to produce excess luminosities and enhancing the mass loss close to the RGB-tip (cf. e.g. Sweigart 1997; Cavallo & Nagar 2000, Weiss, Denissenkov & Charbonnel 2000), but a solid physical picture of the overall impact on the red giant evolution is still lacking.

The total mass lost on the RGB can be easily computed by multiplying ML rates by the ML timescales ($\Delta t_i \times \mathbf{f}_i$) and integrating over the evolutionary timescale. The average total mass lost moderately increases with increasing metallicity, and for a given metallicity is systematically higher in clusters with extended blue HB.

The average mass lost in GC with normal HB is between 0.1 and 0.2 solar masses, it increases by a factor of two (at most) from the most metal poor clusters (about 1/100 solar) to the most metal rich ones (about 1/3 solar). The least square fit gives: $\Delta M_{RGB} \approx 0.04 \times [Fe/H] + 0.21$ M$_\odot$. For a given metallicity ML is systematically higher in GCs with extended blue HB: the average mass lost varies between 0.20 and 0.26 solar masses, i.e. by about 30% only, in the same metallicity range. This means that in the clusters with extended blue HB the majority (about 70-80%) of the stars should loose mass in a normal way, like those in normal HB clusters, while 20-30 % of the stars have enhanced (up to a factor of two) ML.

Future perspectives

In this Section I briefly list some natural follow-up studies inspired by this project.

- In this Thesis I have focussed the attention on mass loss in RGB stars. However mass loss rates and timescales are also obtained for AGB stars. However, a proper analysis of the mass loss timescales and total mass lost

require additional work (e.g. statistical simulations) to properly account the largely dominant low number statistic effects.

- Other constrains on the modulation mechanism can be obtained from a statistical analysis of the intrinsic scatter in the ML rates / luminosity relation (see Figure 6.1).

- Finally, mid-IR survey at much larger spatial resolution and sensitivity will became possible with James Webb Space Telescope (JWST). The JWST is a large, infrared-optimized space telescope, scheduled for launch in 2014. JWST will have a large mirror, 6.5 meters in diameter. MIRI, the mid-IR instrument onboard JWST, will provide imaging and spectroscopy in the 5 - 27 μm spectral range. With MIRI, it will became possible to take high spatial resolution images of the innermost core region of the clusters, and mid IR spectra of the candidate dusty giant stars, to also quantify dust chemical composition and opacity.

Appendix A

NGC 6791

Introduction

NGC 6791 is one of the most massive, metal rich, and oldest open cluster
. Because of these properties, it has been the subject of many photometric
and spectroscopic investigation (Kinman, 1965; Harris & Canterna, 1981;
Demarque, Green & Guenther, 1992; Anthony-Twarog & Twarog, 1985;
Kaluzny, 1990; Kaluzny & Udalski, 1992; Friel & Janes, 1993; Garnavich et
al., 1994; Meynet et al., 1993; Kaluzny & Rucinski, 1993; Tripicco et al., 1995;
Peterson & Green, 1998; Chaboyer, Green & Liebert, 1999; Friel et al., 2002;
Worthey & Jowett, 2003; Stetson, Bruntt & Grundhal, 2003; Carney, Lee &
Dodson, 2005; King et al., 2005; Kalirai et al., 2007).

Its relatively populous color-magnitude diagram suggests a mass ≥ 4000
$M_\odot$ (Kaluzny & Udalski, 1992), and an age in the 8-12 Gyr range, as inferred
from both optical and IR photometry (see e.g Kaluzny & Udalski, 1992;
Tripicco et al., 1995; Chaboyer, Green & Liebert, 1999; Stetson, Bruntt &
Grundhal, 2003; Carney, Lee & Dodson, 2005; Kalirai et al., 2007), depending
also on the adopted reddening and metallicity. Estimates of the cluster
reddening also cover some range, from E(B-V)=0.10 (Janes, 1984) to E(B-
V)=0.22 (Kinman, 1965), with a mean value of E(B-V)=0.16 which is in
excellent agreement with Schlegel, Finkbeiner, & Davis (1998) extinction maps,
which gives E(B-V)=0.15.

NGC 6791 is a relatively distant cluster, with a suggested distance
modulus (m-M)$_0$ ranging from 12.60 (Anthony-Twarog & Twarog, 1985)
to 13.6 (Harris & Canterna, 1981). Current best estimates indicate that
the [α/Fe] is Solar and the metallicity is [Fe/H]=0.3÷0.5 (Kaluzny, 1990;
Demarque, Green & Guenther, 1992; Peterson & Green, 1998; Chaboyer,

Green & Liebert, 1999; Stetson, Bruntt & Grundhal, 2003; Gratton et al., 2006; Origlia et al., 2006). Such an high metallicity would suggest a red HB clump, but the CMD of NGC 6791 exhibits both a clump and a few stars along the extremely blue horizontal branch: this is a strong example of the **second parameter effect**. Several explanations have been proposed for the extreme horizontal branch stars: i) increased mass loss in post main-sequence evolutionary phases, possibly due to the high metallicity of the cluster (Faulkner, 1972); ii) dynamical effects such as binary evolution (Han et al., 2003); iii) mass loss on the horizontal branch (Yong et al., 2000).

NGC 6791 has also a peculiar white dwarf luminosity function, and the metallicity of the cluster has some bearing on the explanation of the WD properties (Bedin et al., 2005; Hansen, 2005). The white dwarf luminosity function can be used to determine the cluster age independently of the main sequence turn-off.

Bedin et al. (2005) find that the white dwarf cooling age of NGC 6791 is a factor of three lower than the misured main sequence turn-off age. Several explanations have been proposed for the white dwarf cooling age discrepancy in NGC 6791.

Recently, Kalirai et al. (2007) presented a photometric and spectroscopic study of the NGC 6791 white dwarf population. They have suggested that most of the white dwarf in the cluster are under-massive, and could not have formed from the canonical stellar evolution following the helium flash at the tip of the red giant branch. The progenitors of these under-massive white dwarfs have lost enough mass along the red giant branch to avoid the flash, and did not convert helium into carbon–oxygen in their core: at least 40% of RGB stars must have experienced higher rates of mass loss. Kalirai et al. (2007) claimed that this increased mass loss is consistent with the presence of the extreme horizontal branch and that the white dwarf cooling age of helium white dwarfs is consistent with the MS turn-off age.

van Loon et al. (2008) have investigated the evidence for super-mass-loss on the RGB of NGC 6791 by looking for circumstellar dust in archival Spitzer infrared images, and by comparing the IR and optical luminosity function with model predictions. They find that there is good agreement between the observed and expected optical and infrared luminosity functions along the RGB in NGC 6791, and that there is little circumstellar dust observed around

RGB stars in that cluster. Hence they conclude that there is no direct evidence supporting the suggestion that metal-rich stars avoid the helium flash at the tip of the RGB and become under-massive helium-core white dwarfs as a result of particularly strong stellar winds.

In this interesting scenario, we have also searched for evidence of increased mass loss on the red giant branch of NGC 6791, both looking for circumstellar dusty envelopes, using archival Spitzer images, and comparing population ratios and optical luminosity functions with template globular clusters.

Spitzer observation

A typical first ascent giant (FARGB) star loses $\sim 0.25\,M_\odot$. In NGC 6791 a $1.1\,M_\odot$ MS turn-off star (these estimates are based on models by VandenBerg et al. 2006 and private communication) must lose $0.6\,M_\odot$ to become a $0.5\,M_\odot$ EHB star. The 0.35–$0.4\,M_\odot$ He WDs observed by Kalirai et al. (2007) must have lost 0.70–$0.75\,M_\odot$ before reaching the RGB-tip. ML in NGC 6791 does not appear to be a simple extrapolation of our GGC results.

NGC 6791 does have some ordinary HB stars, the HB red clump, with masses $\sim 0.7 M_\odot$ (Tripicco et al., 1995), so some stars do reach the RGB-tip. The upper RGB is depleted by those stars which become He WDs. A $0.40\,M_\odot$ He WD leaves the RGB 0.7 mag below the tip; a $0.35\,M_\odot$ He WD departs the RGB 1.6 mag below the tip ($\sim$ 1–1.5 mag above the red HB clump.) Assuming that we want to observe such enhanced mass loss using Spitzer. If the winds are episodic as in GGC we only observe the IR excess in the "on" phase. In GGCs $f_{on} \sim 0.1$–0.2, hence we need a sample of 10 or more stars to be relatively sure of catching at least one stars in the "on" phase. The upper RGB of NGC 6791 does not have these many stars, so we are forced to observe at the level of the HB and below. Ideal Spitzer observation should sample the entire RGB down to the MS turn-off. Unfortunately we do not have such deep observations. In fact NGC 6791 has been observed with IRAC only for Calibration purpose (#1158) on 2005 June 14. The image maps cover the central $9' \times 15'$ of the cluster. High dynamic range mode have been implemented to prevent saturation of brighter sources (short exposures) while maintaining a high signal-to-noise on fainter sources (long exposures). The longest exposures (240s) allow one to measure the RGB down to ≈ 1 mag above the HB level (but we need at least 2 mag fainter photometry). We have examined those

data and we have constructed suitable color-magnitude diagrams (Figure 6.6).
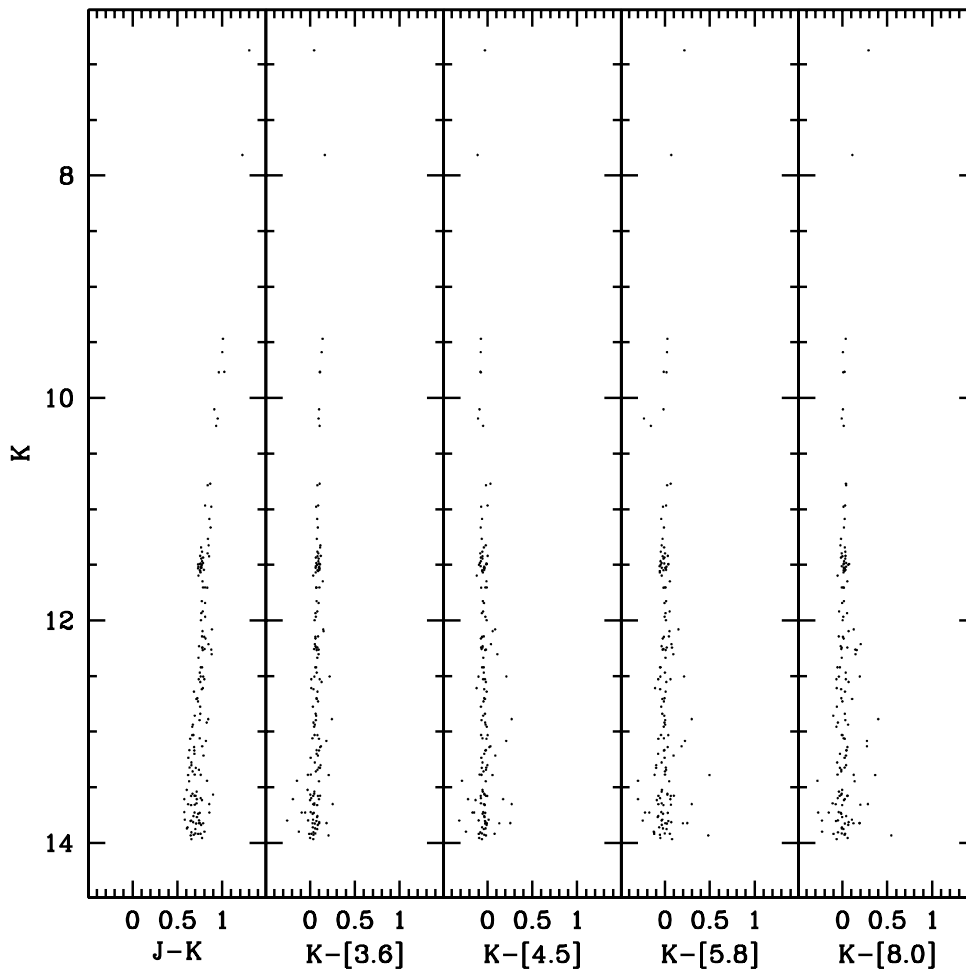We find no stars with an IR excess. However, the sample size is too small, and

Figure 6.6: K, (J-K) and K, (K-IRAC) CMDs of NGC 6791.

we expect to find IR excess in only a fraction of the stars if ML is episodic.

Population ratios

In order to compute appropriate population ratios we have used the BVI
catalog from Stetson, Bruntt & Grundhal (2003), available online on VizieR
database. We have selected the central region of the cluster (r ≤ 300″) and in
the I vs (V-I) color–magnitude diagram (CMD) we have isolated the sub-giant
and giant stars, from the turnoff to the RGB tip. We adopt 47 Tuc as reference

cluster. For this system we have used the ACS+WFI catalog from Beccari et al. (2006). To better isolate the sequences, here we have considered the stars in the outer region of the cluster ($r \geq 600''$): then we have selected stars along the sub-giant and giant stars, from the turnoff to the RGB tip. The field of view and the CMD of the selected RGB stars for the two clusters are showed in Figure 6.7.
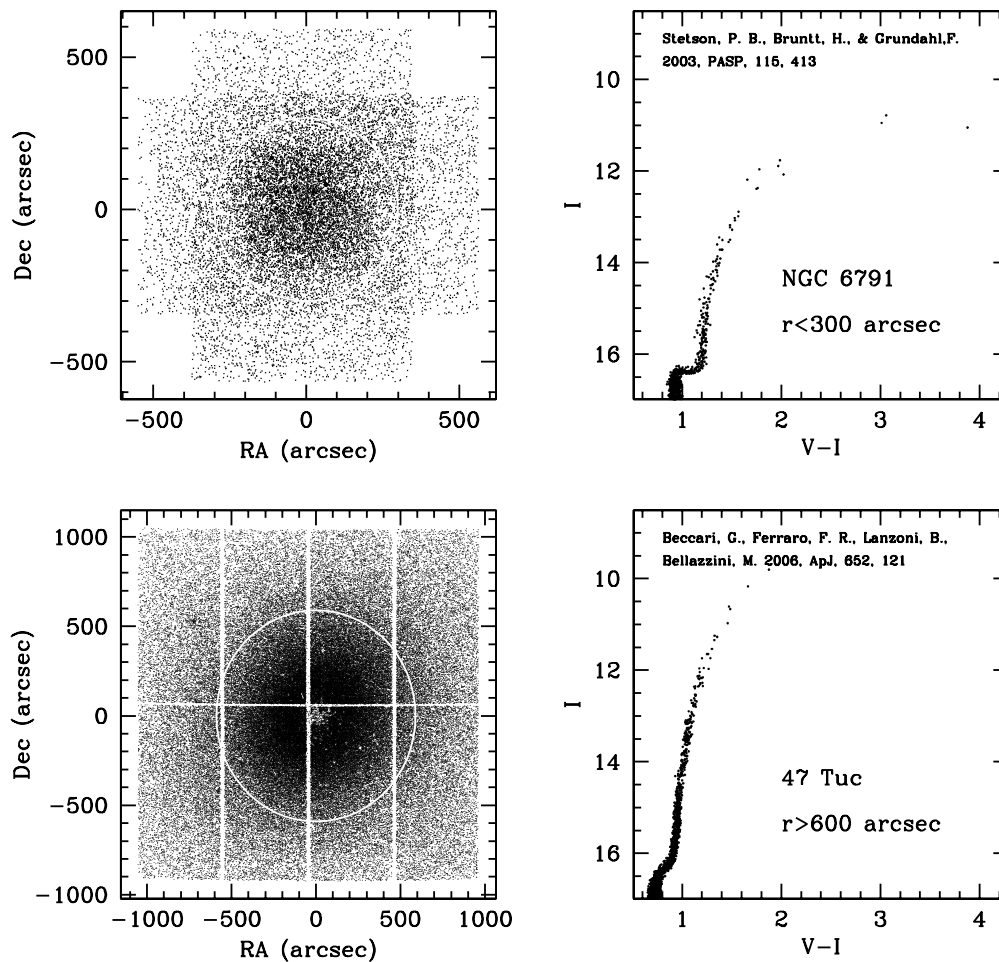

Figure 6.7: Top panels: NGC 6791 selected field of view, the central region of the cluster ($r \leq 300''$), and the correspondent I,(V-I) CMD. Bottom panels: 47 Tuc selected field of view, the outer region of the cluster ($r \geq 600''$), and the correspondent I,(V-I) CMD.

In order to investigate the existence of RGB manqué, we have divided the RGB of each cluster in a few sub-samples (see Figure 6.8) and we have counted

the number of stars in each sample. Then we have computed the population ratios $N_{a,b,c}/N_d$. In Figure 6.8 we have reported the obtained ratios. As can be seen, the population ratio between NGC 6791 and 47 Tuc well agree each other, suggesting that there is not evidence of RGB manqué. Then we have
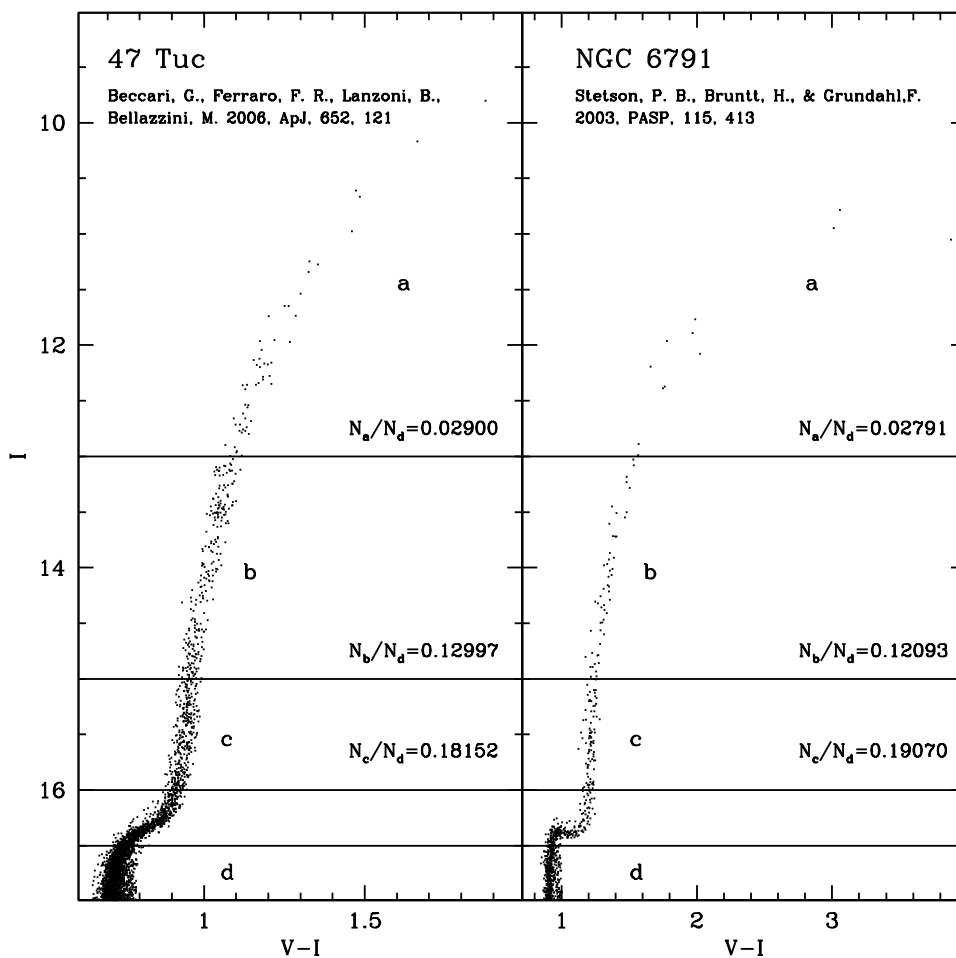

Figure 6.8: CMD of 47 Tuc (right) and of NGC 6791 (left). The population ratios $N_{a,b,c}/N_d$ are also reported.

selected the HB red clump stars in the two clusters and we have computed the population ratio $N_{HB}/N_{a,b,c}$: the population ratios also agree (see Figure 6.9), thus also suggesting that most (if not all) of the red giants in NGC 6791 experienced the helium flash and contributed to form the HB red clump.
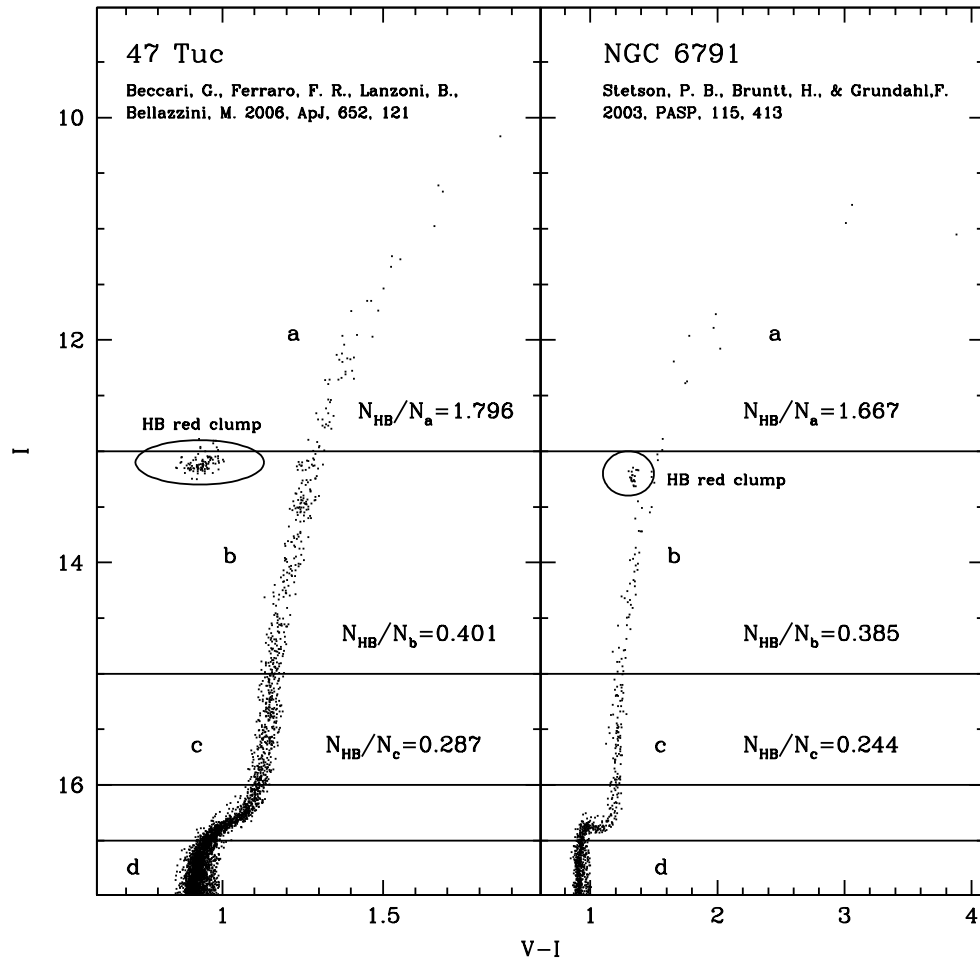
Figure 6.9: CMD of 47 Tuc (right) and of NGC 6791 (left). The population ratios $N_{HB}/N_{a,b,c}$ are also reported.

The Luminosity Function

As a final check to test whether there is a depletion of giants at the RGB tip of NGC 6791, we have compared its luminosity function to that one of 47 Tuc. As can be see in Figure 6.10 (top) the luminosity functions are very similar and there is no evidence of any significant depletion of giants near the tip of NGC 6791.
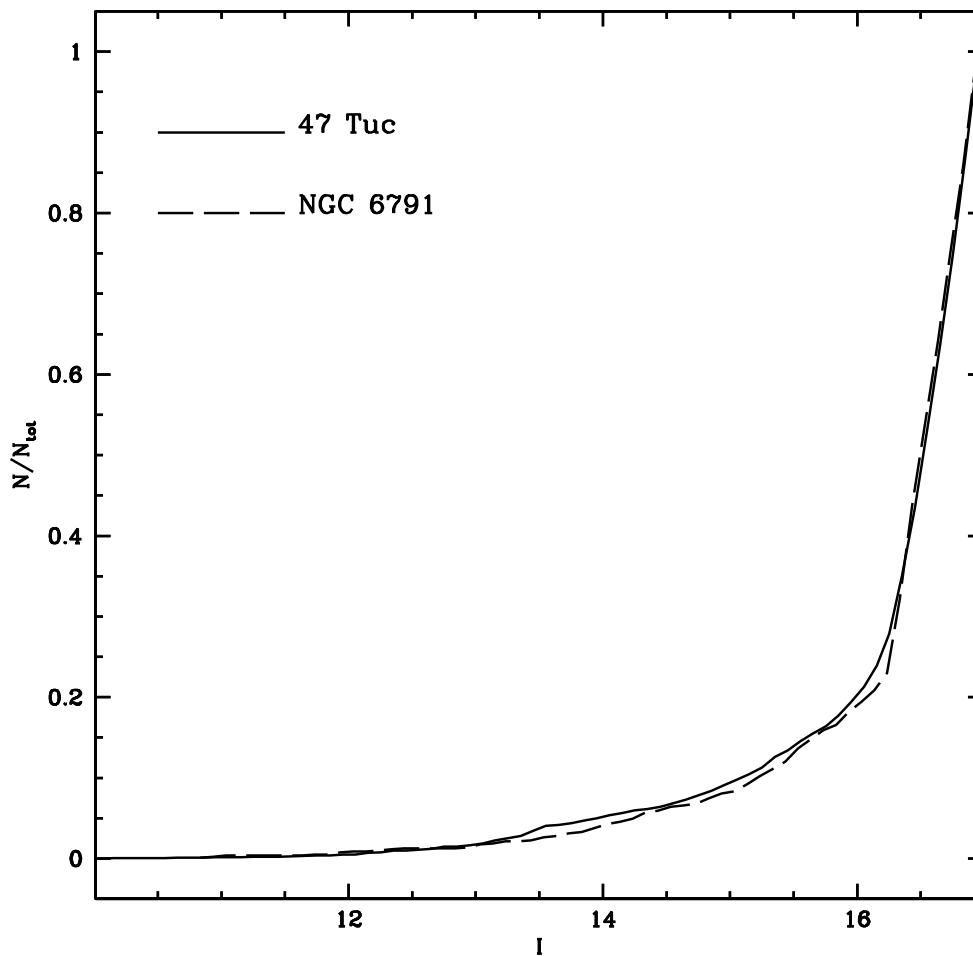

Figure 6.10: Cumulative red giant branch luminosity function of 47 Tuc (solid) and NGC 6791(dashed).

Conclusions

Concluding, all the evidence showed above demonstrated that the number of stars along the RGB of NGC 6791 is consistent with what is expected on the basis of canonical stellar evolution, so there is not an empirical evidence of the enhanced mass loss in this cluster. Future deeper observations of the cluster red giant in the mid-IR could confirm this scenario.

Bibliography

Alves, D. R., Bond, H. E., & Livio, M. 2000, AJ, 120, 2044

Anderson, A. J. 1997, Ph.D. Thesis,

Anderson, J. 2002, Omega Centauri, A Unique Window into Astrophysics, 265, 87

Angeletti, L., Blanco, A., Bussoletti, E., Capuzzo-Dolcetta, R., & Giannone, P. 1982, MNRAS, 199, 441

Anthony-Twarog, B. J. & Twarog, B. A., 1985, ApJ, 291, 595

Auriere, M., Le Fevre, O., & Terzan, A. 1984, A&A, 138, 415

Ayres, T. R., Brown, A., Harper, G. M., Bennett, P. D., Linsky, J. L., Carpenter, K. G., & Robinson, R. D. 1997, ApJ, 491, 876

Baker, J. M., Layden, A. C., Welch, D. L., & Webb, T. M. A. 2007, AJ, 133, 139

Barmby, P., Boyer, M. L., Woodward, C. E, Gehrz, R. D., van Loon J. Th., Fazio, G. G., Marengo, M.& Polomski E. 2009, ApJ137, 207

Bates, B., Catney, M. G., & Keenan, F. P. 1990, MNRAS, 245, 238

Bates, B., Kemp, S. N., & Montgomery, A. S. 1993, A&AS, 97, 937

Beccari, G., Ferraro, F. R., Lanzoni, B., Bellazzini, M. 2006, ApJ, 652, 121

Bedin, L. R., Piotto, G., Anderson, J., Cassisi, S., King, I. R., Momany, Y., & Carraro, G. 2004, ApJl, 605, L125

Bedin, L. R., Salaris, M., Piotto, G., King, I. R., Anderson, J., Cassisi, S., & Momany, Y. 2005, ApJL, 624, L45

Bedin, L. R., Salaris, M., Piotto, G., Cassisi, S., Milone, A. P., Anderson, J., & King, I. R. 2008, ApJl, 679, L29

Boyer, M. L., Woodward, C. E., van Loon, J. T., Gordon, K. D., Evans, A., Gehrz, R. D., Helton, L. A., & Polomski, E. F. 2006, AJ, 132, 1415

Boyer, M. L., McDonald, I., van Loon J. Th., Woodward, C. E, Gehrz, R. D., Evans, A. & Dupree, A. K. 2008, ApJ135, 1395

Boyer, M. L., McDonald, I., van Loon J. Th., Gordon, K. D.Babler, B., Block, M., Bracker, S., Engelbracht, C., Hora, J., Indebetouw, R., Maede, M., Meixner, M., Misselt, K., Oliveira, J. M., Sewilo, M., Shiao, B. & Whitney, B. 2009, ApJ, 705, 746

Boyer, M. L., van Loon, J. T., McDonald, I., Gordon, K. D., Babler, B., Block, M., Bracker, S., Engelbracht, C., Hora, J., Indebetouw, R., Meade, M., Meixner, M., Misselt, K., Sewilo, M., Shiao, B. & Whitney, B. 2010, ApJl, 711, L99

Bragaglia, A., Tosi, M., Andreuzzi, G., & Marconi, G. 2006, MNRAS, 368, 1971

Buonanno, R., Buscema, G., Corsi C. E., Ferraro, I., & Iannicola, G., 1983, A&A, 126, 278

Buonanno, R., Caloi, V., Castellani, V., Corsi, C., Fusi Pecci, F., & Gratton, R. 1986, A&AS, 66, 79

Buonanno, R., Corsi, C., Bellazzini, M., Ferraro, F. R., Fusi Pecci, F., 1997, AJ, 113, 706

Busso, G., Cassisi, S., Piotto, G., Castellani, M., Romaniello, M., Catelan, M., Djorgovski, S. G., Recio Blanco, A., Renzini, A., Rich, M. R., Sweigart, A. V. and Zoccali, M. 2007, A&A, 474, 105

Buzzoni, A. 1989, ApJS, 71, 817

Cacciari, C., & Freeman, K. C. 1983, ApJ, 268, 185

Cacciari, C., Bragaglia, A., Rossetti, E., Fusi Pecci, F., Mulas, G., Carretta, E., Gratton, R. G., Momany, Y. and Pasquini, L. 2004, A&A, 413, 343

Cacciari, C., Bragaglia, A., Rossetti, E., Fusi Pecci, F., Mulas, G., Carretta, E., Gratton, R. G., Momany, Y. & Pasquini, L. 2005, VizieR Online Data Catalog, 341, 30343

Caloi, V., & D'Antona, F. 2005, A&A, 435, 987

Caloi, V., & D'Antona, F. 2007, A&A, 463, 949

Cannon, R. D. 1981, IAU Colloq. 68: Astrophysical Parameters for Globular Clusters, 501

Carney, B. W., Lee, J. W. & Dodson, B. 2005, AJ, 129, 656

Carraro, G., Villanova, S., Demarque, P., McSwain, M. V., Piotto, G., Bedin, L. R. 2006, ApJ, 643, 1151

Carretta, E., Bragaglia, A., Gratton, R. G., Momany, Y., Recio-Blanco, A., Cassisi, S., Francois, P., James, G., Lucatello, S. & Moehler, S. 2007, A&A, 464, 967

Carretta, E., Bragaglia, A., Gratton, R., & Lucatello, S. 2009, A&A, 505, 139

Chaboyer, B,. Green, E. M. & Liebert, J. 1999, AJ117, 1360

Charles, P. A., Jones, D. C., & Naylor, T. 1986, Nature, 323, 417

Catelan, M. 2000, ApJ, 531, 826

Catelan, M., Bellazzini, M., Landsman, W. B., Ferraro, F. R., Fusi Pecci, F., & Galleti, S. 2001, AJ, 122, 3171

Catelan, M., Stetson, P. B., Pritzl, B. J., Smith, H. A., Kinemuchi, K., Layden, A. C., Sweigart, A. V., & Rich, R. M. 2006, ApJl, 651, L133

Cavallo, R. M., & Nagar, N. M. 2000, AJ, 120, 1364

Cesarsky, C.J., Abergel, A., Agnese, P. et al. 1996, A&A, 315, L32

Clement, C. M. 2001, AJ, 122, 2587

Clementini, G., Gratton, R. G., Bragaglia, A., Ripepi, V., Fiorenzano, A. F. M., Held, E. V., & Carretta, E. 2005, ApJl, 630, L145

Cocozza, G., Ferraro, F. R., Possenti, A., & D'Amico, N. 2006, ApJl, 641, L129

Cohen, J. G. 1976, ApJl, 203, L127

Cohen, J. G. 1978, ApJ, 223, 487

Cohen, J. G. 1979, ApJ, 231, 751

Cohen, J. G. 1980, ApJ, 241, 981

Cohen, J. G. 1981, ApJ, 247, 869

Cohen, M., Megeath, S. T., Hammersley, P. L., Martín-Luis, F., & Stauffer, J. 2003, AJ, 125, 2645

Cohen, M., Witteborn, F. C., Carbon, D. F., Davies, J. K., Wooden, D. H., & Bregman, J. D. 1996, AJ, 112, 2274

D'Amico, N., Lyne, A. G., Manchester, R. N., Possenti, A., & Camilo, F. 2001, ApJl, 548, L171

Dalessandro, E., Lanzoni, B., Ferraro, F. R., Rood, R. T., Milone, A., Piotto, G., & Valenti, E. 2008, ApJ, 677, 1069

D'Antona, F., Caloi, V., Montalbán, J., Ventura, P., & Gratton, R. 2002, A&A, 395, 69

D'Antona, F., & Caloi, V. 2004, ApJ, 611, 871

D'Antona, F., Bellazzini, M., Fusi Pecci, F., Galleti, S., Caloi, V., Rood, R. T. 2005, ApJ, 631, 868

D'Antona, F., & Caloi, V. 2008, ArXiv e-prints, 807, arXiv:0807.4233

D'Cruz, N. L., Dorman, B., Rood, R.T., O'Connell, R. W. 1996, ApJ, 466, 359

D'Ercole, A., Vesperini, E., D'Antona, F., McMillan, S. L. W., & Recchi, S. 2008, MNRAS, 391, 825

Demarque, P., Green, E. M. & Guenther, D. B. 1992, AJ, 103, 151

Deutsch, A. J. 1956, ApJ, 123, 210

Deutsch, A. J. 1960, Stellar Atmospheres, 543

Dupree, A. K., Hartmann, L., & Avrett, E. H. 1984, ApJl, 281, L37

Dorman, B., & Rood, R. T. 1993, ApJ, 409, 387

Dupree, A. K. 1986, ARA&A, 24, 377

Dupree, A. K., Sasselov, D. D., & Lester, J. B. 1992, ApJl, 387, L85

Dupree, A. K., Hartmann, L., Smith, G. H., Rodgers, A. W., Roberts, W. H., & Zucker, D. B. 1994, ApJ, 421, 542

Dupree, A. K., & Smith, G. H. 1995, AJ, 110, 405

Dupree, A. K., Smith, G. H., & Strader, J. 2009, AJ, 138, 1485

Edmonds, P. D., & Gilliland, R. L. 1996, ApJl, 464, L157

Elitzur, M., & Ivezić, Z. 2001, MNRAS, 327, 403

Fabbri, S., Origlia, L., Rood, R. T., Ferraro, F. R., Fusi Pecci, F., & Rich, M. 2008, Memorie della Societa Astronomica Italiana, 79, 720

Faulkner, J. 1966, ApJ, 144, 978

Faulkner, J. 1972, ApJ, 173, 401

Faulkner, D. J., & Freeman, K. C. 1977, ApJ, 211, 77

Faulkner, D. J., Scott, T. R., Wood, P. R., & Wright, A. E. 1991, ApJl, 374, L45

Fazio, G. G., Hora, J. L., Allen, L. E., Ashby, M. L. N., Barmby, P., Deutsch, L. K., Huang, J.-S., Kleiner, S., Marengo, M., Megeath, S. T., et al. 2004, ApJS, 154, 10

Ferraro, F. R., Clementini, G., Fusi Pecci, F., Buonanno, R., & Alcaino, G. 1990, A&AS, 84, 59

Ferraro, F. R., Paltrinieri, B., Fusi Pecci, F., Cacciari, C., Dorman, B., & Rood, R. T. 1997, ApJl, 484, L145

Ferraro, F. R., Paltrinieri, B., Pecci, F. F., Rood, R. T., & Dorman, B. 1998, ApJ, 500, 311

Ferraro, F.R., Messineo, M., Fusi Pecci, F., De Palo, M. A., Straniero, O., Chieffi, A., Limongi, M. 1999a, AJ, 118, 1738

Ferraro, F. R., Paltrinieri, B., Rood, R. T., & Dorman, B. 1999b, ApJ, 522, 983

Ferraro, F.R., Montegriffo, P., Origlia, L., Fusi Pecci, F. 2000, AJ, 119, 1282

Ferraro, F. R., Possenti, A., Sabbi, E., & D'Amico, N. 2003a, ApJl, 596, L211

Ferraro, F. R., Possenti, A., Sabbi, E., Lagani, P., Rood, R. T., D'Amico, N., & Origlia, L. 2003b, ApJ, 595, 179

Ferraro, F.R., Dalessandro, E., Mucciarelli, A., Beccari, G., Rich, R. M., Origlia, L., Lanzoni, B., Rood, R. T., Valenti, E., Bellazzini, M., Ransom, S. M., Cocozza, G. 2009, Nature, 462, 483

Forte, J. C., & Mendez, M. 1989, ApJ, 345, 222

Freeman, K. C., & Rodgers, A. W. 1975, ApJl, 201, L71

Freire, P. C., Kramer, M., Lyne, A. G., Camilo, F., Manchester, R. N., & D'Amico, N. 2001, ApJl, 557, L105

Friel, E. D. & Janes, K. A. 1993, A&A, 267, 75

Friel, E. D., Janes, K. A., Tavarez, M., Scott, J., Katsanis, R., Lotz, J., Hong, L., Miller, M. 2002, AJ, 124, 2693

Frogel, J. A., & Elias, J. H. 1988, ApJ, 324, 823

Fusi Pecci, F., & Renzini, A. 1975, A&A, 39, 413

Fusi Pecci, F., & Renzini, A. 1976, A&A, 46, 447

Fusi Pecci, F., Ferraro, F. R., Crocker, D. A., Rood, R. T., & Buonanno, R. 1990, A&A, 238, 95

Fusi Pecci, F., Ferraro, F. R., Bellazzini, M., Djorgovski, S., Piotto, G., Buonanno, R. 1993, AJ, 105, 1145

García-Segura, G., López, J. A., & Franco, J. 2001, ApJ, 560, 928

Garnavich, P. M., VandenBerg, D. A., Zurek, D. R., Hesser, J. E. 1994, AJ, 107, 1097

Geyer, E. H., Nelles, B., & Hopp, U. 1983, A&A, 125, 359

Gillett, F. C., Low, F. J., & Stein, W. A. 1968, ApJ, 154, 677

Gillet, F. C., deJong, T., Neugebauer, G., Rice, W. L., & Emerson, J. P., 1988, AJ, 96, 116

Goldberg, L. 1979, QJRAS, 20, 361

Gratton, R. G., Pilachowski, C. A., & Sneden, C. 1984, A&A, 132, 11

Gratton, R. G., Bonifacio, P., Bragaglia, A., Carretta, E., Castellani, V., Centurion, M., Chieffi, A., Claudi, R., Clementini, G., D'Antona, F., et al. 2001, A&A, 369, 87

Gratton, R., Sneden, C., & Carretta, E. 2004, ARA&A, 42, 385

Gratton, R., Bragaglia, A., Carretta, E., Tosi, M. 2006, ApJ, 642, 462

Gratton, R. G., Lucatello, S., Bragaglia, A., Carretta, E., Cassisi, S., Momany, Y., Pancino, E., Valenti, E., Caloi, V., Claudi, R., et al. 2007, A&A, 464, 953

Greggio & Renzini 1990, ApJ, 364, 35

Grindlay, J. E., & Liller, W. 1977, ApJl, 216, L105

Guhathakurta, P., Webster, Z. T., Yanny, B., Schneider, D. P., & Bahcall, J. N. 1998, AJ, 116, 1757

Guilain, C., Mauron, N., 1996, A&A, 314, 585

Han, Z., Podsiadlowski, P., Maxted, P. F. L., & Marsh, T. R. 2003, MNRAS, 341, 669

Hansen, B. M. S. 2005, ApJ, 635, 526

Habing, H.J., Tignon, J., & Tielens, A.G.G.M. 1994, A&A, 286, 523

Hansen, B. M. S. 2005, ApJ, 635, 522

Harris, W. E. & Canterna, R. 1981, AJ, 86, 1332

Harris, W. E. 1996, AJ, 112, 1487

Harris, W. E. 2003, *Catalog of parameters for milky way Globular Clusters: the database*, accessible at http://www.physics.mcmaster.ca/∼harris/mwgc.dat

Hartwick F.D.A., Cowley A.P., Grindlay J.E., 1982, ApJ, 254, L11

Heinke, C. O., Grindlay, J. E., Edmonds, P. D., Lloyd, D. A., Murray, S. S., Cohn, H. N., & Lugger, P. M. 2003, ApJ, 598, 516

Holzer, T. E., & MacGregor, K. B. 1985, Mass Loss from Red Giants, 117, 229

Howard, J. W., Henry, R. B. C., & McCartney, S. 1997, MNRAS, 284, 465

Howell, J. H., Guhathakurta, P., & Tan, A. 2000, AJ, 119, 1259

Hopwood, M. E. L., Eyres, S. P. S., Evans, A., Penny, A., & Odenkirchen, M. 1999, A&A, 350, 49

Hut, P., McMillan, S. Goodman, J., Mateo, M., Phinney, E. S., Pryor, C., Richer, H. B., Verbunt, F. & Weinberg, M. 1992, PASP, 104, 981

Indebetouw, R., Mathis, J. S.,Babler, B. L., Meade, M. R., Watson, C., Whitney, B. A., Wolff, M. J., Wolfire, M. G., Cohen, M., Bania, T. M., Benjamin, R. A., Clemens, D. P., Dickey, J. M., Jackson, J. M., Kobulnicky, H. A., Marston, A. P., Mercer, E. P., Stauffer, J. R., Stolovy, S. R. and Churchwell, E. 2005, ApJ, 619, 931

Ita, Y. , Tanab, T., Matsunaga, N., Nakada, Y., Matsuura, M., Onaka, T., Matsuhara, H., Wada, T., Fujishiro, N., Ishihara, D. et al. 2007, PASJ, 59, 437

Ivezić, Z., Nenkova, M., & Elitzur, M., 1997, MNRAS, 287, 799

Ivezić, Z., Nenkova, M., & Elitzur, M., 1999, User Manual for DUSTY, (Lexington: Univ. Kentucky), accessible at http://www.pa.uky.edu∼moshe/dusty

Janes, K. A. 1984, PASP, 96, 977

Janes, K., & Kassas, M. 1997, The Third Pacific Rim Conference on Recent Development on Binary Star Research, 130, 107

Judge, P.G., & Stencel, R. E. 1991, ApJ, 371, 357

Kalirai, J. S., Bergeron, P., Hansen, B. M. S., Kelson, D. D., Reitzel, D. B., Rich, R. M., & Richer, H. B. 2007, ArXiv e-prints, 705, arXiv:0705.0977

Kalirai, J. S. 2007, Astronomical Society of the Pacific Conference Series, 372, 91

Kaluzny, J. 1990, MNRAS, 243, 492

Kaluzny, J. & Udalski, A. 1992, ACTA Astron., 42, 29

Kaluzny, J. & Rucinski, S. M. 1993, MNRAS, 265, 34

Kemp, S. N., & Bates, B. 1995, A&AS, 112, 513

Kessler M. F., Steinz, J. A., Anderegg, M. E. et al. 1996, A&A, 315, L27

Knapp, G. R., Rose, W. K., & Kerr, F. J. 1973, ApJ, 186, 831

Knapp, G. R., Gunn J.E., Connoly A.J. 1995, ApJ, 448, 195

King, I. R., Bedin, L. R., Piotto, G., Cassisi, S., & Anderson, J. 2005, AJ, 130, 626

Kinman, T. D. 1965, ApJ, 142, 655

Kulkarni, S. R., & Anderson, S. B. 1996, Dynamical Evolution of Star Clusters: Confrontation of Theory and Observations, 174, 181

Kurucz, R. L. 1993a, Kurucz CD ROM 18, SYNTHE Spectrum Synthesis Programs and Line Data (Cambridge: SAO)

Kurucz, R. L. 1993b, Kurucz CD ROM 13, ATLAS9 Stellar Atmosphere Programs and 2 km/s Grid (Cambridge: SAO)

Lebzelter, T., Posch, T., Hinkle, P. R. & Bouwman, J. 2006, ApJl653, L145

Lee, Y.-W., Joo, J.-M., Sohn, Y.-J., Rey, S.-C., Lee, H.-C., & Walker, A. R. 1999, Nature, 402, 55

Lynch, D. K., & Rossano, G. S. 1990, AJ, 100, 719

Lyons, M. A., Kemp, S. N., Bates, B., & Shaw, C. R. 1996, MNRAS, 280, 835

McDonald, I. & van Loon J. Th. 2007 A&A, 476, 1261

Maeder, A., & Meynet, G. 2005, A&A, 440, 1041

Mallia, E. A., & Pagel, B. E. J. 1978, MNRAS, 184, 55P

Mauas, P.J.D., Cacciari, C., Pasquini, L. 2006, A&A, 454, 609

Megeath, S. T., Cohen, M., Stauffer, J., Hora, J. L., Fazio, G., Berlind, P., & Calkins, M. 2003, The Calibration Legacy of the ISO Mission, 481, 165

Mengel, J. G., & Gross, P. G. 1976, Ap&SS, 41, 407

Meynet, G., Mermilliod, J. C. & Maeder, A. 1993, A&AS, 98, 477

Merritt, D., Meylan, G., & Mayor, M. 1997, AJ, 114, 1074

Milone, A. P., Bedin, L. R., Piotto, G., Anderson, J., King, I. R., Sarajedini, A., Dotter, A., Chaboyer, B., Marìn-Franch, A., Majewski, S. et al. 2008, ApJ, 673, 241

Minniti, D., Coyne, S. J., & Claria, J. J. 1992, AJ, 103, 871

Montegriffo, P., Ferraro, F. R., Fusi Pecci, F., & Origlia, L. 1995, MNRAS, 276, 739

Montegriffo, P., Ferraro, F.R., Fusi Pecci, F., & Origlia, L. 1998, MNRAS, 297, 872

Moorwood, A. F. M et al. 1992, The Messenger, 69, 61

Moorwood, A., Cuby, J.-G., & Lidman, C. 1998, The Messenger, 91, 9

Mullan, D. J. 1978, ApJ, 226, 151

Natta, A., & Panagia, N. 1976, A&AS, 50, 191

Netzer, N., & Elitzur, M. 1993, ApJ, 410, 701

Norris, J. E., & Da Costa, G. S. 1995, ApJ, 447, 680

Norris, J. E., Freeman, K. C., & Mighell, K. J. 1996, ApJ, 462, 241

Norris, J. E. 2004, ApJ, 612, L25

Origlia, L., Ferraro, F. R., & Fusi Pecci, F. 1995, MNRAS, 277, 1125

Origlia, L., Ferraro, F. R., & Fusi Pecci, F. 1996, MNRAS, 280, 572

Origlia, L., Gredel, R., Ferraro, F. R., & Fusi Pecci, F. 1997a MNRAS, 289, 948

Origlia, L., Scaltriti F., Anderlucci E., Ferraro, F. R., & Fusi Pecci, F. 1997b MNRAS, 292, 753

Origlia, L., Ferraro, F.R., Fusi Pecci, F., Rood, R.T. 2002, ApJ, 571, 458

Origlia, L., Valenti, E., Rich, R. M. & Ferraro, F. R. 2005 MNRAS, 363, 897

Origlia, L., Valenti, E., Rich, R. M., Ferraro, F. R. 2006, ApJ, 646, 499

Origlia, L., Rood, R. T., Fabbri, S., Ferraro, F. R., Fusi Pecci, F., & Rich, R. M. 2007, ApJL, 667, L85

Origlia, L., Lena, S., Diolaiti, E., Ferraro, F. R., Valenti, E., Fabbri, S., & Beccari, G. 2008, ApJl, 687, L79

Pancino, E., Ferraro, F. R., Bellazzini, M., Piotto, G., & Zoccali, M. 2000, ApJ, 534, L83

Pancino, E., Pasquini, L., Hill, V., Ferraro, F. R., & Bellazzini, M. 2002, ApJl, 568, L101

Pease, F. G. 1928, PASP, 40, 342

Penny, A., Evans, A., & Odenkirchen, M. 1997, A&A, 317, 694

Peterson, R. C. 1981, ApJl, 248, L31

Peterson, R. C. 1982, ApJ, 258, 499

Peterson, C. J. 1993, Structure and Dynamics of Globular Clusters, 50, 337

Peterson, R.C., Rood, R.T., Crocker, D.A. 1995, ApJ, 453, 214

Peterson, R. C. & Green, E. M. 1998, AJ, 502, L39

Pietrinferni, A. Cassisi, S., Salaris, M., Castelli, F. 2006, ApJ, 642, 797

Pinsonneault, M. H., Deliyannis, C. P., & Demarque, P. 1991, ApJ, 367, 239

Piotto, G., King, I. R., Djorgovski, S. G., Sosin, C., Zoccali, M., Saviane, I., De Angeli, F., Riello, M., Recio-Blanco, A., Rich, R. M., Meylan, G. & Renzini, A. 2002, A&A, 391, 945

Piotto, G., Villanova, S., Bedin, L. R., Gratton, R., Cassisi, S., Momany, Y., Recio-Blanco, A., Lucatello, S., Anderson, J., King, I. R., Pietrinferni, A. & Carraro, G. 2005, ApJ, 621, 777

Piotto, G., Bedin, L. R., Anderson, J., King, I. R., Cassisi, S., Milone, A. P., Villanova, S., Pietrinferni, A. & Renzini, A. 2007, ApJl, 661, L53

Phinney, F. S. 1996, The Origins, Evolution, and Destinies of Binary Stars in Clusters, 90, 163

Pritzl, B. J., Smith, H. A., Catelan, M., & Sweigart, A. V. 2001, AJ, 122, 2600

Pritzl, B. J., Smith, H. A., Catelan, M., & Sweigart, A. V. 2002, Observed HR Diagrams and Stellar Evolution, 274, 335

Pritzl, B. J., Smith, H. A., Stetson, P. B., Catelan, M., Sweigart, A. V., Layden, A. C., & Rich, R. M. 2003, AJ, 126, 1381

Pryor, C., & Meylan, G. 1993, Structure and Dynamics of Globular Clusters, 50, 357

Reach, W. T., Megeath, S. T., Cohen, M., Hora, J., Carey, S., Surace, J., Willner, S. P., Barmby, P., Wilson, G., Glaccum, W., et al. 2005, PASP, 117, 978

Reimers D. 1975a, in Problems in Stellar Atmospheres and Envelopes, eds. B. Baschek, W. H. Kegel, & G. Traving (Berlin: Springer), 229

Reimers D. 1975b, in *Mem. Soc. R. Sci. Liège 6 Ser.*, 8, 369

Renzini, A. 1977, in *Advanced Stages of Stellar Evolution*, ed. Bouvier & A. Maeder (Geneva Obs., Geneva), 151

Renzini, A., & Fusi Pecci, F. 1988, ARA&A, 26, 199

Rich, M.R., Sosin C., Djorgovski, S.G., Piotto, G., King, I.R., Renzini, A., Phinney, E.S., Dorman, B., Liebert, J., Meylan, G. 1997, ApJ, 484, 25

Rich, R.M., & Origlia, L. 2005, ApJ, 634, 1293

Richer, H. B., Fahlman, G. G., Rosvick, J., & Ibata, R. 1998, ApJL, 504, L91

Rieke, G. H., & Lebofsky, M. J. 1985, ApJ, 288, 618

Roberts, M.S. 1988, IAU Symp. 126, J.E. Grindlay & A.G.D. Philip eds., 411

Rood, R.T. 1973, ApJ, 184, 815

Sandage, A., & Wallerstein, G. 1960, ApJ, 131, 598

Sandage, A., & Wildey, R. 1967, ApJ, 150, 469

Sandell G., Stevens M. A., Heiles C. 1987, A&A, 179, 255

Saviane, I., Piotto, G., Fagotto, F., Zaggia, S., Capaccioli, M., & Aparicio, A. 1998, A&A, 333, 479

Sawyer Hogg, H. 1973, Publications of the David Dunlap Observatory, 3, 6

Schlegel, D. J., Finkbeiner, D. P., & Davis, M. 1998, ApJ, 500, 525

Schröder, K.-P., & Cuntz, M. 2005, ApJl, 630, L73

Smith, G. H., & Dupree, A. K. 1988, AJ, 95, 1547

Smith, G. H., Wood, P. R., Faulkner, D. J., & Wright, A. E. 1990, ApJ, 353, 168

Smith, G. H., Dupree, A. K., & Churchill, C. W. 1992, AJ, 104, 2005

Smith G. H., Woodsworth A.W., Hesser J.E., 1995, MNRAS, 273, 632

Smith, G. H., Dupree, A. K., & Strader, J. 2004, PASP, 116, 819

Smith, M. G., Hesser, J. E., & Shawl, S. J. 1976, ApJ, 206, 66

Smith, V. V., Suntzeff, N. B., Cunha, K., Gallino, R., Busso, M., Lambert, D. L., & Straniero, O. 2000, AJ, 119, 1239

Sneden, C., Kraft, R. P., Shetrone, M. D., Smith, G. H., Langer, G. E., & Prosser, C. F. 1997, AJ, 114, 1964

Soker, N. 2000, ApJ, 540, 436

Sollima, A., Ferraro, F. R., Origlia, L., Pancino, E., & Bellazzini, M. 2004, A&A, 420, 173

Sollima, A., Pancino, E., Ferraro, F. R., Bellazzini, M., Straniero, O., & Pasquini, L. 2005, ApJ, 634, 332

Sollima, A., Ferraro, F. R., Pancino, E., & Bellazzini, M. 2005, MNRAS, 357, 265

Sollima, A., Borissova, J., Catelan, M., Smith, H. A., Minniti, D., Cacciari, C., & Ferraro, F. R. 2006, ApJl, 640, L43

Sollima, A., Ferraro, F. R., Bellazzini, M., Origlia, L., Straniero, O., & Pancino, E. 2007, ApJ, 654, 915

Sosin, C., & King, I. R. 1997, AJ, 113, 1328

Sosin, C., Dorman, B., Djorgovski, S. G., Piotto, G., Rich, R. M., King, I. R., Liebert, J., Phinney, E. S. & Renzini, A. 1997, ApJl, 480, L35

Stefanik, R. P., Carney, B. W., Latham, D. W., Morse, J. A., & Laird, J. B. 2001, Bulletin of the American Astronomical Society, 33, 1310

Stephens, A. W., & Frogel, J. A. 2004, AJ, 127, 925

Stetson, P. B., 1987, PASP, 99, 191

Stetson, P. B., 1994, PASP, 106, 726

Stetson, P. B., Bruntt, H. & Grundhal, F. 2003, PASP115, 413

Stetson, P. B., McClure, R. D., & VandenBerg, D. A. 2004, PASP, 116, 1012

Suntzeff, N. B., & Kraft, R. P. 1996, AJ, 111, 1913

Sweigart, A. V. 1997, ApJl, 474, L23

Sweigart, A. V., Brown, T. M., Lanz, T., Landsman, W. B. & Hubeny, I. 2002, ASPC 265, 261

Tripicco, M. J., Bell, R. A., Dorman, B., Hufnagel, B. 1995, AJ, 109, 1697

Valenti, E., Ferraro, F.R., & Origlia, L. 2004a, MNRAS, 351, 1204

Valenti, E., Ferraro, F. R., & Origlia, L. 2004b, MNRAS, 354, 815

Valenti, E., Ferraro, F. R., & Origlia, L. 2007, AJ, 133, 1287

VandenBergh, S. 1967, AJ, 72, 70

VandenBerg, D. A., Bergbusch, P. A., & Dowler, P. D. 2006, ApJS, 162, 375

van Loon, J. T. 2000, A&A, 354, 125

van Loon, J. T., Stanimirović, S., Evans, A., & Muller, E. 2006, MNRAS, 365, 1277

van Loon, J. T. 2007, van Leeuwen, F., Smalley, B., Smith, A. W., Lyons, N. A., McDonald, I. & Boyer, M. L. 2007, MNRAS, 382, 1353

van Loon, J. T., Boyer, M. L., & McDonald, I. 2008, ApJl, 680, L49

van Loon, J. T., Smith, K. T., McDonald, I., Sarre, P. J., Fossey, S. J., & Sharp, R. G. 2009, MNRAS, 399, 195

Villanova, S., Piotto, G., King, I. R., Anderson, J., Bedin, L. R., Gratton, R. G., Cassisi, S., Momany, Y., Bellini, A., Cool, A. M., Recio-Blanco, A. & Renzini, A. 2007, ApJ, 663, 296

Walker, A. R. 1992, PASP, 104, 1063

Wehlau, A., Butterworth, S., & Hogg, H. S. 1990, AJ, 99, 1159

Weiss, A., Denissenkov, P. A., & Charbonnel, C. 2000, A&A, 356, 181

Welty, D. E. 1985, AJ, 90, 2555

Weymann, R. 1962, ApJ, 136, 476

Wilson, W. J., & Barrett, A. H. 1972, A&A, 17, 385

Wilson, W. J. 1973, Molecules in the Galactic Environment, 165

Willson, L. A. 2000, ARA&A, 38, 573

Woolf, N. J., & Ney, E. P. 1969, ApJl, 155, L181

Worthey, G. & Jowett, K. J. 2003, PASP, 115, 96

Yong, H., Demarque, P., & Yi, S. 2000, ApJ, 539, 928

Zinn, R. 1985, ApJ, 293, 424